7-2020

Understanding the Interfacial Reactions Initiating on Lithium Metal Surfaces in Next-Generation Battery Technologies

Joshua A. Lochala
University of Arkansas, Fayetteville

Understanding the Interfacial Reactions Initiating on Lithium Metal Surfaces
in Next-Generation Battery Technologies

A dissertation submitted in partial fulfillment
of the requirements for the degree of
Doctor of Philosophy of Chemistry

by

Joshua A. Lochala
John Brown University
Bachelor of Science in Chemistry, 2015

July 2020
University of Arkansas

This dissertation is approved for recommendation to the Graduate Council

Jie Xiao, Ph.D.
Dissertation Director

Robert Coridan, Ph.D.
Committee Member

David Paul, Ph.D.
Committee Member

Stefan Kilyanek, Ph.D.
Committee Member

Ryan Tian, Ph.D.
Committee Member

Abstract

Li-ion batteries have started to reach the theoretical maximum energy. Next-generation batteries represent the future of portable energy sources for vehicle electrification and grid energy storage. Li metal battery is one of the most promising next-generation battery technologies that could potentially double the cell level energy of conventional Li-ion batteries. However, Li metal has multiple drawbacks that require addressing before realization. These drawbacks include dendrite formation leading to internal short and increasing internal resistance due to the breakdown of electrolyte, leading to rapid cell death. These problems stem from the interfacial reactions occurring during the plating and stripping of Li metal. The plating of Li metal is impacted by the mass transport of ions within the electrolyte and surface conditions of the substrate it is plating on. The research presented here strives to understand the interfacial reactions due to the atomistic nature of the substrate, both in crystal type and facet selection, and the surface compounds present on the substrates with regards to surface oxides and other conversion materials. W was found to show a promising performance when compared to Cu. The SEI on W showed a more robust composition with an increase in inorganic component production. The crystal face present during plating causes the plated Li to match the crystal face; however, as the thickness of the plated Li increases, the crystal structure becomes anisotropic and starts to become unimodal. The unimodal texture showed that Li plates in the basis-oriented reproductive type (BR), with the zeta-fiber being the preferred texture. The surface compounds present were explored initially with WO_3, as the oxygen content is controllable, and the WO_3 undergoes multiple transformations. A first of its kind application of WO_3 was found to impact the Li plating and stripping by changing the solid electrolyte interface (SEI) properties through participation in the electrochemical reactions. The presence of W, derived from WO_3, within the SEI, creates a framework that helps to regenerate ”dead” Li. Additionally, the modified SEI changes the nature of Li nucleation and helps to form a denser inorganic layer by catalytically increasing the decomposition of the electrolyte. New insights have been provided in tailoring SEI properties formed on Li metal surfaces to inspire revolutionary ideas to address the grand challenges of rechargeable Li metal batteries.

Acknowledgments

Thank you to Jie Xiao for the guidance and leadership to help me develop my understandings as a scientist and researcher. Thanks to those who helped throughout my time in the lab, Bingbin Wu, Dianying Liu, Jingnan Li, and Witness Martin listened to my rambling and provided feedback. Thank you to those collaborators Dr. Xingchen Xiao from General Motors who helped with the magnetron coating process and Dongping Lv from PNNL who helped in the training of practical aspects of battery research. Thanks to my family for supporting me and helping me. Finally, thanks to Danielle, my wife, for continual support and helping me while I strive to achieve my goals and being a crucial part of my success.

SOLI DEO GLORIA

Table of Contents

List of Figures

List of Tables

1 Introduction

1.1 Why Lithium Metal Batteries?

For the past 20 years, lithium-Ion batteries have been the topic of most battery research. These Li-ion batteries have started to realize the highest theoretical capacity when utilizing the standard carbon anode.

1.1.1 Opportunities

Lithium metal is a promising alternative to the standard carbon anode with high theoretical specific capacity (3860 mA· h g^{-}1), low molecular weight, and low redox potential (-3.04V vs. SHE) leading to a very promising high energy-dense anode. The Lithium anode functions through the simple plating electrochemical reaction as given in **Equation 1.1**:

$$Li^{+}_{solvated} + e^{-} \rightarrow Li_{solid}(-3.04V vs SHE) \tag{1.1}$$

The previous generation of anodes all operate under the insertion principle, such as graphite the most utilized anode material.[1] Specifically, as the utilization of next-generation cathodes such as sulfur and oxygen becomes more prevalent, an anode with a high capacity is needed to compliment them. This is clearly seen in **Figure 1.1** where the next generation cathodes are between 1250 Ah/kg and 3000 Ah/kg.[2] The only anodes that can support this large of capacity are Si/C composites, Si, and Li. Li metal is the main focus of this work due to the nature of its electrochemical plating and stripping.

1.1.2 Challenges

There remain two main problems that need to be solved for the application of Li metal batteries, dendritic lithium formation, and exponential solid electrolyte interface (SEI) due to the nonhomogeneous Li plating.

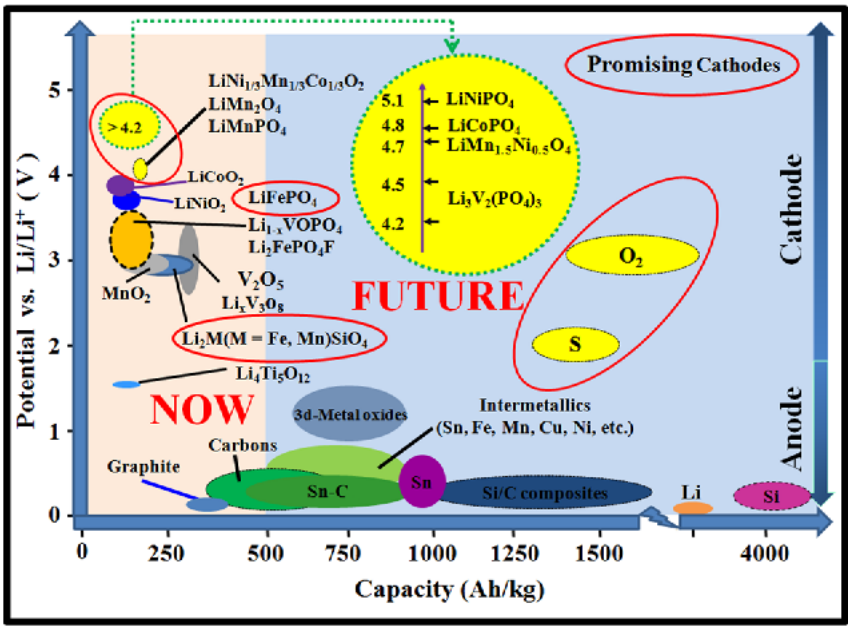

Figure 1.1: Electrode Materials and their corresponding electrochemical performances. Reproduced with permission from Ref 1. Copyright 2013 Elsevier Ltd.

Dendrite Formation

Dendrites form for various reasons, one of the main reasons for dendrite formation is Li's hyperactivity. Any area of localized high current density causes the Li to plate at that location selectively, causing a feedback loop leading to these large dendrites. Dendrites, once formed, lead to a plethora of other problems, eventually leading to cell death. **Figure 1.2** illustrates the problems due to the plating and stripping of Li metal. Li dendrites start as localized growth of Li into fibrous and tree-like shapes. Upon more substantial growth, the Li dendrite can eventually lead to the penetration of the mechanical separator between the anode and the cathode. This penetration can lead to complete cell short circuit and increased risk of thermal runaway of the battery causing massive damage (e.g., Samsung Galaxy Note exploding).[3] The internal resistance goes to 0 ohms, and the open-circuit voltage goes to 0V vs. Li^+/Li.[4] Dendrites represent the risk factor with the most catastrophic results. The catastrophic effects of the short-circuit causing thermal runaway, are mostly preceded by the disconnection between the Li and the current collector. The expansion of the Li during cycling and the loss of electronic contact is a much more prevalent issue caused

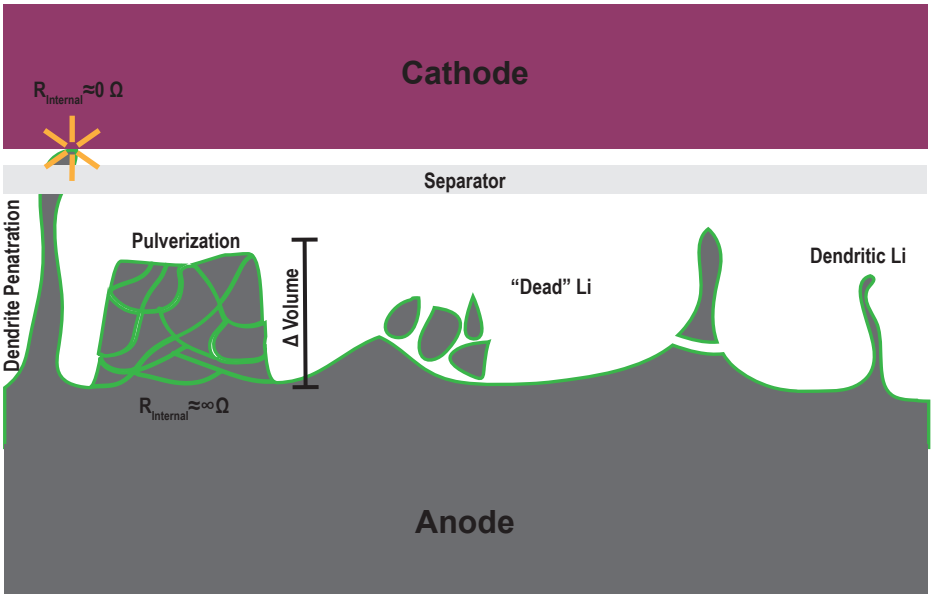

Figure 1.2: Illustration of Li Metal failure mechanisms.

by dendrites' formation, which can cause the battery to fail without any type of drop off.[5]

Dendrites further cause Li to become detached from the current collector. In the case of dendritic Li, this can occur upon charging, where the Li metal will strip from the base of the Li dendrite, eventually isolating it due to lack of electronic connection. Li upon subsequent plating and stripping starts to generate smaller deposits with higher surface area, called pulverization. The pulverized Li can break off due to lack of mechanical connection becoming electrochemical isolated.[6] "Dead" Li is a significant problem in practical battery function due to the finite amount of Li metal within a battery. If dead Li is not mitigated, eventually all active Li will be passivated, and the battery will no longer have a functioning counter electrode.

1.2 Origins of Li Dendrites

To understand the origins of Li dendrites, a foundational understanding of the nature of the electrodeposition of metals is needed. Li is a pure metal. It will almost always form a crystal structure; therefore, the deposition of Li is, in fact, electrocrystallization. This electrocrystallization is commonly split into two distinct stages: the deposition stage and the crystallization stage. In the

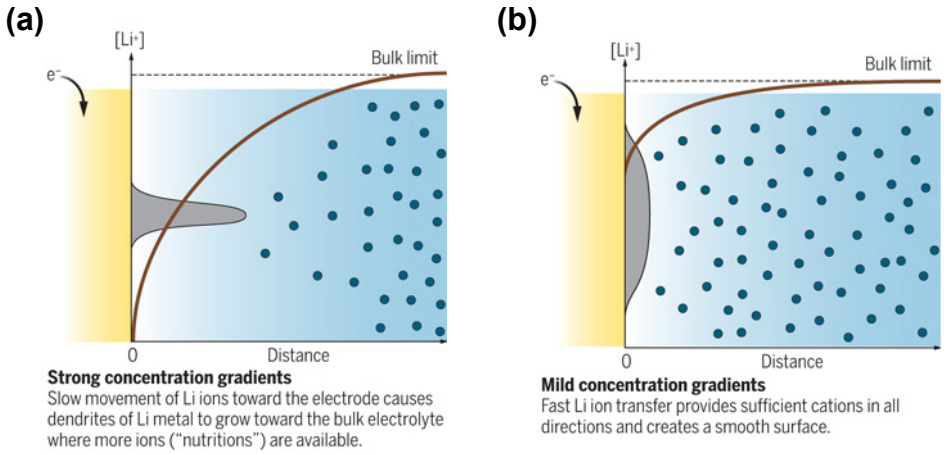

Figure 1.3: Schematic representation of the two concentration gradients during the deposition of Li metal at low diffusion (**a**) and fast diffusion (**b**). Reproduced with permission from Ref. (*7*). Copyright © 2019 American Association for the Advancement of Science

deposition stage, dendrites originate from one simple electrochemical principle: mass transport. This mass transport of the Li ions within the electrolyte determines the morphology of the plated Li.[7] The mass transport is dictated by the surface and bulk ion concentrations and their diffusion to the electrode surface. Therefore the dendrites formed through mass transport depend on the diffusion, convection, and migration of the Li ions.[7] Li metal cells are cycled in static environments, meaning that convection will impact the local diffusion speed, causing some ions to be faster and others slower. This creates localized growth dependent on the local variable diffusion due to the natural convection. In the case of diffusion, two separate scenarios are present, depending on the diffusion rate. With the assumption that no interface is formed, a slow constant diffusion rate of Li cations to the surface causes the concentration gradient to be very steep (**Figure 1.3a**).[7] This steep diffusion causes highly localized deposition with the dendrite growing outward towards the cations as the cations are depleted at the surface. On the opposite end, with a sustained fast diffusion rate, the concentration gradient is shallow (**Figure 1.3b**).[7] This causes the formation of large broad plated Li as the cations are being constantly replenished with the high diffusion rate. In the case of high current density, the depletion of Li cations is accelerated, causing the diffusion through the electrolyte to be slow, thus forming high areas of localized dendrite growths.[7] This mass transport controlled understanding of the deposition of Li metal and the formation of dendrites applies to all

metal deposition and is not a phenomenon isolated with only Li metal.

The second part of the formation of dendrites occurs during the electrocrystallization of the Li metal. Li begins its crystallization as adatoms that migrate onto the surface. These adatoms tend to diffuse on the surface of the electrode toward crystallographic sites suitable for the new phase.[8] These new sites are either supernuclei or nucleation sites.[8] The cathode affects this nucleation and adatoms due to surface conditions based on cleanliness, absorbed layers, surface oxides, and even atomistic structures.[9] All surface defects on the current collector/deposition substrate impact the adatom attachment, surface diffusion, nucleation, and growth.[9] This nucleation and growth directly impact the internal microstructure concerning grain size and shape as it evolves during deposition. Generally, additives for crystal growth allow for certain inhibitions. These inhibitions directly change the deposit structure. The metal structure can have five different deposition structures described as:[10]

- Field oriented crystals such as whiskers, dendrites, or loose crystal powder
- Basis reproduction type with coherent deposits with grain size and surface roughness increasing with deposition thickness
- Twin transition type high twin densities, materials with low stacking fault energies
- Field-oriented texture with coherent deposits with small grains throughout the whole deposition
- Unoriented dispersed type with tiny grain size

The deposit structure of Li is usually between field-oriented crystals and basis reproduction types. With the right additives, an ideal deposition structure would be the unoriented dispersed type, with the minimal grain size and an almost amorphous structure forming a thin dense structure. A deeper understanding of the metal substrate on which Li plates is important to understand what properties need to be modified to achieve the electrocrystallization needed.

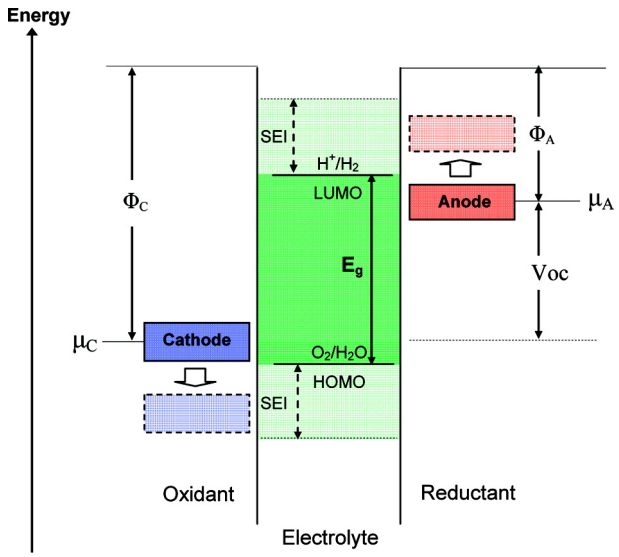

Figure 1.4: Energy diagram of aqueous electrolyte, where Φ_A and Φ_C represent the anode and cathode work functions, E_g represents the thermodynamic stability of the electrolyte. μ_A >LUMO and μ_C HOMO kinetically stabilized through the formation of an SEI Layer. Reproduced with permission from Ref. (*11*). Copyright © 2009 American Chemical Society

1.3 Solid Electrolyte Interface (SEI) Further Interferes with Smooth Li Deposition

The diffusion of ions through the SEI is one of the main causes of the SEI inducing the further growth of Li dendrites. While areas of high diffusion have been found, this uneven diffusion creates a highly uneven localized electric field, causing dendrites by the focus of the cations. Additionally, all the side reactions consume Li to form the products, decrease the net Li within the cell. This is also considered to be "dead", where this Li is no longer available for use in the electrochemical reaction for the external circuit. The high surface area dendrites and pulverized Li during cycling induces more SEI formation.

1.3.1 Electronics of the SEI

Understanding the SEI and its formation can give insight into how it affects the formation or prevention of Li dendrites. The electron energies of the electrode and electrolyte provide the basic fundamental understanding of the formation of the SEI from an electronics perspective. **Figure 1.4**[*11*] shows the schematic open circuit energy diagram of an aqueous battery, where the

cathode is the oxidant, the anode is the reductant, and E_g is the energy separation of the highest occupied molecular orbital (HOMO) and the lowest unoccupied molecular orbital (LUMO). This E_g represents the electrochemical window of the electrolyte. The anode and cathodes are electrode conductors' electrode potentials are represented by μ_A and μ_C, respectively. This creates parameters that must be met within the battery, mainly that μ_A must be below the LUMO, or else a passivation layer is needed to push it below the LUMO. The same principle applies to μ_C and the HOMO. A passivation layer must form to push the μ_C below the HOMO, thereby stabilizing the battery. The battery must operate within the electrolytes electrochemical window constraining the battery working voltage V_{oc} represented in **Equation 1.2**[11]:

$$eV_{oc} = \mu_A - \mu_C \leq E_g \tag{1.2}$$

where e represents the magnitude of electric charge. A passivating layer (SEI), as described above, can give the kinetic stability to a larger working potential given the ΔV from $eV_{oc} - E_g$ is not too great. Applying these principles to Li-ion batteries, electrodes must be found that fit in the HOMO and LUMO of nonaqueous electrolytes. As mentioned, the ideal future electrode for the next generation batteries is Li^0, however, the Fermi energy (ε_F), which in this case $\varepsilon_F = \mu_A$, lies above the LUMO of most practical electrolytes. The SEI is the reason the Li anode can work. Ideally, a good SEI has the following properties:

1. High ionic conductivity: to quickly and efficiently move Li-ions.
2. Electronically insulating: to prevent the further decomposition of the electrolyte.
3. Mechanically stable/flexible: strong enough to prevent dendrite formation mechanically, flexible enough to move with the large volume changes the anode undergoes during cycling.

1.3.2 SEI Morphology and Composition

The SEI, being formed from the reaction between the Li and the electrolyte, is composed of reductive units from both the solvent and salt of the electrolyte. The SEI structure is accepted

as under two forms: one form the mosaic structure and the other the layered structure. The mosaic structure is based on nonhomogeneous decomposition leading to localization of various products in the insoluble multiphase on the anode.

The insoluble phase as it moves out from the anode vertically towards the electrolyte and forms the two-layer structure. The innermost mosaic structure is composed mainly of the dense inorganic products, mostly Li salts, while the outer layer is composed of the larger organic decomposition products. This outer layer is generally less dense and with higher electrolytic permeability. These two layers depend mainly on the electrolyte utilized to understand and evaluate the decomposition products. In the following work, the main electrolyte used in the experimental system is ether-based, with the Li salt of Lithium bis(trifluoromethanesulfonyl)imide (LiTFSI) with the solvents Dimethyl Ether (DME) and Dioxolane (DOL), for ether electrolyte is used in the next-generation Li-air and Li-S batteries. In this case, the inorganic layer would be composed of Li_2O, LiF. Li_2CO_3, LiOH, and $LiSO_4$. The organic layer contains various polymerizations of the solvent with bases such as $R-CO_2Li$ and $R-CH_2OLi$.[12] These decomposition products are found on the surface through the use of X-Ray Photospectroscopy (XPS).

1.3.3 Ion Diffusion through the SEI

The components and makeup of the SEI, particularly the inorganic layer, are important, as they dictate Li-ion diffusion. Through multiple studies, Li-ions will be readily transported through grain bounders, porous regions, compound boundaries, interstitial sites, and vacancies.[13] The Li-ion diffusion through the various inorganic components directly dictates the localization of Li nucleation sites, playing an important in dendrite prevention. As mentioned previously, the SEI must be electronically insulating to prevent further decomposition. Upon DFT computation, the bandgap for the three main components within the SEI, Li_2O, LiF, and Li_2CO_3, is 4.7 eV, 8.9 eV, and 4.7 eV respectively, demonstrating the electronic insulating nature of the SEI. The energy barriers for the Li_2O and Li_2CO_3 are low ($\approx$0.308 eV and 0.152 eV respectively).[14] With this knowledge, modifications to the SEI can be made to optimize and direct the SEI to help mitigate

dendrite features. This is not as easy in practice because of the heterogeneous nature of the interface with multiple components in a mosaic structure. Zhang et al. found that while LiF has a high ionic diffusion barrier, when in contact with Li_2CO_3, space charging along their interface is promoted, increasing the ionic conductivity and Li transport.[15] Thus, the synergistic or antagonistic nature of the components within the SEI is still under investigation.

1.3.4 Mechanical Strength of the SEI

The mechanical nature of the SEI is essential due to the significant volume change during the plating and stripping. The SEI must be strong enough to withstand the volume change. A weak SEI will break, exposing the Li to more electrolytes increasing the SEI, and raising the resistivity. Additionally, a strong SEI can be mechanically strong enough to prevent the formation of dendrites by having a shear modulus of $\approx 10^9$ Pa.[16] While this is true for an ideal SEI, due to the mosaic nature the SEI shear modulus is always low and heterogeneous. It has been seen through atomic force microscopy (AFM) that due to the composite nature of the SEI, the shear modulus ranges from 50-400 MPa.[17,18] This shows that different areas of the SEI are strong enough to prevent dendrites, and others with weak areas have a high probability of dendrite formation. Therefore, the SEI is a conglomerate of dendrite-preventing and dendrite-inducing properties, meaning the research strives to make this more uniform.

1.4 Side Reaction Mitigations

Preventing dendrites and promoting smooth Li plating through modification of the SEI is a popular mitigation method. The nature of the SEI allows for creative solutions such as simply adding different additives to the electrolyte to incorporate them into the SEI. Other options for mitigation include forming a custom SEI before cycling in the battery or adding a different layer on top of the Li before cycling.

1.4.1 Electrolyte Additives

Electrolyte Additives are one of the first SEI modifiers to be utilized. These additives fall under two categories: sacrificial and non-sacrificial. The sacrificial electrolytes will generally decompose, adding the wanted decomposition products into the SEI to induce the desired results. The non-sacrificial additives are those compounds that are not active against Li metal but still perform the function of smoothing the plating and stripping.

One of the first electrolyte additives utilized was fluoroethylene carbonate (FEC).[19,20] This compound was first introduced into Li-ion batteries to add additional LiF to the SEI, forming a dense, LiF enriched layer.[21] This additive has made its way into Li metal batteries in carbonate systems utilizing lithium hexafluorophosphate ($LiPF_6$) ethylene carbonate (EC) and dimethyl carbonate (DMC).[22] It is effective when used as an additive in Tetraethylene Glycol Dimethyl Ether (TEGDME) with LiTFSI, forming a stable SEI enabling excellent cycle stability.[20] Vinyl Carbonate (VC) is another additive that has been utilized to stabilize the Li anode. Aurbach et al. showed that VC in equal parts EC-DMC electrolyte improved the cells cyclability while reducing its irreversible capacity loss.[23] More recently it was found that when VC was paired with $LiNO_3$, an efficiency of nearly 100% with spherical Li morphologies was achieved.[24]

$LiNO_3$ is an additive utilized as to suppress lithium polysulfides formed in Li-S batteries.[25,26] More recently it's been shown that the polysulfides and $LiNO_3$ actually play an important role in the smooth plating of Li metal. $LiNO_3$ without polysulfides (**Figure 1.5a**) shows a much worse performance than in the presence of Li polysulfides (LiPS) (**Figure 1.5b**).[27] This is because the LiPS allows for the formation of a LiF-Li_2Sx-Li_2SO_3 giving a CE of 95% .[28] Zhao et al. further expanded upon this by utilizing Li_2S_5 with LiTFSI and $LiNO_3$ as a ternary-salt system to render the desired increased CE, decreased polarization, and smooth Li plating.[29]

Other notable additives are lithium bis(fluorosulfonyl)imide (LiFSI),[30] lithium bis(oxalato)borate (LiBOB),[31] 2-fluoropyridine,[32] triprogaryl phosphate,[33] tetrachloro-1,4-benzoquinone (TCBQ),[34] and lithium difluorophosphate ($LiPO_2F_2$) all with the purpose of modifying the SEI to promote higher Li-ionic conductivity to decrease overpotential and create a more uniform nu-

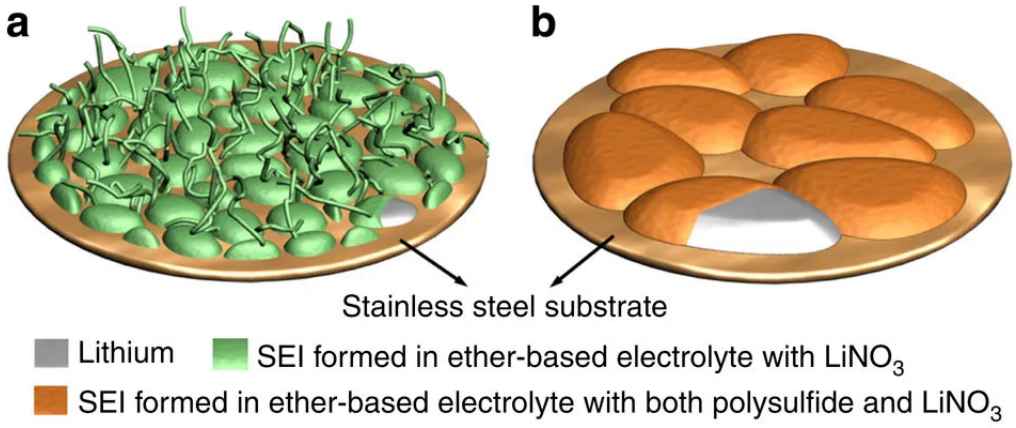

Figure 1.5: Schematic illustration showing the morphology difference of lithium deposited on the stainless steel substrate in the two electrolytes (both contain lithium nitrate), but (**a**) without LiPS (**b**) Containing lithium polysulfide. Reproduced with permission from Ref. (*27*) Copyright 2015 Springer Nature Limited

cleation of Li. These generally are more focused at prevention of dendrites than treatment of formed dendrites. While some aspects of the SEI can focus on the mechanical prevention of dendrites (LiFSI at different concentrations form thick LiF layers that can prevent the dendrites), this is generally a by-product.

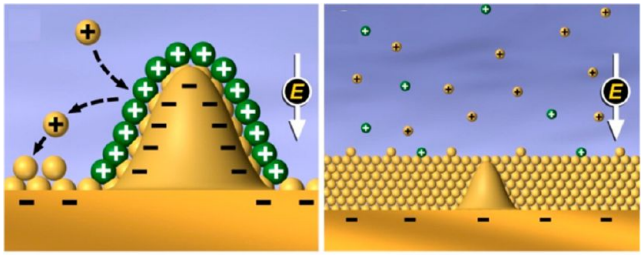

Figure 1.6: Schematic illustration showing the self-healing electrostatic shield. Reproduced with permission from Ref. (*35*). Copyright 2013 American Chemical Society

Non-sacrificial electrolytes, as mentioned, are those additives that serve the purpose of protecting and combining with the SEI without direct reaction with the Li. One of the most famous examples proposed by Ding et al. was the utilization of Cs^+ containing additives to form a self-healing SEI.[35] The cations have a lower reduction potential than that of the Li-ion. This allows them to accumulate at the tips of Li protuberances without plating, forming an electrostatic shield preventing the further plating at the tip, allowing the Li to plate more uniformly shown in **Fig-**

ure 1.6.[35] Following this same thinking KNO_3 has been shown to follow a similar mechanistic approach, utilizing the K^+ cation to create an electrostatic shield to prevent the further growth of Li dendrites.[36] However, by utilizing the -NO_3 anion, a dual purpose is formed for this additive exploiting the formation of $LiNO_3$ which has shown to improve the lithium-ion mobility within the SEI similar to $LiNO_3$.[36] Electrolyte additives by themselves show promise, but their long term commercial applicability is still to be seen, requiring other options in addition to additives.

1.4.2 Artificial SEI

Another method for modifying the SEI is creating a custom SEI with all the desired properties ex-situ then inserting it into the battery. This opens up the methodology for this application from simply chemically pretreating the Li, using electrochemical pretreatment, and even atomic layer deposition (ALD) to create the SEI one layer at a time.

Chemical pretreatment of the Li is a useful method of creating a custom SEI where the Li is treated with various chemicals to create a simpler SEI with just a few compounds. One example of this pretreatment is the use of Li-salts and N-methylpyrrolidinium bis(fluorosulfonyl)imide ionic liquids.[37] This formed a robust SEI containing mainly LiF, Li_2CO_3, and $LiSO_2F$ yielding stable cycling. Another benefit of this method is the potential to form different surface dynamics as well as chemical dynamics. Ishikawa et al. utilized a binary electrolyte containing propylene carbonate (PC), dimethyl carbonate (DMC) with the salts Li bis(perfluoroethylsulfonyl)imide ($Li(C_2F_5SO_2)_2N$) and aluminum iodide (AlI_3).[38] This created a stable SEI with residual Al forming an Al-Li alloy, helping stabilize the SEI's interfacial resistance, thereby decreasing overpotential. Other notable pretreatments include submerging the anode in H_3PO_4 and dimethylsulfoxide (DMSO) to form a single layer of Li_3PO_4[39] or using a stream of $GeCl_4$-THF to form a SEI composed of Ge, GeO_x, Li_2CO_3, LiOH, LiCl, and Li_2O.[40]

Electrochemical pretreatment is similar to chemical pretreatment but involves an electrochemical activation. An example of this type of lab formed SEI is using 1M $LiCF_3SO_3$ in TEGDME-FEC (5:1 v/v) in symmetric, Li — electrolyte — Li, cells proposed by Liu et al.[41] The

symmetric cell is cycled a couple of cycles to form a robust SEI that shows high cyclability when utilized in Li-air batteries.[41] Another aspect of this type of pretreatment is that it can utilize existing chemical methods and modify them. Mia et al. took the same principle of using AlI_3 mentioned above, but utilized it in a symmetric Li metal cell with 1M LiTFSI in DOL/DME with the aluminum iodide additive.[42] The anode was taken out and utilized in multiple full cells. They showed that the film could be a thin polymerized layer containing the Al-Li alloy and inter-dispersed Li salts with the addition of highly conductive LiI.[42] These electrochemical pretreatment methods can combine the best of both worlds, allowing for the formation of SEI's in carbonate-based electrolytes with additives that would be unstable in other electrolyte systems.

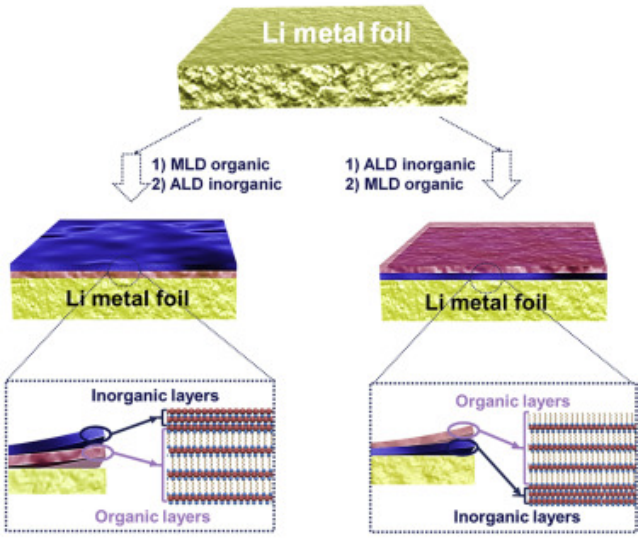

Figure 1.7: Diagram representing the dual-layer structure of the ALD/MLD layer structures. Reproduced with permission from Ref. (*43*). Copyright 2019 Elsevier Inc.

Mechanical treatment via ALD is the premier method for lab-created SEI films. The first such film that showed high promise is Al_2O_3.[44] Al_2O_3 was shown to interact with Li to form a favorable alloy layer with high levels of Li-ion conductivity.[45] This layer was found to need to be in the nm range to be effective without sacrificing too much resistance.[44] This lead researchers to go for a more hybrid approach using ALD to coat the Al_2O_3 as a thin, compact inorganic layer

while using molecular layer deposition (MLD) to deposit a compact organic layer consisting of alcuone(Al-ethylene glycol) which is generally more porous shown in **Figure 1.7**.[43] This allowed for the mimicking of the natural dual-layer structure of the SEI generated in situ. It was shown that the organic layer helped give flexibility to the ALD layer increasing the long term stability of the artificial SEI.[43] These types of pretreatment methods are good at creating the initial SEI; however, the issue remains to be determined the efficacy of these films under severe cycling conditions either deep cycling ($\geq$ 5 mAh cm^{-2}) or high current density ($\geq$ 1 mA cm^{-2}) where they can break or fail to form the more usual SEI's when exposed to the electrolyte.

1.5 Fundamentals between Metal Substrate Properties and Deposited Li

Lithium metal and its interaction with electrolytes to form an SEI is an area of great interest. The majority of research that has been done has utilized a Li|Cu cell setup to test the SEI formed on fresh Li deposited. This is a valuable test method because the actual morphology and performance of the additive can be seen more clearly as compared to Li|Li symmetric cells. This is due to the limited amount of Li within the system, particularly on the Cu anode. However, this leads us to ask the question of what is the fundamental linkage between metal substrates properties and deposited Li, and whether this influence is due to a particular metal-metal interface or crystal facet selection, or the interaction of a thin oxide layer on the substrate surface that acts as an SEI modifier.

1.5.1 Metal-Metal Interface

The utilization of the Cu current collector for the plating and stripping of Li metal is due to the Li-ion battery. Within the Li-ion battery, a current collector that was able to withstand the low potentials of the carbon anode was needed. Al would corrode at this potential, so Cu was used. After that, this has been the industrial standard. Some notable research that runs parallel with this work involves the coating of Cu with tin to induce a better Li adhesion and better subsequent cycling performance.[46] The other real research in the area of the substrate is the utilization of 3D substrates. These structures seek to address the volume change and stable cycling by providing

a structure for Li to plate within.[47–54] While this is relevant; the underlying questions still need to be addressed. This research seeks to fill this gap and study the effect the substrate has on the morphology of the Li, the subsequent SEI formed, and its long term performance.

1.5.2 Crystal Facet Impact on Li Metal

There has been some striving to understand the crystal faces interaction between Cu and Li metal. It has been shown that the Cu(100) face is lithiophilic and can help guide the plating of Li(110).[55,56] Both Kim et al.[56] and Gu et al.[55] postulate that the Cu(100) induces a thin film of Li(110) oriented Li, this causes the rest of the bulk Li to be of the said crystal structure. The theoretical calculations for the epitaxial growth of Li show that Cu(100) will theoretically induce a Li(100) thin-film due to the minimized elastic energy (meV) of ≈0.009 and a minimal coincident interface area (MCIA) of 105.7 $Å^2$.[57,58] When the substrate Cu(110) was considered the theoretical film orientation would be Li(110) with an elastic energy of 0.011 meV and an MCIA of 149.5 $Å^2$.[57,58] The question this raises is in what form is the Li that is in this orientation. The type of distribution of the Li and whether it is bimodal or unimodal determines the type and strength of the Li metal. Texture analysis on Li metal has been shown to give a good idea about the crystal orientation and distribution of the plated Lithium metal.[59] It was shown that the texture (preferential crystallographic orientation) of Li is formed during electrodeposition. The work herein seeks to fill the gap between these two sides of the story to understand the crystal face impact on the texture of Li metal at low thicknesses and at a bulk thickness.

1.5.3 Li Interface with Surface Oxide Coated Substrates

This work seeks to understand and describe the surface oxide, WO_3, as an SEI modifier. Oxides have been used as surface modifiers but not the conversion material WO_3. These other surface oxides include Al_2O_3, MgO,[60], SiO,[61] and CuO.[62] The purpose of the study of WO_3 is that WO_3 is electrochemically active with Li.[63] This material has even received research as a potential anode for Li-ion batteries.[64] WO_3 is somewhat different from other conversion materials due to its

ability to intercalate Li to form tungsten bronzes. These form through the following reaction:

$$xLi^+ + WO_3 + xe^- \rightarrow Li_xWO_3,\ x \leq 1\ (1.22V - 0.78V vs\ Li^+/Li) \tag{1.3}$$

The Li^+ intercalates into the WO_6, at the interstitial sites in the middle to form the Li_xWO_3, resulting in the W^{6+} being partially reduced with addition of the electron in the W^{5d} band.[63,65] Li, as it continually intercalates, increases the electronic conductivity until Li>0.25, this transitions the material from semiconductor to conductor state.[66] When the intercalation reaches Li=1, the WO_3 in the monoclinic phase changes to cubic perovskite structure gradually. Following this saturation, the conductivity increases and drives the conversion reaction.

$$xLi^+ + LiWO_3 + xe^- \rightarrow \frac{x+1}{2}Li_2O + W,\ 1 < x \leq 5\ (\leq 0.78V vs\ Li^+/Li) \tag{1.4}$$

After saturation, Li^{+1} ions, as they start to increase in quantity, bind with the oxygen atoms, reducing the W^{n+} and causing destabilization in the W framework. This leads to the formation of Li_2O, and the distortion continues. The W^{n+} becomes fully reduced, becoming W^0, the W framework completely collapses into amorphous W metal and Li_2O. The conversion reaction is reversible upon charging but limited due to the structure collapse and lack of electronic conductivity. This research seeks to understand the nature of this electrochemical reaction and the fundamental nature of the SEI in its formation and after long term cycling. A knowledge of this modifier will help to expand the field of surface modifiers on the current collector giving another piece to the puzzle, which is the Li metal battery.

2 Metal Substrate Effect on Lithium Metal and the Interface

Lithium metal has been frequently studied regarding having a host to plate the Li metal into, but typically Li metal is generally plated and stripped upon Cu. The understanding of the impact the substrate plays on the plating and stripping of Li metal is still unknown. In this chapter, the screening and characterization of different metal substrates are performed to determine the impact the substrate and the underlying atomistic nature has on Li metal deposition.

2.1 Li Mismatch on Substrate

A prescreening of the substrates to determine the electrochemical interactions was used to select different metals for further study. The screening includes the analysis of the coulombic efficiency (CE). CE is a metric used to understand the ratio of Li^+ in the battery system. In Li-ion batteries this is written as:

$$\begin{aligned} CE &= \frac{\text{discharge capacity}}{\text{charge capacity}} \\ &= \frac{\text{total } Li^+ \text{ returning to the cathode}}{\text{total } Li^+ \text{ departing the cathode}} \\ &= \frac{\text{total } e^- \text{ returning to the cathode}}{\text{total } e^- \text{ departing the cathode}} \end{aligned} \tag{2.1}$$

This assumes no side reactions in the electrodes.[67] With the activity of the Li metal and the significant formation of side reactions the CE for Li/Cu cells is calculated from the following equation.

$$\begin{aligned} CE &= \frac{\text{Stripped Li Capacity } (mAh \cdot cm^{-2})}{\text{Plated Li Capacity } (mAh \cdot cm^{-2})} \\ &= \frac{\text{total } e^- \text{ from stripped Li} + \#\text{ of } e^- \text{ from irreversible electrochemical reactions}}{\text{total } e^- \text{ from plated Li} + \#\text{ of } e^- \text{ from irreversible electrochemical reactions}} \end{aligned} \tag{2.2}$$

The amount of Li that is plated is held constant allowing for the stripped amount to be measured and observed. The CE includes parasitic side reactions; this can alter the CE and skew results if one set of parasitic side reactions is occurring. Therefore, while this gives a good idea about the

performance of a material with regards to the plating and stripping of Li metal, this cannot be the only metric used to determine the stability of the Li metal. Additionally, this data applies for the particular system of Li/Cu cell, a full battery consisting of Li/NMC may perform differently due to the higher potential utilized during the charging step (4.2V vs. Li^+/Li).[67]

For this work, Cu, W, Ni, Ag, and different stainless steels were screened. The stainless steel that was used is the Stainless Steel AISI 4xx series. This AISI 4xx series was used since it has a body-centered cubic (BCC) crystal structure similar to the W and the Li used, allowing for a direct comparison of crystal structure, whereas Cu, the standard substrate, is face-centered cubic (FCC) type. The three stainless steels used are AISI 410 (Fe 87.5% and Cr 12.5%) referred to as Fe87, AISI 420 (Fe 86.7%, Cr 13.0%, and C 0.3 %) referred to as Fe86, and finally AISI 430 (Fe 81%, Cr 13%, Mn $<$ 1.0%, Si $<$ 1.0%, C$<$ 0.12%, S $<$ 0.030%, P $<$ 0.040%) which is referred to as Fe81.These were tested in 1M LiTFSI in DME/DOL electrolyte. This particular ether electrolyte is utilized in next-generation Li metal batteries; therefore, it is a good standard electrolyte to utilize in a practical Li metal system. Coin cells were made utilizing Li metal as the anode and the different metal substrates as cathodes, acting as substrates for Li metal plating. They were discharged at 0.25 mA/cm^2 to 0.5 mAh/cm^2 Li and charged at 0.25 mA/cm^2 to 1.5V vs Li^+/Li. After the initial electrochemical screening when compared with Cu (**Figure 2.1**), it was found that W increased the CE of the plating and stripping of Li metal (**Figure 2.1a**) as compared to the other metals, particularly Ni (**Figure 2.1b**), which shows a performance worse than that of Cu, failing after only 10 cycles. In **Figure 2.1c**, the high CE of Ag is seen. However, this is not from the plating and stripping of Li metal, but the alloying of Li with the Ag. This will be expounded upon later. The stainless steel (**Figures 2.1d-f**) shows a very low CE with an increase in efficiency after approximately 30 cycles demonstrating underlying reactions. The initial coulombic data shows interesting results for multiple substrates. To further understand this information, two other plots are needed. The voltage vs. time graph to understand the fluctuation of the voltage polarization within the cell. The voltage polarization is a direct understanding of the bulk resistivity within the cell in a qualitative manner. The larger the distance between the plateau of plating and stripping,

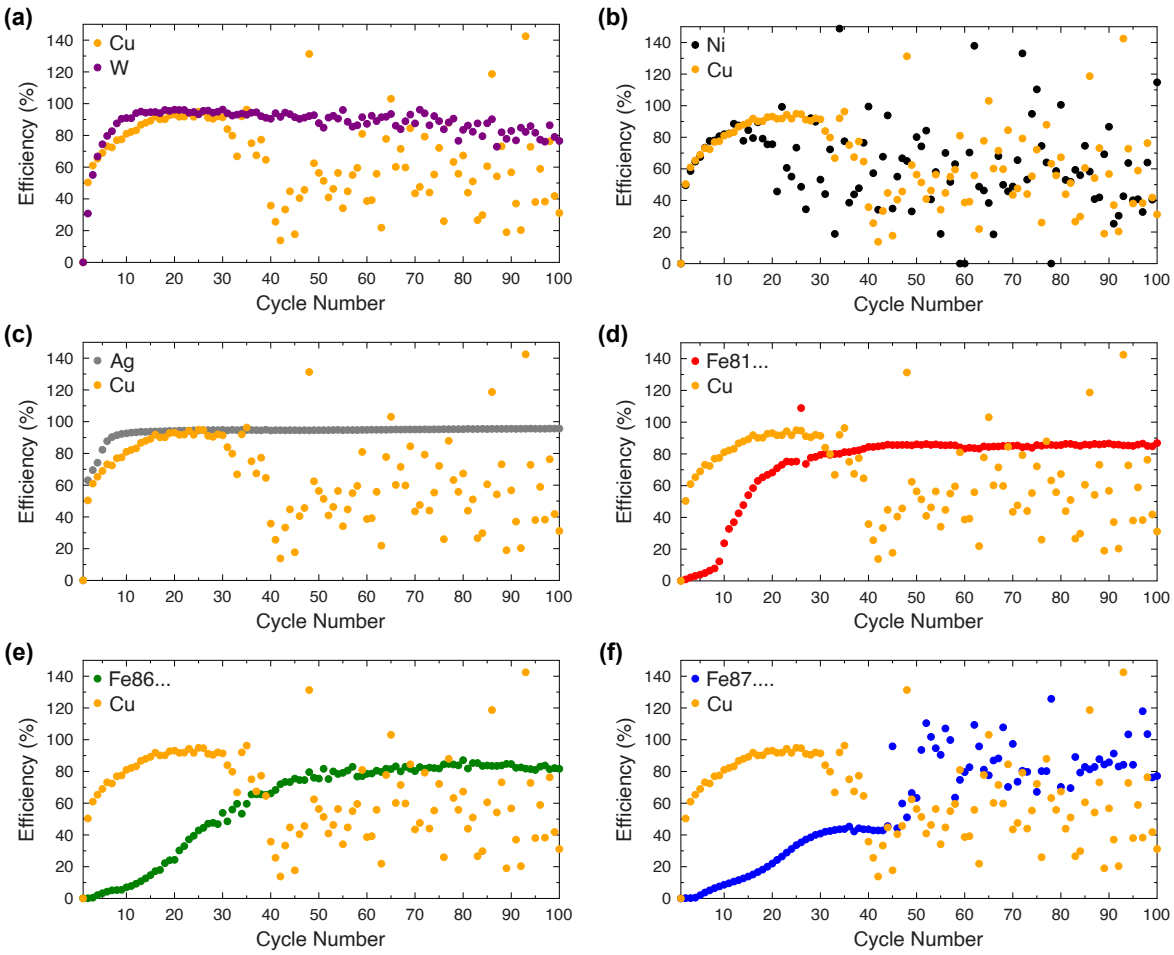

Figure 2.1: CE comparison of different metallic substrates: **(a)** W, **(b)** Ni, **(c)** Ag, **(d)** Fe81, **(e)** Fe86, **(f)** Fe87

the higher the resistance within the cell due to Ohms Law.

$$V = IR \tag{2.3}$$

Where V is the potential of the cell, I is the current, and R is the resistance. Since the cells are running under constant current, the fluctuation of the plating and stripping potential is directly due to the internal resistance. This allows for the identification of shorting (the quick drop in voltage to nominally 0V vs. Li^+/Li) and the increase in resistance usually attributed to SEI buildup. The other plot that will be examined is the voltage profile. This is graphed as V vs Li^+/Li against Areal

Capacity(mAh·cm^{-2}. This allows for the examination of the electrochemical reactions within the cell. A plateau on a voltage profile demonstrates different electrochemical reactions. In cells where only Li is being plated and stripped, one plateau should be observed for these different reactions.

2.1.1 Case Studies: Cu, W, and Ni Substrates

Cu, W, and Ni are examined due to similar metals and chemical interactions. From **Figure 2.2a**, the increase in the resistance is seen in the Li|Cu, which is indicative of the formation of the SEI. In addition, the large spikes in the negative potential demonstrate the instability of the lithium metal plating by having various nucleation over-potentials. The voltage profile in **Figure 2.2b** shows a large initial nucleation overpotential of approx. -0.05 V vs. Li^+/Li. The voltage polarization of the W substrate (**Figure 2.2c**) shows a highly stable interface with a low SEI resistance and little instability in the plating potential of the Li metal. The initial nucleation overpotential, seen in the voltage profile (**Figure 2.2d**), shows a reading much lower than that of the Cu. This stabilization is the reason for the highly stable CE seen in Section 2.1. The Ni showed a very unstable CE, as seen in **Figure 2.2e**, which reveals the highly unstable plating and stripping performance. The large fluctuations in the polarization are indicative of soft shorting. Soft shorting is the slight penetration of Li through the separator, causing the polarization to decrease close to 0V vs. Li^+/Li. This can disappear during charging by Li being stripped away.[68] A very large nucleation overpotential shows a highly resistant surface to initial Li plating. Ni, therefore, is the worst substrate to utilize for Li plating and stripping.

The impact of the substrate on the Li plating and stripping, while visible in electrochemical testing, the Li morphology is hidden. To understand the morphology, Li was plated at various capacity onto the surface of the substrate. The Cu and W substrate used in the initial screening was used due to its promising results. The SEM shows that while the Cu (**Figure 2.3a**) has a rough surface morphology, the W shows in **Figure 2.3b** a smooth surface morphology. The surface of the substrate is an important foundation, in that the rougher the substrate, the higher the surface localization of the charge, and this would be the first place on which Li plates which can increase

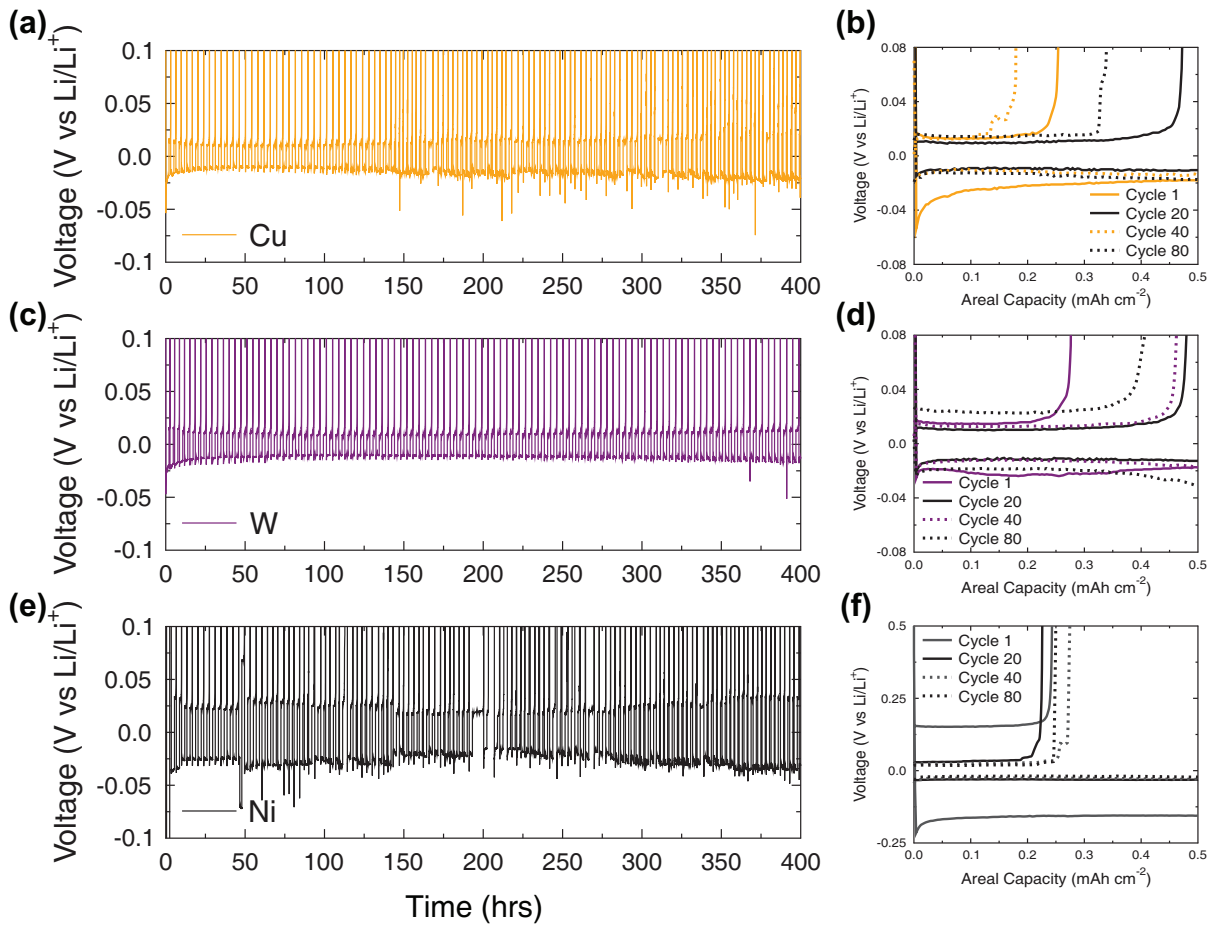

Figure 2.2: Voltage polarization and voltage profile of Cu (**a, b**), W (**c, d**), and Ni (**e, f**) respectively.

the likely hood of dendrite formation.[69] After 1 mAh cm^{-2} of Li was plated on the substrates, the morphology was then examined by SEM. The SEM reveals that the Li on the Cu substrate (**Figure 2.3f**) has a mossy like structure with rounded tips, this is consistent with other results on the morphology of Li in the ether electrolyte. The morphology of the Li on W in **Figure 2.3g** shows a quite smooth morphology, which is interesting and differs completely from that of the Cu. Upon further plating to 3 mAh cm^{-2} the Li morphology changes on the substrates. The Cu (**Figure 2.3k**) shows an increasing prominence of the mossy structure, and the W (**Figure 2.3l**) starts to show fibers growing laterally. The development of the Li as it is plated in increasing amounts demonstrates an interaction between the surface and the Li. As more and more Li is plated, the positive effects of the surface start to be minimized, and the Li starts to resemble that of mass

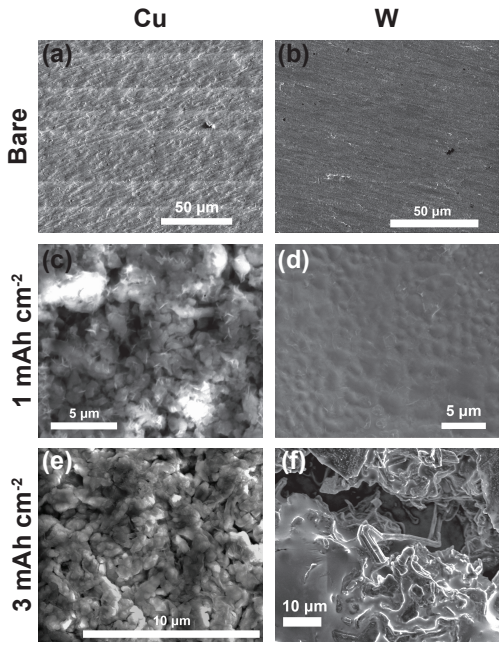

Figure 2.3: SEM of bare Cu (**a**) and W (**b**); 1 mAh cm^{-2} Cu (**c**) and W(**d**); and 3 mAh cm^{-2} of Cu (**e**) and W(**f**).

transport regulated Li. This raises the question about the mechanism by which the Li is smoothed. The interactions between the substrate and Li would be evident in the SEI, which develops on the surface during plating. The surfaces will be analyzed in the next section to try to determine the mechanism by which the Li is modified.

2.2 Quantification of Surface Films Formed on Different Substrates

To determine the lithium plating mechanism, XPS was performed on the substrate's bare surface to analyze the properties therein. Following this testing, the substrates were discharged at constant current to 0V vs. Li^+/Li, followed by XPS studies. This represents the SEI precursor, which will directly affect the morphology of the plated Li with the elimination of Li metals impact. XPS was performed on the Cu and W due to the high impact the W has on the Li. The XPS revealed that the W has WO_3 on the surface, and this appears in the W4f (**Figure 2.4a** spectrum at approx. 36 eV, the typical peaks from the W metal appear at approx. 32 eV. The O1s for the W in **Figure 2.4b** shows the WO_3 peak at 531 eV and the peak for the C=O and N=O from

atmospheric absorption on the surface. In **Figure 2.4c**, the bare Cu in the Cu2p region shows the

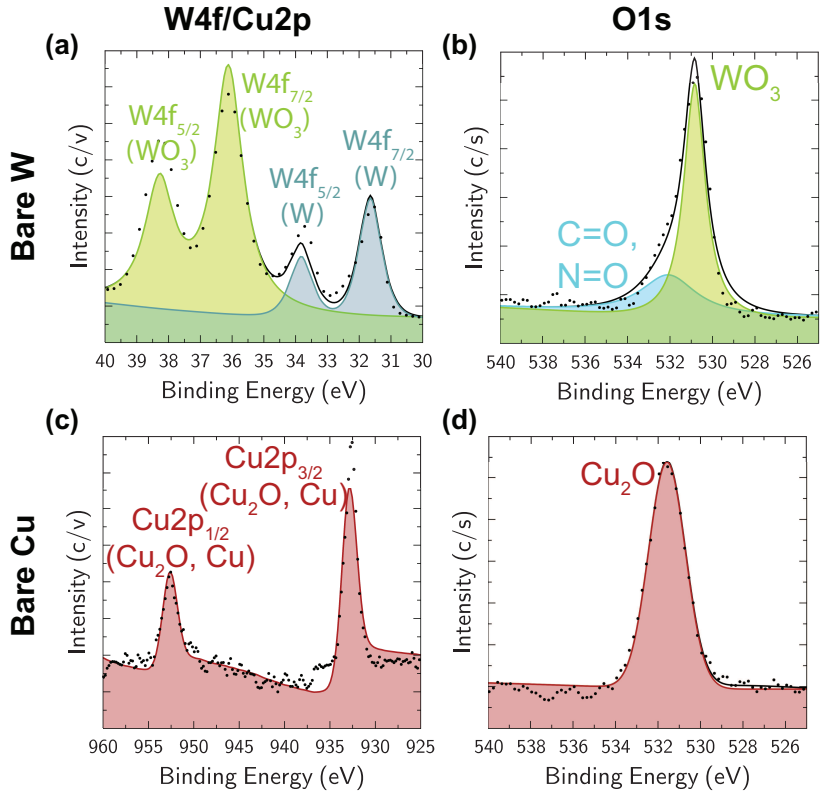

Figure 2.4: XPS of bare W in the W4f region (**a**) and O1s region (**b**) and bare Cu in the Cu2p region (**c**) and O1s region (**d**).

peaks indicative of the Cu_2O and Cu. This region overlaps, so the O1s (**Figure 2.4d**) confirms the presence of the surface oxide and just the bulk metal. The interaction may be that of the surface oxide. Both WO_3 and Cu_2O are both electrochemically active with Li metal. They are considered conversion materials. The conversion reaction follows the pattern of

$$M_aX_b + (b-c)Li^+ + (b-c)e^- \rightarrow aM + bLi_cX \tag{2.4}$$

where M is in this case, W or Cu, and X is oxygen. The effect of this conversion reaction on the Li is to be investigated. The precursor SEI that is formed after discharging to 0V vs. Li^+/Li dictates the initial morphology of the Li, which can be found through the XPS measurements of the surface after this discharge. **Figure 2.5** shows the F1s, C1s, O1s, C1s, S2p, and W4f regions for Cu and W

respectively. The F1s for Cu (**Figure 2.5a**) show that the ratio of LiF to the C-F that correlates to

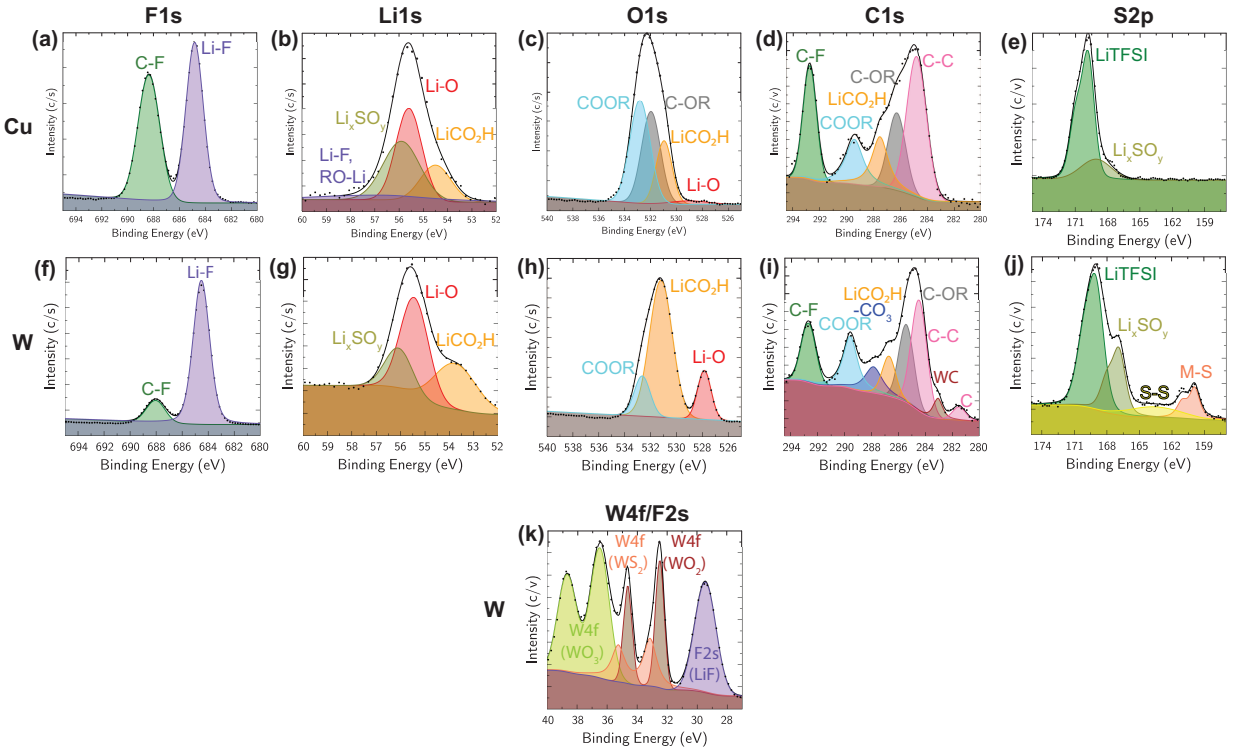

Figure 2.5: XPS of Cu in the F1s region (**a**), Li1s region (**b**), O1s region (**c**), C1s region (**d**), and S2 region (**e**); and W discharged to 0V vs. Li^+/Li in the F1s region (**f**), Li1s region (**g**), O1s region (**h**), C1s region (**i**), S2 region (**j**), and the W4f/S2p region (**k**).

the LiTFSI salt is in a similar ratio with a higher response to the LiF. The Li1s in **Figure 2.5b** shows the presence of $LiCO_2H$ at 54 eV, Li-O at 55.6 eV, Li_xSO_y at 56 eV and LiF at 58 eV, these products are the main byproducts of the reaction of Li with the solvent forming Li-O and $LiCO_2H$; with the Li_xSO_y and Li-F being formed from the decomposition of the salt LiTFSI. The decomposition of the solvent is further seen in the O1s (**Figure 2.5c**), and the C1s (**Figure 2.5d**) plots that reveal the components of COOR, C-OR, and C-C formed from the solvents. The S2p for Cu in **Figure 2.5e** shows the salt and the lithium sulfate formed from the reaction of Li with the salt. When the surface of the W at 0V vs. Li^+/Li was examined, there are a few things to notice. In the F1s region (**Figure 2.5f**), the ratio of C-F to Li-F is much greater than that of the Cu. The Li1s (**Figure 2.5g**) and O1s (**Figure 2.5h**) both show similar constituents to that of the Cu, with an increase in the amount of the $LiCO_2H$. **Figure 2.5i** is the C1s for W at 0V vs. Li^+/Li and shows two new peaks

that correspond to WC and CO. The CO is attributed to atmospheric interference. The WC peak at 283 eV indicates some interaction between the W and the electrolyte. The S2p region (**Figure 2.5j**) reveals new peaks as well at 163 eV and 160 eV. These are attributed to the S-S bond and the M-S bond, respectively. M-S can be the Li-S bond or W-S bond; the latter assignment is supported when the W4f region is examined. The W4f region shows the WO_3 at 36.5 eV. In addition to this peak, two new peaks are seen with WS_2 at 33.1 eV corroborating the assignment of the S2p peak to the W-S bond. Additionally, the WO_2 peak arises, stemming from the decomposition of WO_3 with Li. The F2s region is right beside the W4f region, and the LiF peak is seen at 29 eV in this region as well. The XPS of these precursors shows that there is an additional decomposition of the LiTFSI salt that does not occur on the Cu. However, this does not appear as much with regards to the solvent in the electrolyte. To further understand the relationship between the substrate and electrolyte, additional analysis is needed.

2.3 Electrochemical Kinetics

The understanding of the interaction between substrate and electrolyte can be analyzed through Tafel analysis. Tafel plots are used to calculate the plating exchange current density to understand the interface reactions. The exchange current of the plating of Li on the surface is quantified, using the Bulter-Valmer equation:

$$j = j_0[e^{-\alpha f\eta} - e^{(1-\alpha)f\eta}] \tag{2.5}$$

where the j_o is the exchange current density, η is the overpotential, and α is the transfer coefficient. Utilizing a microelectrode allows for the negation of mass transport effects as well as minimize the SEI formation. When graphed as $\log \mid j \mid$ vs. η, the y-intercept of the fit is $\ln j_0$, and the slope is $-\alpha f\eta$ for this cathodic range. Since mass transfer effects are mitigated, the overpotential at a specific current is solely derived from the activation energy to drive the heterogeneous process. This means that low activation energy indicates sluggish kinetics giving rise to higher overpotentials.[70]

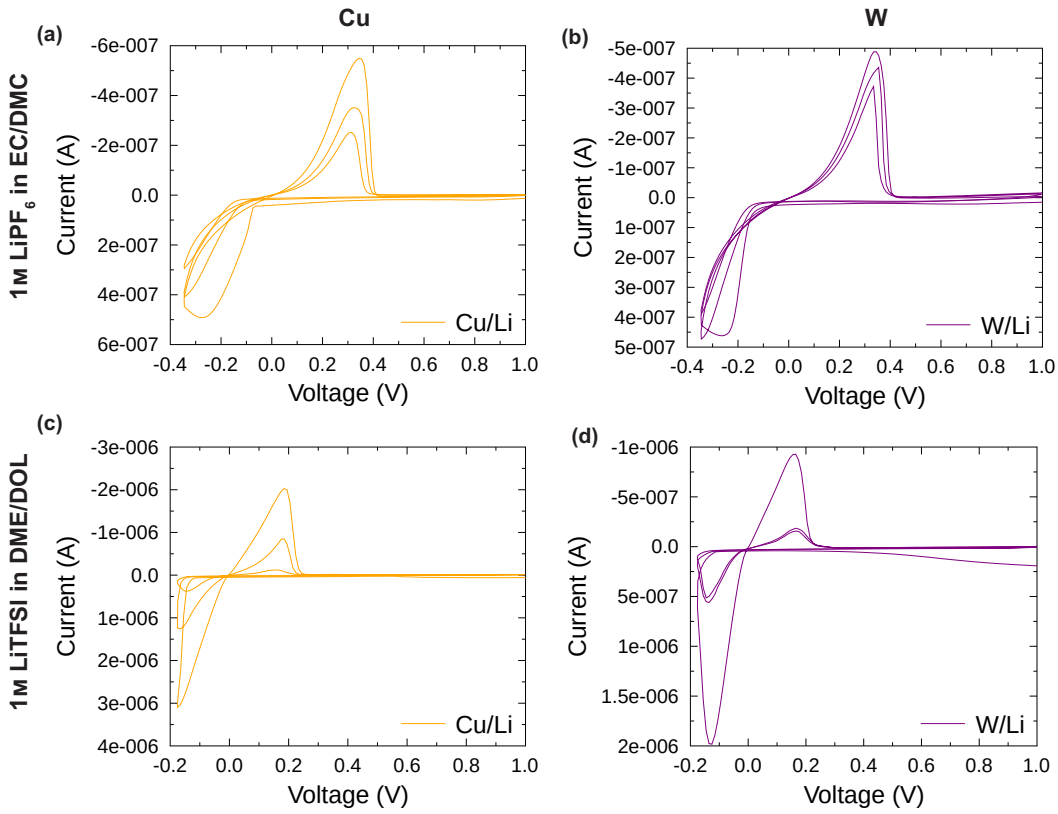

Figure 2.6: CV of Cu (**a**) and W (**b**) in 1M $LiPF_6$ in EC/DMC, Cu (**c**) and W (**d**) in 1M LiTFSI in DME/DOL

Due to the relation:

$$j_0 = Fk^0C \tag{2.6}$$

assuming the $C_O^* = C_R^* = C$, where C is the concentration at the surface of reactants, F is faraday constant, and k^0 is the rate constant, showing that the exchange current is proportional to k^0 giving an understanding of the kinetics of the plating on the surface of the metal. The Tafel plots were extracted through the use of cyclic voltammetry (CV) using microelectrodes (25 μm diameter) of

Table 2.1: Stripping capacity and exchange current of the microelectrodes.

Sample	1st Positive Scan ($\mu m \cdot cm^{-2}$)	2nd Positive Scan ($\mu m \cdot cm^{-2}$)	3rd Positive Scan ($\mu m \cdot cm^{-2}$)	j_0 mA·cm^{-2}
Cu(Carbonate)	5.68	5.25	1.54	350
W(Carbonate)	4.67	3.64	3.31	13.7
Cu(Ether)	5.28	3.05	.379	3.9
W(Ether)	12.2	.484	.465	3.6

Cu and W, using the first negative scan from the CV. The CV was performed using Li as both the counter and reference electrode at a scan rate of 100 mV/s. The test began at the open-circuit voltage (OCV) and scanned negatively first to -0.35 V vs. Li^+/Li then back to 1V vs. Li^+/Li for 1M $LiPF_6$ in EC/DMC and to -0.18V vs. Li^+/Li to 1V vs. Li^+/Li for 1M LiTFSI in DME/DOL these specific voltages were used to prevent SEI formation by higher reduction potentials. The carbonate and ether electrolytes were both used to decouple any electrolytic effects from the substrate. The CV of the Cu (**Figure 2.6a**) shows a large initial plating peak and a large stripping peak. This current response diminishes after the first scan and continues through the third scan. The W, however, in **Figure 2.6b**, shows a similar peak as the Cu the difference starts to appear upon the second and third scan, the current response stays the same with very little diminishing of the current. This is clear when the area under the curve of the stripping peaks are examined in **Table 2.1**. The Cu stripping capacity drops from 5.68 μm·cm^{-2} to 1.54 μm·cm^{-2} a diminishing capacity of ≈4.14 μm·cm^{-2}. The W starts with a lower capacity of 4.67 μm·cm^{-2} but only drops by 1.36 μm·cm^{-2}. The Cu in the ether electrolyte (**Figure 2.6c**) shows a performance, not unlike the carbonate with the diminishing current response of the stripping of Li much greater between 1 and 3. The W shows a high current response initially, then a stabilization of current responses after the first scan (**Figure 2.6d**). This shows stabilization in the interface of the W, which diminishes the continuous resistance of the interface, decreasing the potential of Li plating seen in Cu. The capacity of the stripped Li on the W, however, diminishes greatly after the first cycle, revealing an interfacial change causing a decrease in the capacity of the stripping.

The Tafel of Cu in the carbonate electrolyte shows a high j_0 of 350 mA cm^{-2} (**Figure 2.7a** & **Table 2.1**). In **Figure 2.7b** the Tafel of the tungsten shows a decrease in j_0 of 13.7 mA cm^{-2}. The Cu, therefore, shows a low activation energy for the plating of Li than that of the W. The ether, however, shows that the Cu (**Figure 2.7c**) has a decreased j_0 of 3.9 mA cm^{-2} and on the W (**Figure 2.7d**) the j_0 is very similar at 3.6 mA cm^{-2}, to that of Cu. This shows that while the CV demonstrates stabilization of plating on W, the actual activation overpotential needed to plate Li is very similar to that of Cu in the ether electrolyte and Cu much lower in carbonate. Therefore, the

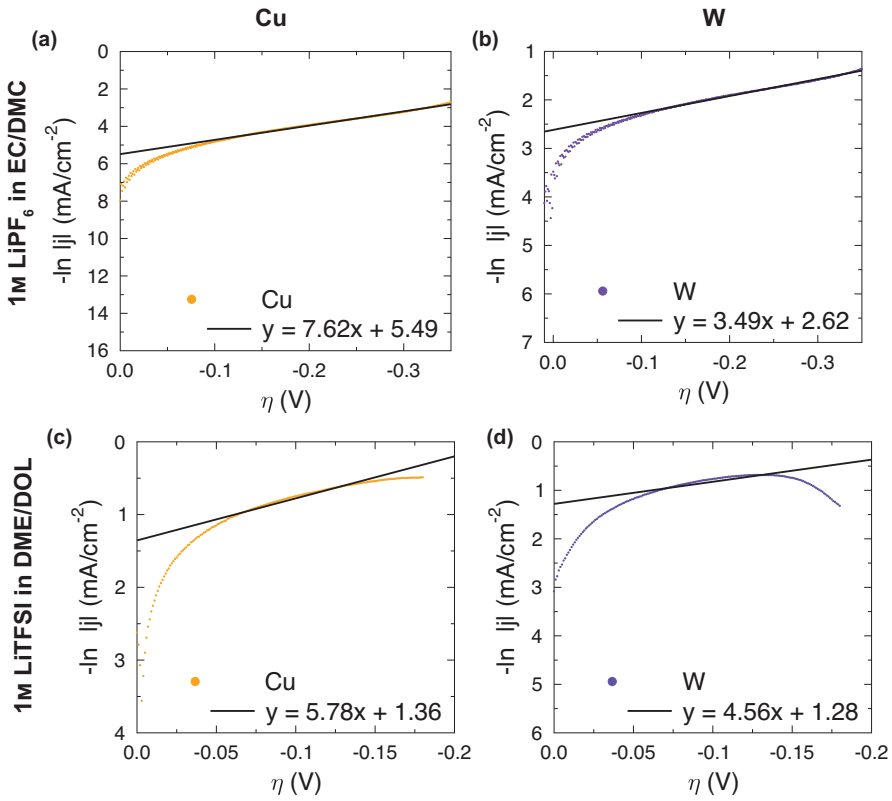

Figure 2.7: CV of Cu (**a**) and W (**b**) in 1M $LiPF_6$ in EC/DMC, Cu (**a**) and W (**b**) in 1M LiTFSI in DME/DOL

alteration of the Li plating seems to stem from differing surface impurities or modified SEIs rather than an innate difference in the activation energy of the plating of Li metal on the bulk metal lattice of Cu or W.

3 Impacts of Specific Metal Lattice Faucets in SEI Properties and Li Morphologies

3.1 Introduction

As mentioned in Chapter 1, surface conditions based on cleanliness, absorbed layers, surface oxides, and even atomistic structures affect the nucleation of Li metal. The microelectrodes and the general electrochemical testing of the Cu and W were all performed on polycrystalline substrates. The understanding of the factors affecting the nucleation of Li leads to question the atomistic impact of the substrate on Li metal. The atomistic structure of the surface that a material is crystallizing on affects the type of crystals formed and their orientations. Therefore, textures within the Li plated structure are explored. The hypothesis, therefore, is that, firstly, the crystal nature of the substrate that Li plates on will change the texture of the Li metal giving rise to particular textures depending on the substrate; secondly, the pressure of the cell and type of separator give preferential orientations based on the slip strain of Li.

3.2 Single Crystal Impact on Li Metal

Following alongside the previous testing, three single-crystal substrates were chosen to test the hypothesis: Cu(100), Cu(110), and W(100). Cu was chosen as it is the standard substrate, and some previous work, addressed in the introduction, shows preferential plating of Li depending on the crystal face. W was chosen as it is a stable metal of the BCC crystal structure, adding the additional testing of FCC vs. BCC with the Cu vs. Li and BCC vs. BCC for W vs. Li.

The single crystals as received show rough structure under SEM in **Figure 3.1a-c** for Cu(100) and Cu(110), while the W(100) shows a relatively smooth substrate at this resolution. After mechanical polishing with 8000 grit polishing foam and subsequent alumina oxide paste, the surfaces look more uniform in smoothness/roughness. This allows for an accurate comparison concerning the impacts of roughness. The Cu(100) (**Figure 3.1d**) and Cu(110) (**Figure 3.1e**) show a drastic reduction in the large striations due to the cutting blade for preparation of the single crystal substrates. The W(100) after polishing (**Figure 3.1f**) shows a slight increase in roughness

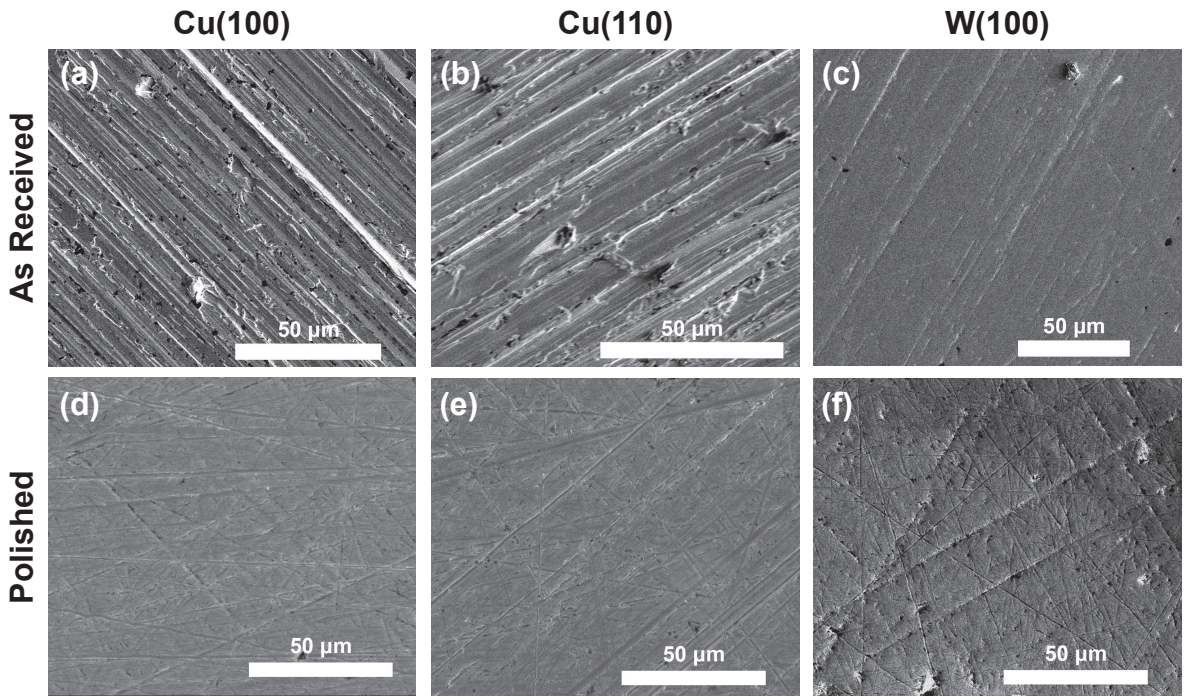

Figure 3.1: Surface morphology of as received single crystal substrates (**a-c**) and polished substrates (**d-f**) of Cu(100), Cu(110), and W(100).

compared to the as-received though putting it on par with the other single crystals. The XRD (**Figure 3.2**) of the bare single crystals shows the high signals of the various crystal represented with Cu(100), showing the Cu(200) face at 50.3°, and the Cu(110) the Cu(220) face at 74.13°. The W(100) shows the W(200) peak at 53.3°. To the left of each single-crystal peak, there is a peak corresponding to the kβ residual peaks due to the high intensities of the single peaks. The XRD shows that the substrate is composed of a single crystal compared to the reference patterns. Initially, the cells were tested against Li metal using the plating protocol from previous chapters in ether electrolyte, to verify the removal of the surface layer and whether there was an intrinsic difference in the long term effects due to the single crystal substrate. In **Figure 3.3**, the electrochemical performance through 100 cycles is shown. The initial nucleation (**Figure 3.3a**) shows Cu(100) and W(100) have relatively the same nucleation energy than that of the Cu(110), showing that Cu(110) has a lower resistance to Li nucleation than that of the other two substrates. During cycling, the CE (**Figure 3.3b**) shows the stability of the Cu(110) substrate compared to the Cu(100)

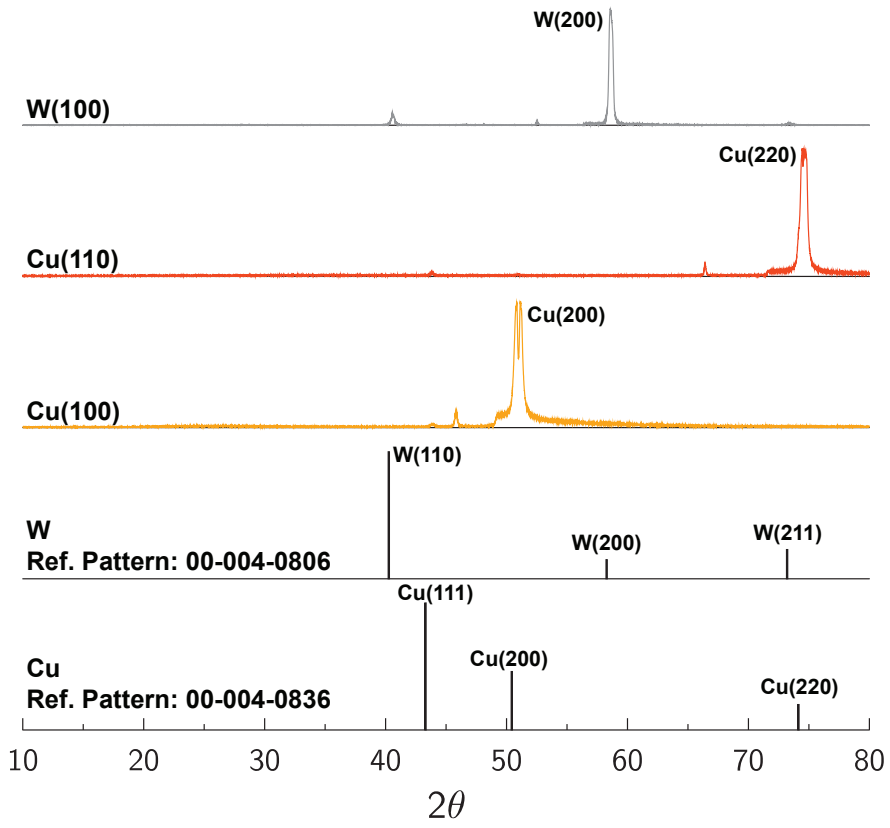

Figure 3.2: XRD of single-crystal substrates with reference patterns.

and W(100), with it being stable through 30 cycles before becoming unstable shown by the high hysteresis.

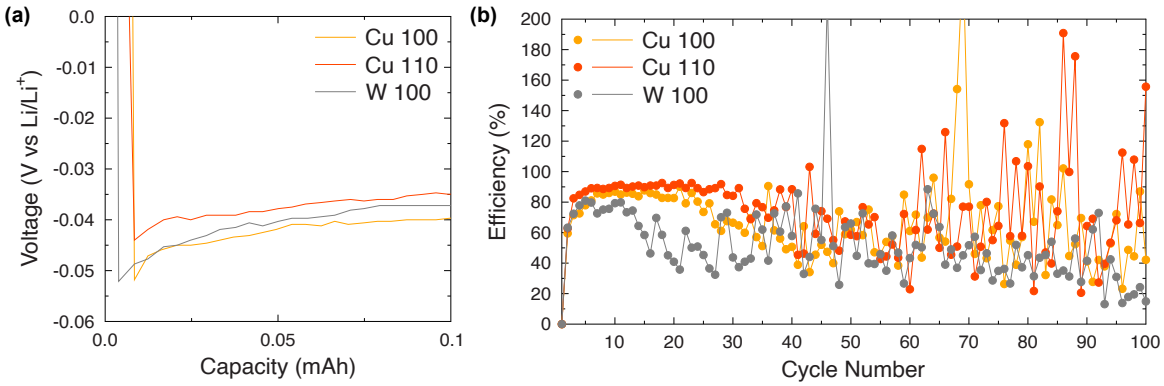

Figure 3.3: Electrochemical results of the single crystal substrates. (**a**) First cycle nucleation overpotential and (**b**) CE of cycled single crystals.

3.3 Understanding the Deposition of Li on Single Crystal Metal Substrates

Understanding the deposition of the Li on the substrates requires a fundamental knowledge of the morphology of the Li metal. The examination of the lithium nucleation morphology reveals

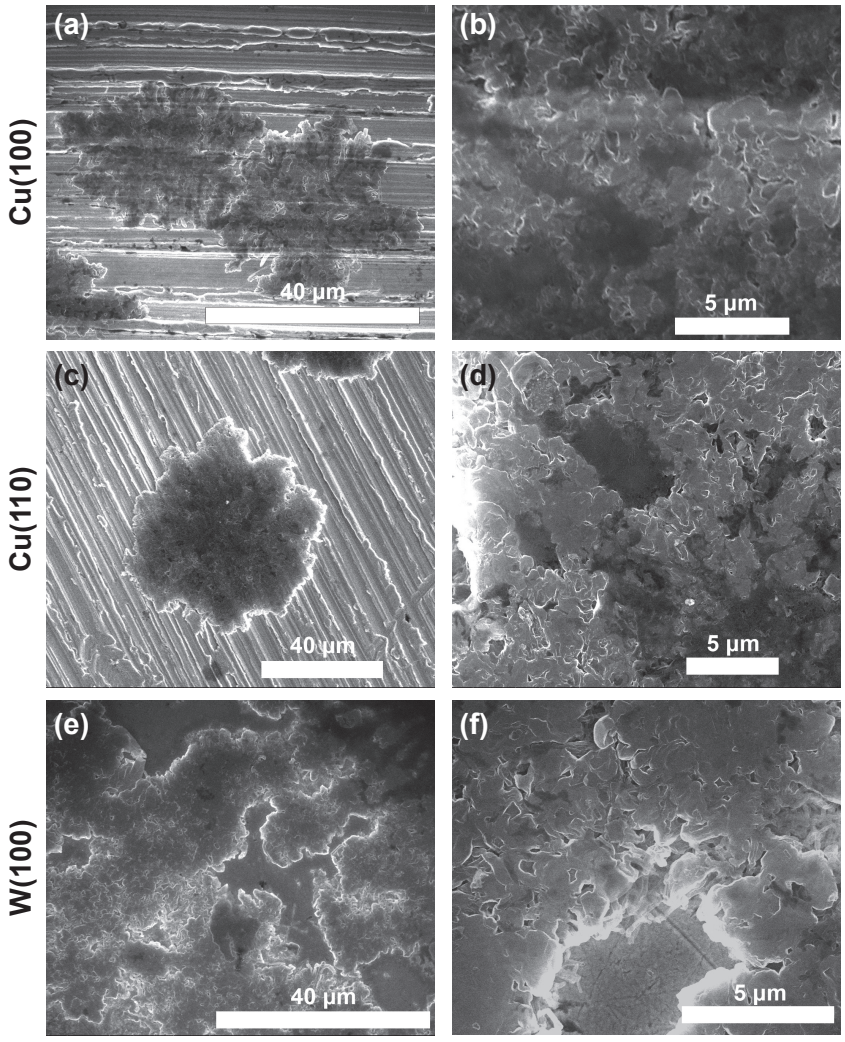

Figure 3.4: SEM of Li nucleated on the single crystal substrate Cu(100) (**a-b**), Cu(110) (**c-d**), and W(100) (**e-f**).

a similar morphology between all three substrates. The SEM reveals the Li has similar nucleation pattern between the Cu(100) (**Figure 3.4a & b**) and Cu(110) (**Figure 3.4c & d**). The Li plates in circular patterns and flattened, mossy, close morphology. The W(100) shows a more sprawling less organized nucleation, with a mossy morphology similar to that of the other two substrates (**Figure 3.4e & d**). This shows there is parity between the substrates with no major variants in the

observable morphology of the plated Li.

3.3.1 SEI Quantification

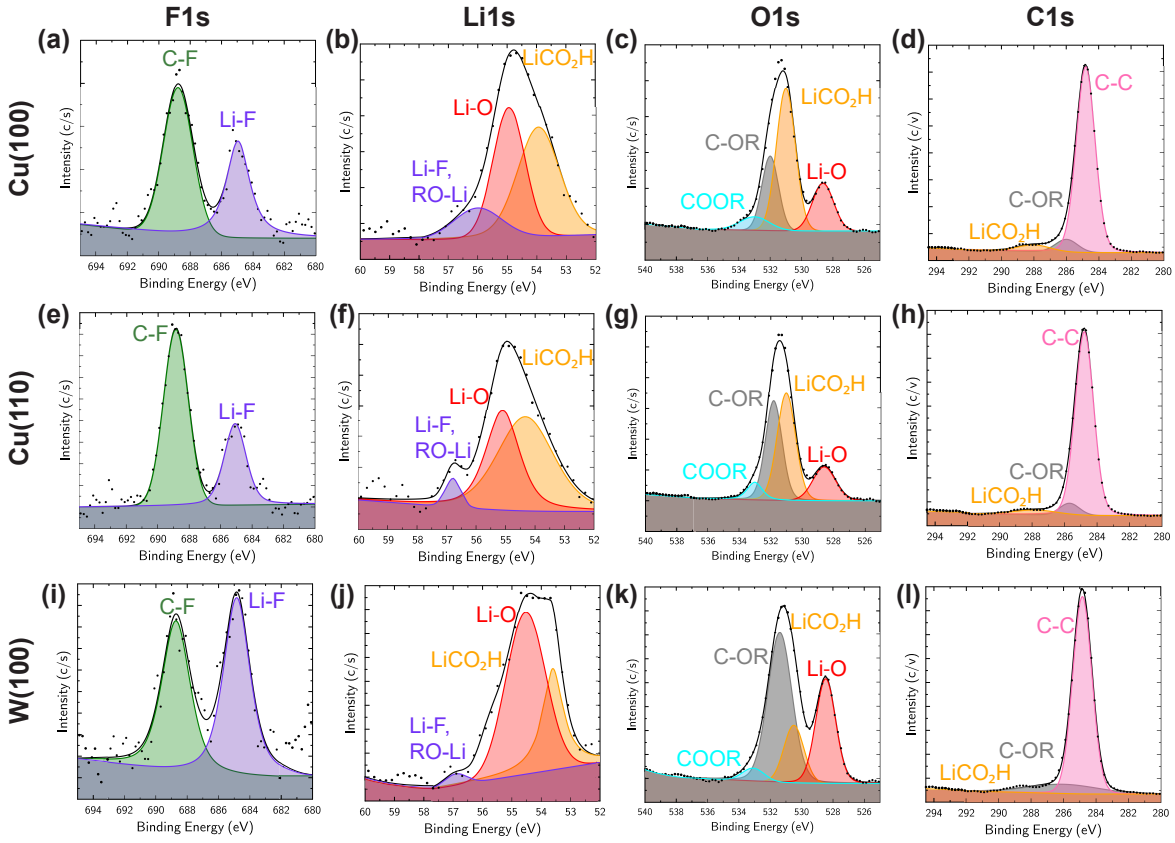

Figure 3.5: XPS of Cu(100) in the F1s region (**a**), Li1s region (**b**), O1s region (**c**), and C1s region (**d**); Cu(110) in the F1s region (**e**), Li1s region (**f**), O1s region (**g**), and C1s region (**h**); and W(100) in the F1s region (**i**), Li1s region (**j**), O1s region (**k**), and C1s region (**l**)

To further understand the nature of the interaction of the substrate with the plating of Li metal, the SEI is observed using XPS at 0V vs. Li^+/Li in **Figure 3.5** the similarities between the substrates is further demonstrated. The Cu(100) shows higher C-F peak than Li-F in the F1s (**Figure 3.5a**) with components in the Li1s (**Figure 3.5b**), O1s (**Figure 3.5c**), and C1s (**Figure 3.5d**) showing Li-O, C-OR, COOR, $LiCO_2H$, and C-C corresponding to the breakdown of the electrolyte and advantageous carbon. The Cu(110) (**Figure 3.5e-h**) and W(100) (**Figure 3.5i-l**) show the same components as Cu(100) with similar intensities with exception to that of Li-F and

Li-O in W(100) showing a marked increase in both of these peaks, reiterating the SEI advantage pure W has on the SEI formation. While this is an improvement, it is not such a great improvement that the underlying study of the crystal structure is not impeded.

3.3.2 Microstructures of Deposited Li on Single Crystal Substrates

While thus far, the single crystals show marginal differences in electrochemical screening, Li morphology, and SEI components, the impact the single crystal substrates on the crystallinity of the Li metal has yet to be identified. To understand this impact, XRD is utilized on the plating of Li at two separate thicknesses: 20 μm and 200 μm. These two thicknesses allow for the

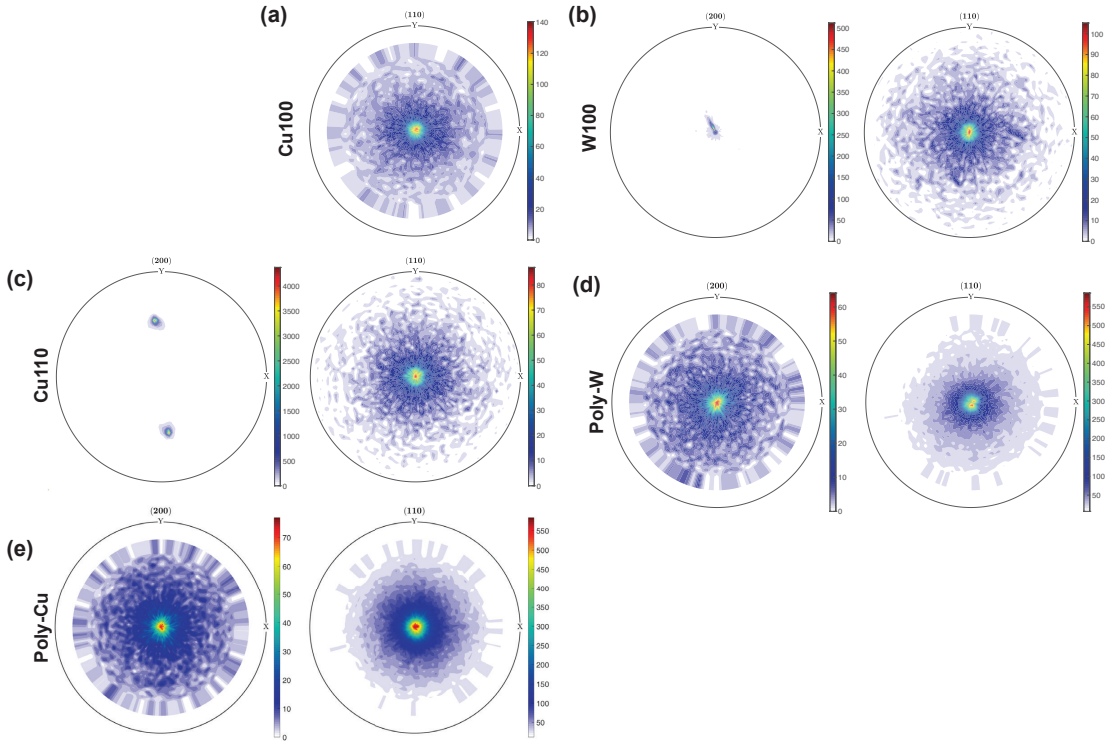

Figure 3.6: Pole figures of single and polycrystalline samples plated to 20 μm for Li(110) peaks and Li(200).

testing of the substrate impact before bulk characteristics of Li metal plating comes into play (20 μm) and after (200 μm). Additionally, polycrystalline Cu (poly-Cu) and polycrystalline W (poly-W) were tested alongside the single crystals as control variables. The microstructure of Li is

identified by using texture analysis of the Li metal. As mentioned in Chapter 1, in regards to Li metal, one study has performed texture studies on Li metal using different electrolytes on a poly-Cu substrate. Additionally, the texture that was identified uses a different cell design than the cell design presented here. The cell design used for the previous texture studies utilized a hollow spacer between the separator and the plating substrate to eliminate the pressure impact on the texture. No such spacer has been utilized in this work, allowing for the full examination of substrate effects and pressure effects. All substrates after an initial plating of 20 μm were disassembled and prepared for XRD under a pure Ar atmosphere described in the appendices. Pole figures of Li(110) and Li(200) were obtained (**Figure 3.6**) giving two separate crystal planes to determine texture, however at such low thickness of Li the Li(200) peak was unable to be obtained for the Cu(100) due to the signal of the Cu(200) peak overlap. The Li(110) for the Cu(100) shows a singular point in the center of the pole figure. Showing that Li(110) has the highest intensity at $\phi \approx 90°$. This texture is

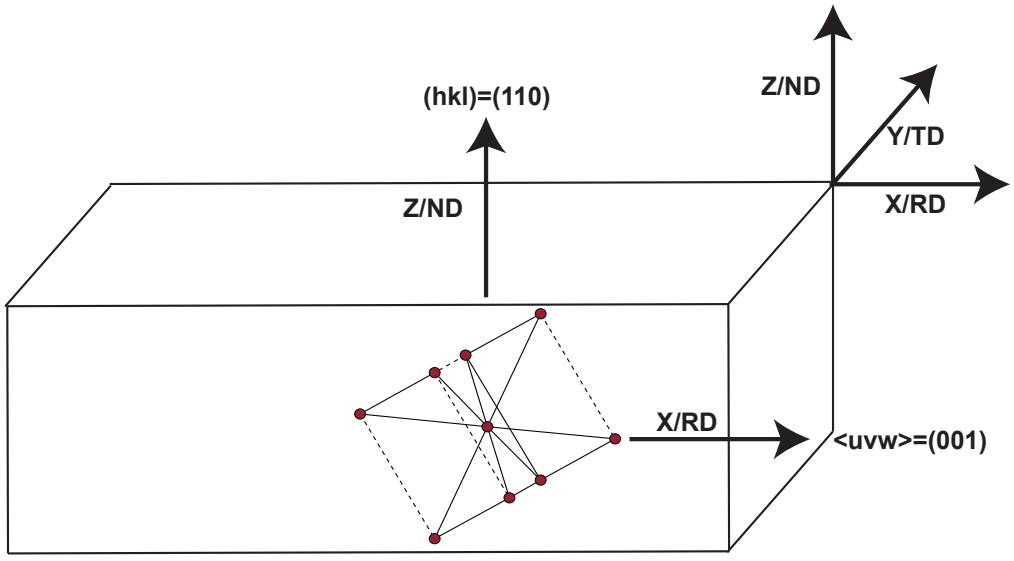

Figure 3.7: Schematic showing the 3D orientation of the Goss texture.

concentrated within $\phi \approx 10°$of 90°. The W(100) shows a similar texture to that of Cu(100) in the Li(110) plane, however in the Li(200) plane, the intensity of the peak is much great than that of the Li(110) going from 100 to 500 cps. Showing the Li(200) is highly oriented at 90°with a directional component. For Cu(110) the change in the Li(200) is shown further, with 2 points at ψ of $\approx 44°$

and ϕ of $\approx 10^{\circ}$ and 190°, corresponding to the Li(110) planes. This shows the Li is highly oriented with respect to the Cu(110) plane in an epitaxial manner following the basis-oriented reproduction (BR) type electrocrystallization.[9] The poly-W (**Figure 3.6d**) shows a similar pole figure to that of W(100), with a much greater variation in Li(200) than that of the W(100). The impact of the substrate has a decreased effect due to the polycrystalline nature of the substrate. Furthermore, the intensity difference between Li(110) for poly-W than for W(100) is much greater on the poly-W, demonstrating the W(100) similar to the Cu(110) follows the basis-oriented reproduction type electrocrystallization. The poly-Cu (**Figure 3.6e**) shows similar pole figures to the poly-W with the Li(110) having a higher intensity and a much larger radius around the center, showing a much greater variation of the orientation of both planes. Pole figures are 2D representations of 3D data, in order to requalify the 3D data, the Orientation Distribution Function (ODF) is needed. The ODF is the probability density function of orientations using the Euler angles of φ_1, Φ, and φ_2. The ODF

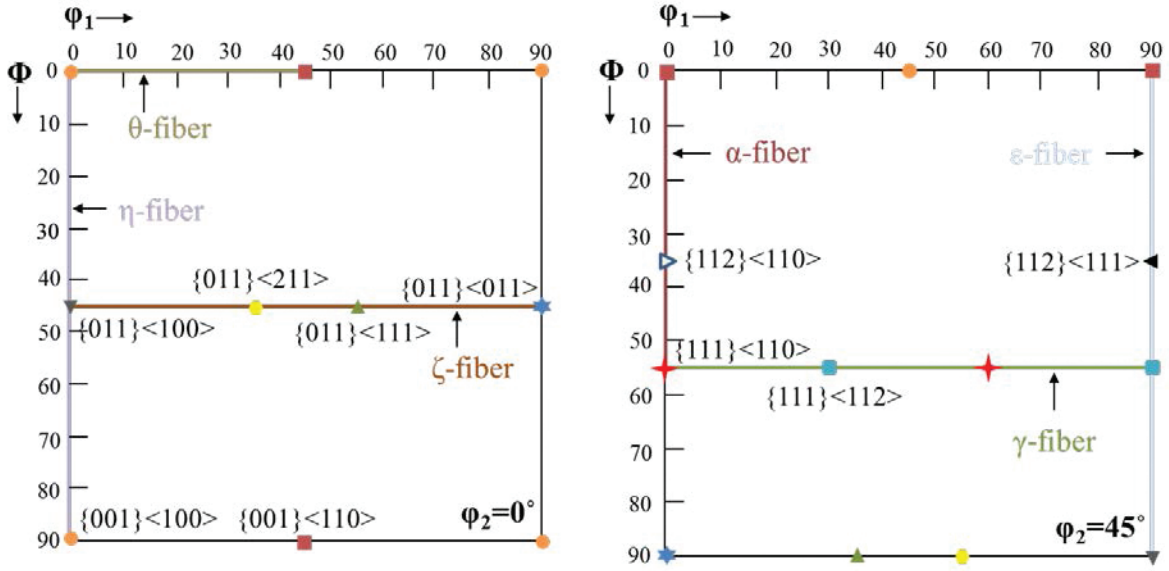

Figure 3.8: Illustration of important BCC components. Copyright Elsevier 2015. Reproduced with permission from Ref. (*71*)

was calculated using the MTEX ODF function, based upon the modified least squares estimator.[72] In describing textures, two different Miller Indices describe the particular texture as it relates to the whole specimen orientation. The specimen direction is related to the crystal through the 3 axes

of Z-direction or normal direction (ND), the X-direction or the rolling direction (RD), and the Y-direction or the Transverse Direction (TD) shown in **Figure 3.7**. The Goss texture is represented in Figure 3.7, with the (hkl) of (110) parallel to the ND and the <uvw> of (001) parallel to the RD. Textures with Miller Indices of both (hkl) and <uvw> are referred to as biaxial textures, whereas uniaxial textures are aligned to just one crystal axis with regards to the specimen. The ideal textures for a BCC material at φ_2 =0°and φ_2 =45°is shown in **Figure 3.8**.[71] The ideal uniaxial textures in BCC materials are the θ-fiber <001> ‖ ND, ζ-fiber <011> ‖ ND, η-fiber <100> ‖ RD, γ-fiber <111> ‖ ND, ε-fiber <011> ‖ TD, and α-fiber <110> ‖ RD.[73] These uniaxial fibers have biaxial components labeled with the different colors in Figure 3.8. The ODF for the different substrates is represented in **Figure 3.9**. Immediately the understanding of the nature of

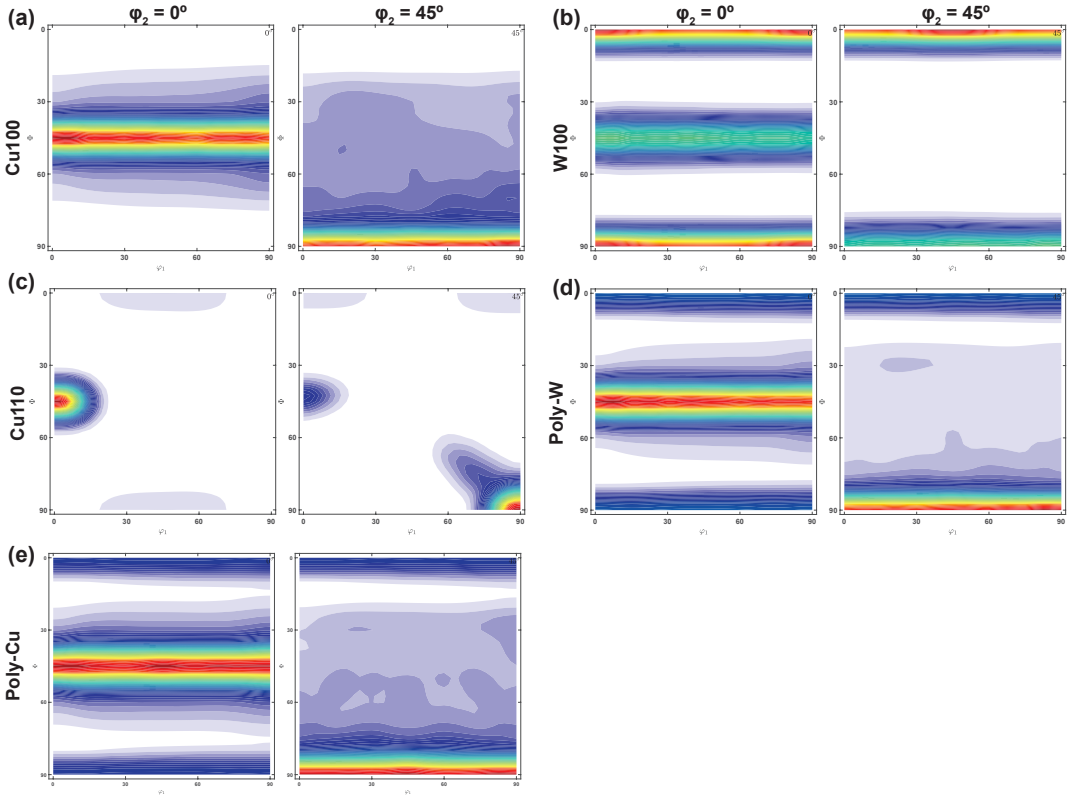

Figure 3.9: ODF of the φ_2 =0°and φ_2 =45°of Cu(100) (**a**), W(100) (**b**), Cu(110) (**c**), Poly-Crystalline W (**d**), and poly-crystalline Cu (**e**) at 20 μm.

the microstructure of the Li is more evident when the ODFs are examined. The Cu(100) (**Figure 3.9a**) shows mainly the ζ-fiber at the Φ =45°and φ_2 =0°. The symmetry of this fiber is visible at

φ_2 =45°and Φ =90°. The W(100) (**Figure 3.9b**) ODF shows a much lighter amount of ζ-fiber and a much higher concentration of the θ-fiber at φ_2=0°and Φ=0°\90°, with the symmetric points at φ_2=45°at Φ=0°. The impact of the substrate shows more clearly with the main fiber aligning with the W(100). The Cu(110) (**Figure 3.9c**) makes this even more apparent with the Goss texture which shows up with (110) <001> at Φ=45°at φ_2=0°with the symmetric point at φ_2=45°φ_1=90°and Φ=90°. Additionally, in the φ_2 =45°there is a small amount of transformed Goss texture with (111) <110> at $\Phi = 45^\circ$ and $\varphi_1 = 0^\circ$. The texture arises due to the aligning with the Cu(110). The Poly-Cu (**Figure 3.9d**) and Poly-W (**Figure 3.9e**) show the ζ-fiber and θ-fibers, with the ζ-fiber being the most prevalent. This shows that the Li, when not impacted by the substrate, prefers the ζ-fiber orientation. From this, a trend appears, and the following hypothesis is proposed. The Li begins

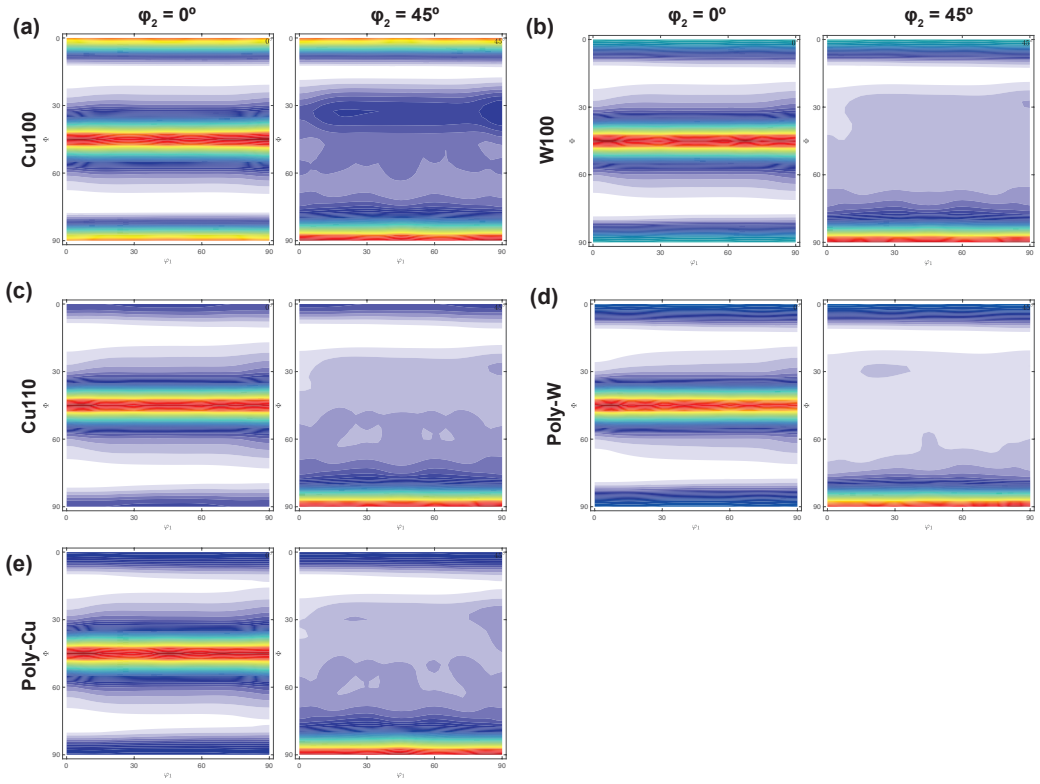

Figure 3.10: ODF of the φ_2 =0°and φ_2 =45°of Cu(100) (**a**), W(100) (**b**), Cu(110) (**c**), Poly-Crystalline W (**d**), and poly-crystalline Cu (**e**) at 200 μm.

nucleating and plating correlating with the principle crystal face of the substrate, as more Li plates the low energy θ-fiber becomes the principle texture of the plated Li. As still more Li plates the

pressure from the cell starts to transition the Li from the θ-fiber to the ζ-fiber texture as this follows the slip plane (110) for the BCC crystal structure.[74] Additionally, the competition between the low surface energy growth grains and the high surface energy growth grains cause an anisotropic growth of specific crystal faces.[10] BR deposition is known to plate in initial fine-grained, equiaxed structures which then transition to grained columnar structure with grain anisotropy and anisotropic crystallographic texture.[10] This is modeled in the BCC 3D projection of **Figure 3.11**, where the blue line is the θ-fiber, and the red lines are the ζ-fiber textures. This is concerning when viewed from the perspective of dendrite prevention due to the higher strength the ζ-fiber has compared to the θ-fiber. This is due to the crystallographic strength of the 110 face vs. the 100 face, due to lithium's high anisotropic factor of 8.52. This high value means that shear and elastic moduli vary significantly with orientation and, therefore, dendrite strength and propensity for formation. It has been calculated that in axial loading, the stiffest orientation is the $<111>$ and the most compliant the $<100>$ supporting the risk of dendrites penetrating the separator at high Li plating due to the fiber transformations. The axial loading aligns with the z-direction, which is the orientation of all fibers observed in the pole figures.

The effect of the substrates, therefore, is mitigated at the larger thicknesses, forming an increasing propensity to have strong dendrites, whereas at small thickness equiaxed structures are more prevalent.

3.3.3 Studies on Separators

The effects of mechanical pressure have shown to be a strong correlative factor in the plating and stripping of Li metal.[75] This is due to the high elastic factors of the Li, allowing for suppression and the changing of the microstructure through the application of mechanical pressure. The effect of the pressure on the fiber texture raises an interesting question: How does the internal pressure distribution (i.e., the separator) change the fiber textures of the plated Li, particularly at the thicker scale? To test this question, the Polyethylene (PE) separator was replaced with glass fiber separator. It has been seen that when PE vs. glass fiber is cycled with Li metal, the glass fiber

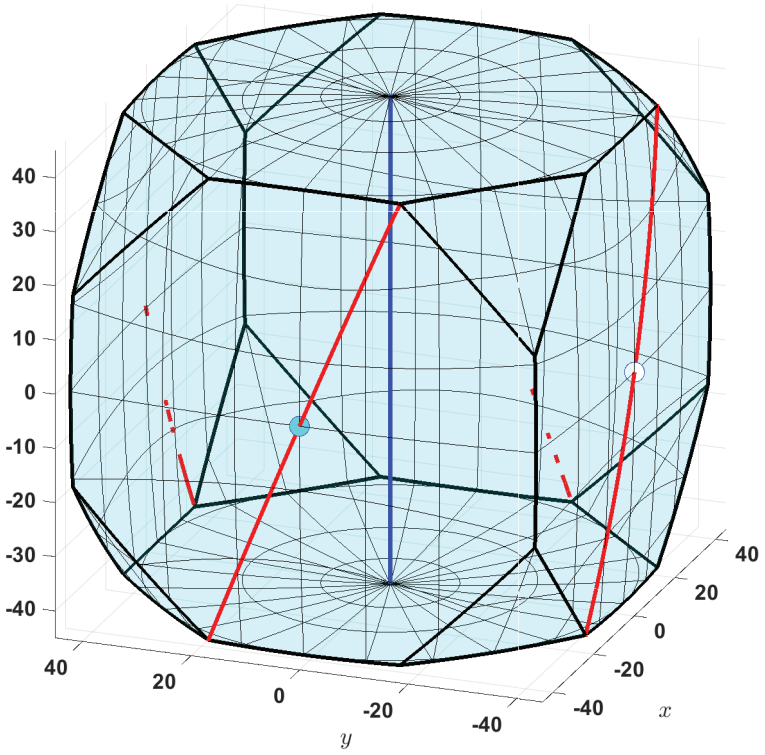

Figure 3.11: 3D crystalline projection of BCC materials with ζ-fiber (blue) and θ-fibers (red).

induces dendrite formation due to the Li growing along the fibers.[68] Additionally, the glass fiber (**Figure 3.12a**) is not uniform in its surface morphology as compared to the Celgard PE (**Figure 3.12b**), creating a more nonhomogeneous pressure profile when against the substrate.

The single crystal and polycrystalline samples were prepared and tested using the same procedure before swapping the Celgard 2500 separator with glass microfiber filter disks. Li was plated to a thickness of 200 μm, and the cells were disassembled, and the pole figure obtained. The pole figures for Li(110) and Li(200) are shown in **Figure 3.13** for (**a**) Cu(100), (**b**) Cu(110), and (**c**) W(100). The pole figures for the GF samples show points in the center indicative of a fiber texture. However, the Cu(100) and Cu(110) points spread laterally in the same direction, with two points developing. This represents an orientation aligning to the rotation of the sample; this separation of points are not seen on the W(100) sample. The samples aligning with the (100) plane of the Li (i.e., Cu(100) and W(100)) have the respective texture distribution being more concentrated at $\approx 90^{\circ}$ rather than the larger distribution of orientations for the Li(110) plane. The

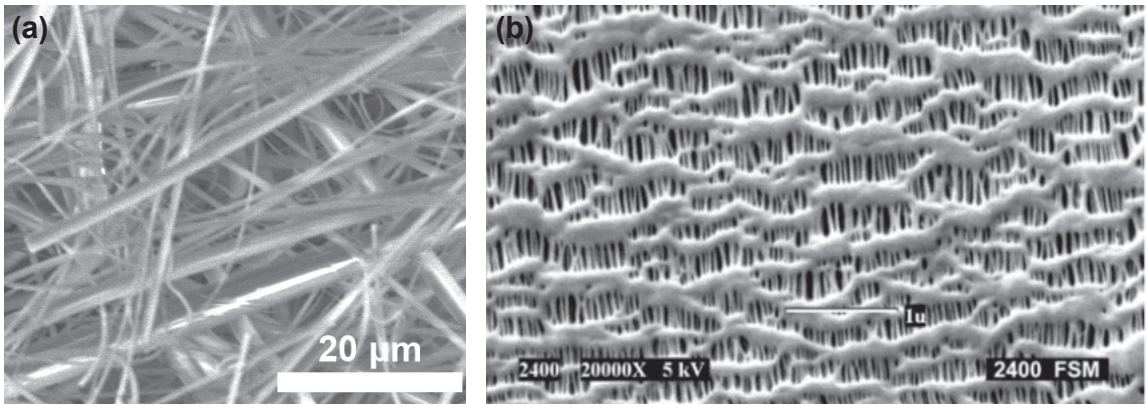

Figure 3.12: SEM of glass fiber (**a**) and Celgard 2335 (**b**) reproduced with permission from (*76*). Copyright 2012 MDPI

further elucidation of the changes the GF has on the texture is seen in the ODF of the single crystals (**Figure 3.14**). The ODF, when compared to the PE, shows a broadening of all fiber textures. The broadening shows an increase in disorientation and that the Li is more amorphous. A new fiber texture is observed along the $\Phi \approx 35^\circ$ axis in $\varphi = 45^\circ$ for both Cu(100) and Cu(110), with faint fiber on the W(100). This fiber texture will hereafter be referred to as the Cu-Fiber with an axis on the Li(112) axis. The appearance of this fiber is attributed mainly to the further deformation and strain of the Li dendrite as it grows longer within the Cu-Fiber. The transition from the θ-fiber to the ζ-fiber texture is less pronounced when GF is used, demonstrating the lack of homogeneous pressure to induce the slip strain effect that leads to this formation. The alignment of the fibers with the substrates holds to be the main texture forming factor in the GF cells.

3.4 Conclusion

The exploration of the single-crystal modified Li microstructure concerning Li amount and separator type has been explored. It was shown that the single crystals affected the principle plane of Li growth and the formation of fiber textures along those principle planes. As Li grows, when enough uniform pressure is had, the transition from the θ-fiber to the ζ-fiber is seen following the slip plane common to BCC materials. It was found that both W(100) and poly-W displayed higher

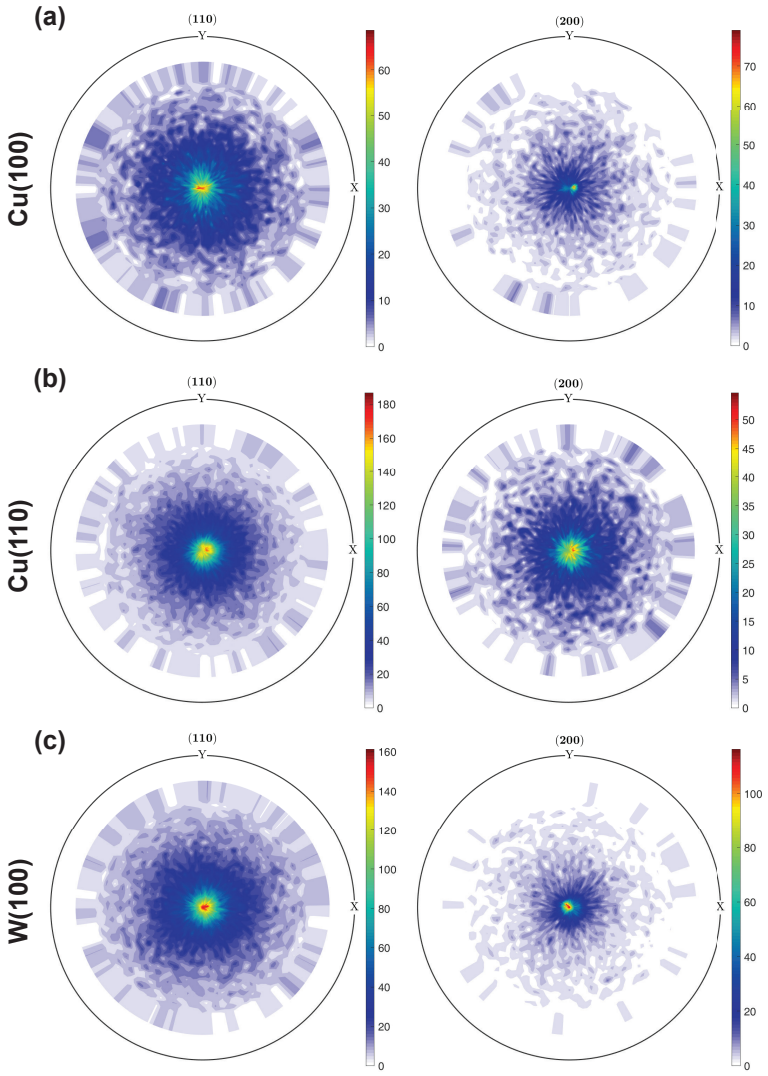

Figure 3.13: Pole figures of single-crystal samples plated to 200 μm for Li(110) peaks and Li(200) with glass fiber separator.

textured materials than the Cu samples with Cu(110) at 20 μ m being the exception. GF further decreases the texture formation increasing the random distribution of textures within the plated Li. Further work can be pursued to understand the effect of continuous cycling and the subsequent SEI formation has on the microstructure of Li metal. The texture and anisotropic properties of Li metal can have a more significant impact on the performance of Li metal batteries than previously thought.

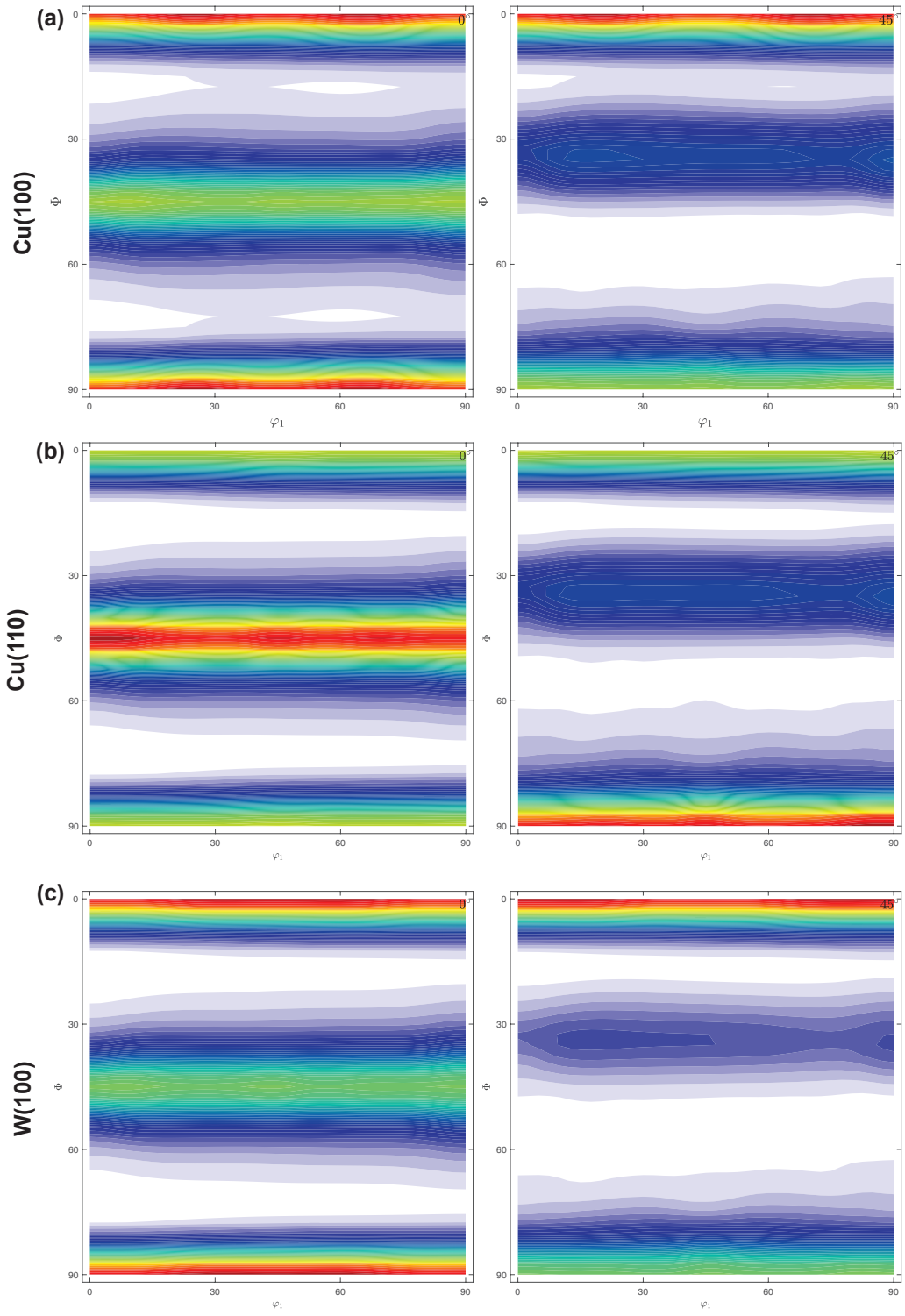

Figure 3.14: ODF of the φ_2 =0°and φ_2 =45°of Cu(100) (**a**), W(100) (**b**), Cu(110) (**c**), Poly-Crystalline W(**d**), and Poly-Crystalline Cu (**e**) at 200 μm with glass fiber texture

4 WO_3 for Modifying the Interface and Omptimize the SEI

4.1 Increased Surface Oxide Content

The other aspect of the surface that affects the nucleation and subsequent plating of Li metal is surface oxides. Therefore, once the surface of the W and Cu were analyzed, it was hypothesized that the surface oxide, mainly WO_3, was the main driving force for the enhanced lithium plating and stripping. Generally, metal oxides reside on all metallic surfaces when exposed to oxygen. Therefore, the surface oxide plays a much more important role than previously thought in regards to Li metal.

4.1.1 Thermal Oxidation of W to Form WO_3

The effects WO_3 has on the SEI was explored through enhancing the surface oxide by thermal treatment to increase the amount of WO_3 on the surface. The surface oxide formation follows two formulas according to Baur et al.[77] Firstly the W reacts with oxygen to form WO_2 shown in equation 3.1

$$W(s) + O_2(g) \rightarrow WO_2(s) \tag{4.1}$$

This WO_2 reacts further with oxygen to form the WO_3.

$$WO_2(s) + \frac{1}{2}O_2(g) \rightarrow WO_3(s) \tag{4.2}$$

This process is exacerbated in the presence of water, where it increases the volatility of tungsten oxides and speeds up the oxidation.

Three separate temperatures were utilized for this starting at 500°C, 600°C, and 700° C. These were heated under ambient conditions in a box furnace for 60 min, except for 700°C which was also heated for 120 min. These were immediately quenched upon finishing to minimize additional oxidation. The W was measured and weighed before then after heating and heated in a crucible boat. **Table 3.1** shows the resulting pictures and weight change of the samples. As ex-

Table 4.1: Post heat treatment analysis of W

Testing Conditions	Tungsten Samples	Δ mg cm^{-2}
500 ˚C 60 min		0.119 mg cm^{-2}
600 ˚C 60 min	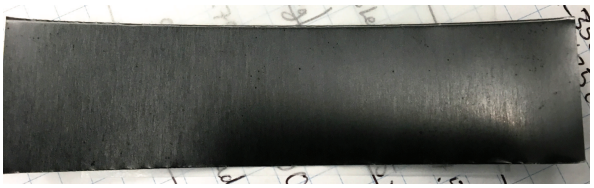	0.689 mg cm^{-2}
700 ˚C 60 min	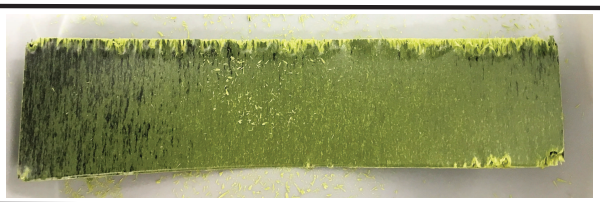	4.582 mg cm^{-2}
700 ˚C 120 min	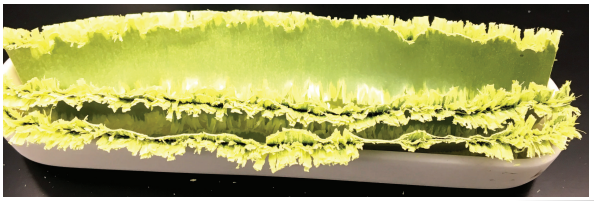	12.2 mg cm^{-2}

pected, the weight change increases as the temperature increases and more time is spent in the heat. The color changes from blue to black, to black with yellow speckles, to almost completely yellow. The color change makes sense as WO_3 is yellow; therefore, as the layer becomes thicker, the appearance of the WO_3 becomes more prominent. Additionally, the edges start to flake as the oxide layer expands into the W whereas, the lower temperatures, 500°C and 600°C, show good adhesion of the oxide layer.

4.1.2 Exploration of Physical and Electrochemical Properties of Heat Treated W

Various characterization methods were performed to understand the WO_x and its impact on the Li metal. XRD (**Figure 4.1**) shows that as the W starts to oxides the WO_3 peaks at 23°and 34°appear. The WO_3 peak at 23° starts to differentiate as the oxide content increase due to the location of 3 separate planes (i.e. WO_3(002), WO_3(020), and WO_3(200)),[78] similar to the green

line of the powder pure WO_3. Furthermore, the peak at 34° is also a composite of WO_3(022), WO_3(202), WO_3(220), and WO_3(202). The W peaks at 59° and 74° start to diminish as well, correlating to W(200) and W(211), respectively. The oxide layer gets thicker and more defined as it grows, and as the temperature increases, both due to increased oxide content and thermal annealing. This agrees with the observations of the color of the samples.

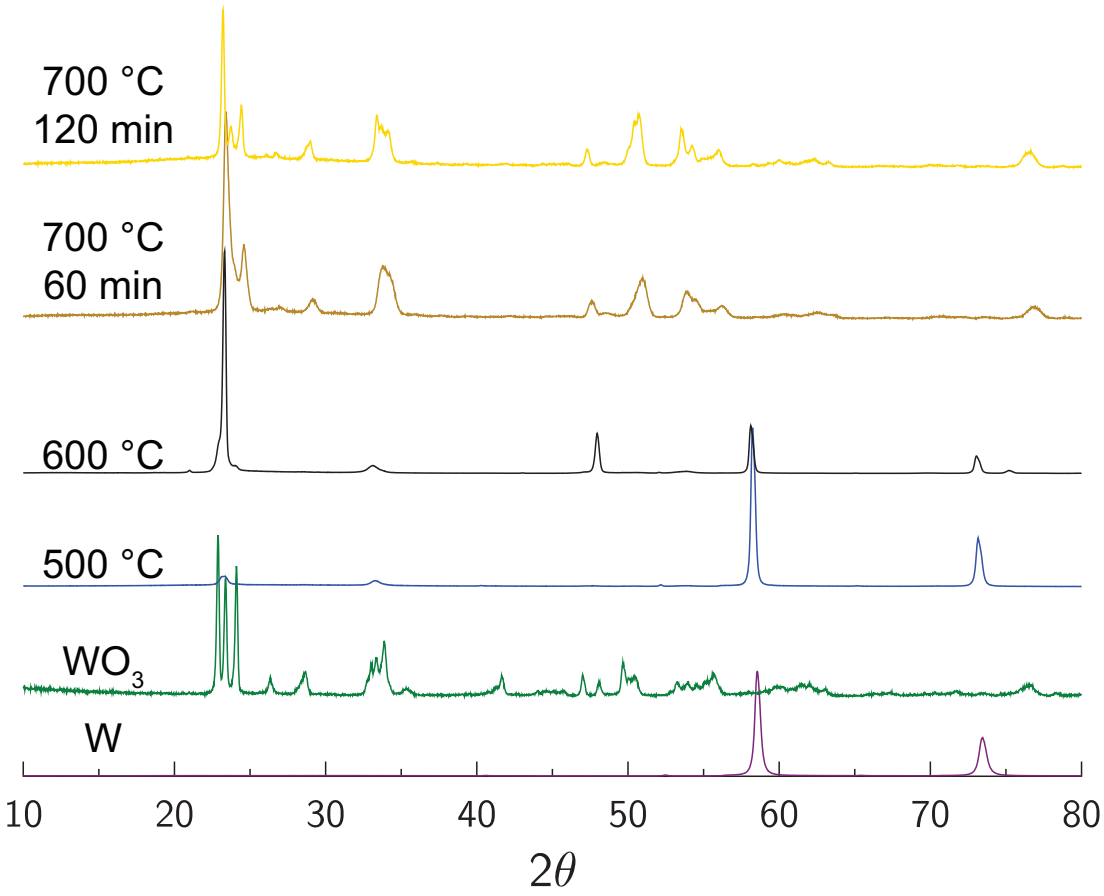

Figure 4.1: XRD of heat-treated W, with bare W the purple line, powdered WO_3 the green line, the blue line the W heated at 500°C, 600°C heat treated W the blue line, 700°C heated for 60 min the dark gold line, the yellow line the 700 °C heated W for 120 min.

The surface morphology of the films were observed under SEM. The SEM of 500°C (**Figure 4.2a**) shows a smooth surface similar to that of the bare W, as the heat increase to 600°C (**Figure 4.2b**) cracks start to appear due to the volume expansion of the WO_3. The unit cell volume for W is 16.191 $Å^3$ and the unit cell volume for WO_3 115.669 $Å^3$ this means that the surface oxide formation causes a volume expansion of 714%. This becomes more prominent at 700°C 65

min (**Figure 4.2c**) and 120 min, as the cracks become greater. Additionally, the surface starts to become speckled with particles of WO_3.

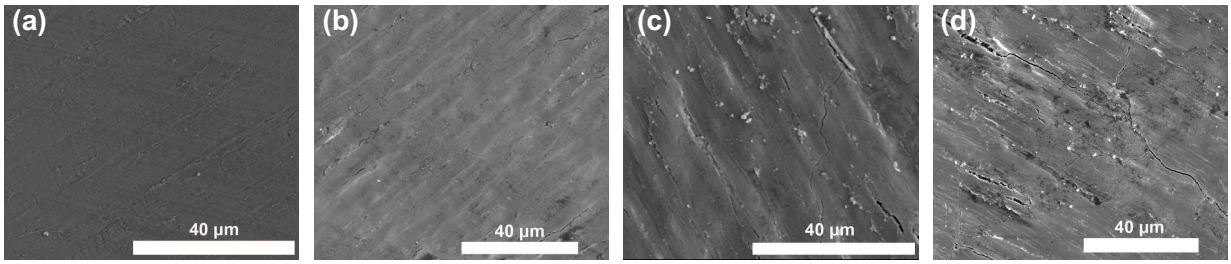

Figure 4.2: SEM of heat treated W heated at 500°C (**a**), 600°C (**b**), 700°C heated for 60 min (**c**), and 700°C for 120 min (**d**).

WO_3 on the W was first discharged to 0V vs. Li^+/Li to understand the conversion reaction and the capacity addition of the WO_3. **Figure 4.4** shows the voltage profile of the different W metals. The profile reveals that the contribution of the additional WO_3 is similar to the weight

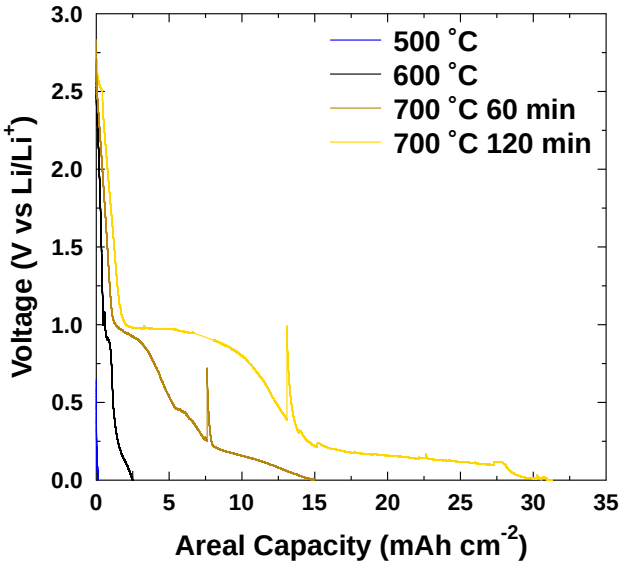

Figure 4.3: Voltage profile of heat treated W discharged to 0V vs. Li^+/Li at 10 μA.

change with capacity contribution of 0.1231 mAh cm^{-2}, 2.5012 mAh cm^{-2}, 14.937 mAh cm^{-2}, and 31.313 mAh cm^{-2}respectively. Additionally, the voltage profile for the intercalation increases as the layer increases. The morphology of the layer, as it undergoes the conversion reaction, will change with the Li's addition within the structure. The morphology changes are minimal for the

500°C (**Figure 4.4a**) and 600°C (**Figure 4.4b**) due to the layer being small, the increased amount of oxide increase the volume change and starts to show the breakdown of the layer. As the layer increases the morphology starts to become rougher and localization of broken surface becomes visible (**Figure 4.4c**). Finally, the surface shows a highly rough morphology at the higher oxide amount due to the higher time during discharge allowing for a more complete conversion at 700 ° C 120 min(**Figure 4.4d**). Therefore, the oxide layers' mechanical stability is greater at lower thicknesses, hinting that lower thicknesses will be idle for SEI modification.

The samples of the 500°, 600°, and 700°C heated for 65 min and 700°C 120 min were tested against Li metal as an anode to determine the capacity retention of the WO_3 and the impact the thicker layers had on the conversion reaction. The metal was cut into 14 μm diameter chips and was cycled against Li metal between 0.3V vs. Li^+/Li to 3.2V vs. Li^+/Li at 0.15 mA cm^{-2}. **Figure 4.5** shows the cycling data for the heat-treated W. An ideal layer's electrochemical profile will show a stable, decreasing capacity and low voltage polarization. The efficiency for the reversible conversion reaction averages to be nominally 99% for both 500°C and 600°C (**Figure 4.5a**). The 500°C shows variation due to fluctuations in the charge capacity. The two 700°C samples both show lower efficiency, spiking to over 100%, particularly the 120 min sample (**Figure 4.5b**). The charge capacity in **Figure 4.5c, d** shows the decreasing capacity retention of the conversion reaction. The thinnest layer 500°C shows a lower decreasing capacity due to the higher kinetics of the thin layer. Also, the thin layer is more stable at the collapsed state and can maintain the electronic conductivity within the layer. The 700°C 60 min shows an increasing capacity then drops off due to failure; the 700°C 120 min decreases in charge capacity until the 5th cycle, which charges until

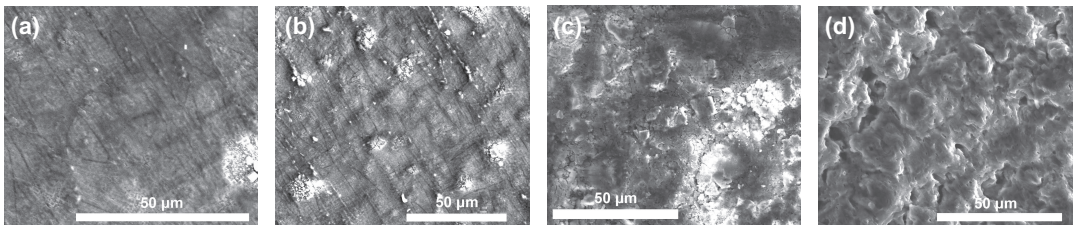

Figure 4.4: SEM of heat treated W discharged to 0V vs. Li^+/Li at 10 μA 500°C (**a**), 600°C (**b**), 700°C heated for 60 min (**c**), and 700°C for 120 min (**d**).

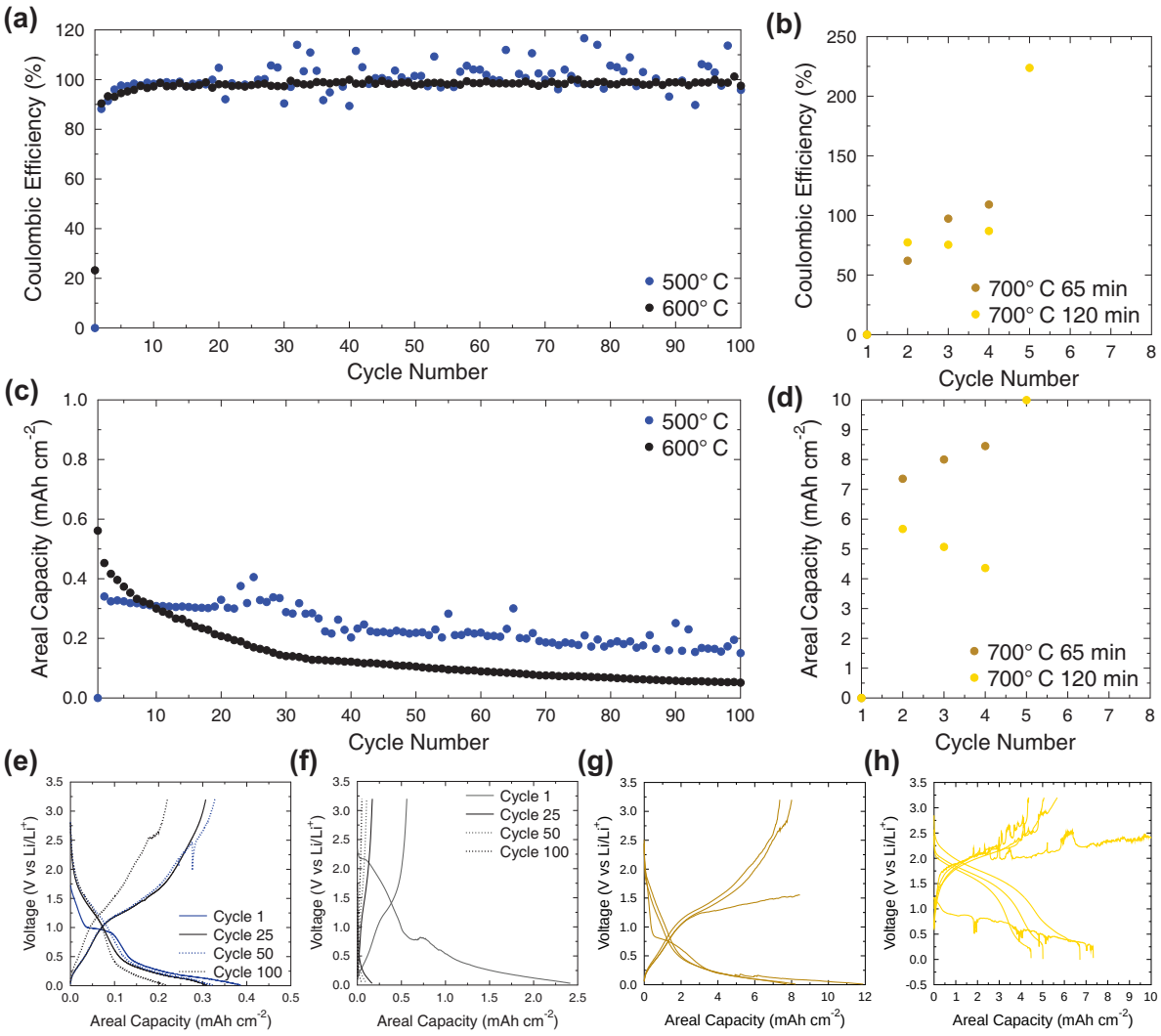

Figure 4.5: Electrochemical Performance of the heat treated W when cycled as an anode from 0.1V- 3.2V vs. Li^+/Li. CE of 500°C and 600°C (**a**); 700°C 65 min and 700°C 120 min (**b**). Areal Capacity of 500°C and 600°C (**c**); 700°C heated for 65 min and 700°C heated for 120 min (**d**). Voltage Profiles of 500°C (**e**), 600°C (**f**), 700°C heated for 65 min (**g**), and 700°C for 120 min (**h**).

failure, never reaching the endpoint. The fluctuations show that increased thickness increases the volume change of the layer, decreasing the electronic conductivity to the point that it cannot charge out. The voltage profiles show Li's intercalation during the first discharge with the plateau at 1V vs. Li^+/Li on the first cycle (**Figure 4.5e-h**). The intercalation plateau disappears after the first cycle due to the nature of the conversion reaction. The formed WO_3 after undergoing conversion reaction is more amorphous, limiting the intercalation due to the lack of interstitial sites within the crystal structure. The instability of the large oxide layer is most prevalent in **Figure 4.5h** due to

the large fluctuations during the charge and discharge cycles. The 600°C sample shows the best behavior and a performance that would indicate it is a strong candidate.

The heat-treated W anodes were then tested against the plating and stripping of Li metal shown in **Figure 4.6**. The CE (**Figure 4.6a**), after 100 cycles, shows the W heated in the box furnace at 600°C for 60 minutes has the highest most stable performance. The 700°C 60 minutes and 500°C show semi-stable cycling up to 40 and 20 cycles, respectively, before starting to lose stability. The 700°C 120 minute W shows efficiency at and above 100% before failing at 50 cycles. The voltage profile for the W heated at 500°C shows the conversion reaction in the first cycle and disappearing by the 25th cycle. The W heated at 600°C in **Figure 4.6c** shows a more significant capacity contributed by the WO_3 conversion reaction than the 500°C. At the 25th cycle, the conversion reaction has almost completely disappeared, but for a little contribution upon charging ceasing by the 50th cycle. As the layer increases, the conversion reaction's participation at early cycles is much higher, as seen in **Figure 4.6d** of W heated at 700°C for 60 minutes. The conversion reaction plays a significant role in the failure mechanism. The thick WO_3 destabilizes as the cell cycles leading to the infinite charging seen in cycle 100. The layer's thickness effects are further shown in the W heated at 700°C for 120 minutes (**Figure 4.6e**). The coating is so thick that no Li is plated even after 50 cycles; the layer destabilizes, and the cell fails due to not charging to the cutoff voltage of 1.5V vs. Li^+/Li. W heated at 600°C shows the most promise due to the stability of the efficiency and the conversion reaction ending quickly. The theoretical benefit of the oxide layer is believed to be the products of the reaction mainly the W and the SEI components generated. The WO_3 needs to be thick enough to produce the optimal amount of W and SEI components, but not thick enough that the Li plates onto an unstable layer of WO_3 that can peel off, thereby losing electronic contact.

4.1.3 Optimized Oxidation of W

To explore this interaction, an optimized and reproducible layer of WO_3 needs to be formed on the surface of W. Two different heat treatments were performed at 600°C to find the best method

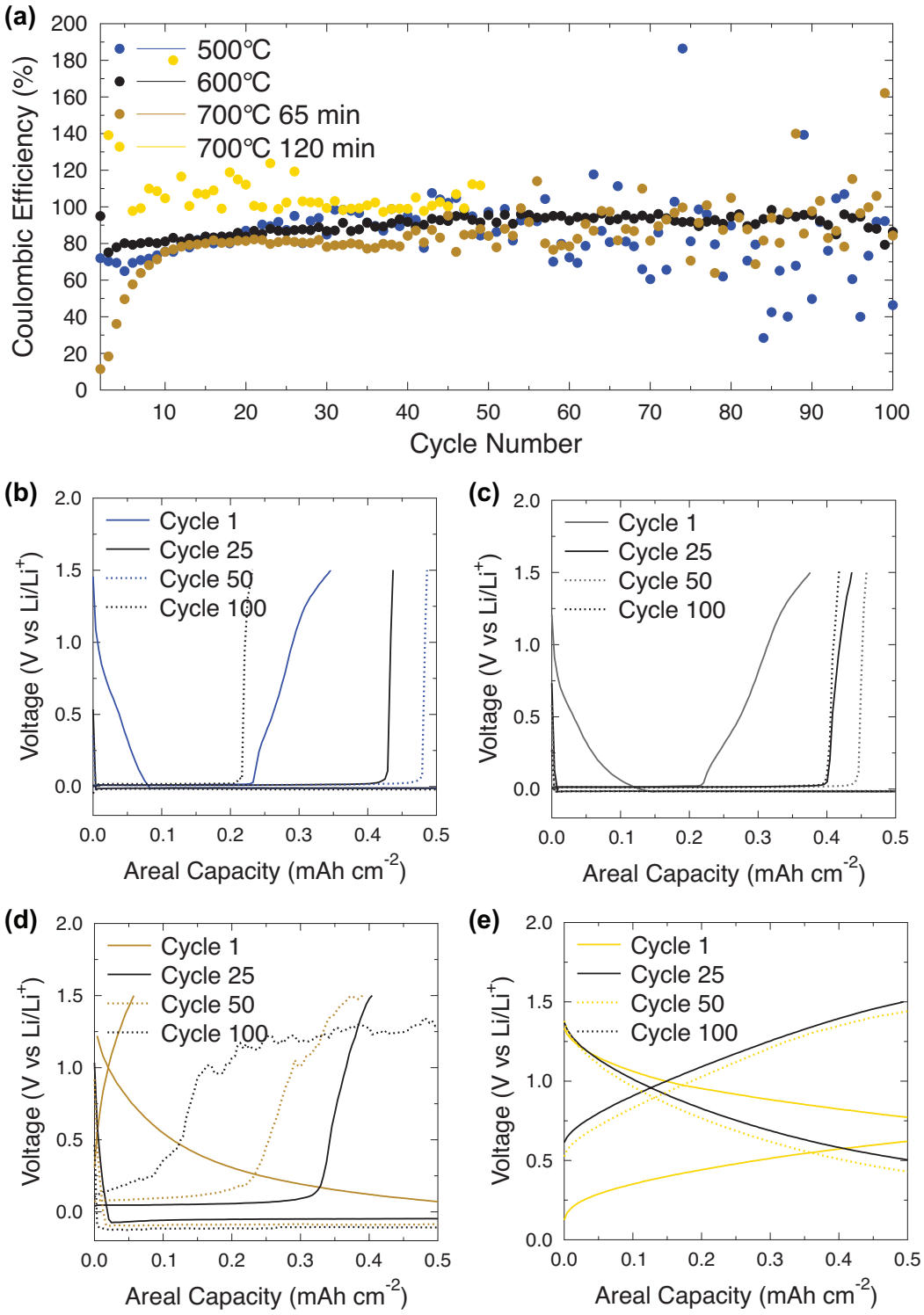

Figure 4.6: Heat treated W plating and stripping of Li metal CE (**a**); voltage profiles of 500°C (**b**), 600°C (**c**), 700°C heated for 60 min (**d**), and 700°C for 120 min (**e**).

for heat formation of the oxide: box furnace and tube furnace. The samples were heated at 600°C, as mentioned for 30 minutes, followed by immediate quenching in ambient air to minimize further reactions. The samples were varied with different ramp times and different atmospheres. Samples in the box furnace were heated under an ambient atmosphere. The samples in heated in the tube furnace were heated under pure oxygen, by first running oxygen through the tube for 30 minutes before heating, to purify the atmosphere within the tube. The samples upon completion were weighed then tested against Li metal and the plating and stripping of Li metal. They were first tested by discharging to 0V vs. Li^+/Li at 0.25 mAh cm $^{-2}$ to determine the initial contribution of the conversion reaction of the oxide. The cells were then cycled using the previous procedure for the plating and stripping of Li metal (discharged at 0.25 mA/cm^2 to 0.5 mAh/cm^2 of Li and charged at 0.25 mA/cm^2 to cutoff voltage of 1.5V vs. Li^+/Li). The average weight change, the capacity contribution of WO_3, CE, and mean average distribution (MAD) of the CE are shown for the various samples. The MAD of the CE is a metric that can show the fluctuation of efficiency. The higher fluctuations cause higher MADs and demonstrate the decreased stability the substrate is against Li. MAD is measured in this case by **Equation 3.3**:

$$MAD = \frac{1}{n}\sum_{n=1}^{n} |e_i + m(X)| \tag{4.3}$$

where n, in this case, is the number of cycles (100), e_i is the efficiency of any given cycle, and m(X) is the mean efficiency of the particular cell. Therefore, MAD allows for a robust understanding of the dispersion of efficiencies during the life cycle of a cell. **Table 3.2** shows the resulting averages for the box furnace samples. The samples ramped at 30 minutes showed an increase in the amount of weight change than the ones ramped at 15 minutes and 5 minutes. The longer time for the reaction to take place increases the weight change. The ones ramped at 15 min. and 5 min. show a similar average change in weight after heating of $\approx$ 0.45 mg cm^{-2}, however, the 5 min. ramp has a much larger variation than the 15 min. ramp time. Interestingly while the weight change is similar, the contribution of the layer is much greater than that of the 5 min. ramp. When it

Table 4.2: Average Weight Change, Capacity, Efficiency, and MAD of 3 cells at different ramp times heated for 30 min under an ambient atmosphere in the Box Furnace.

Sample	Avg. Weight Change (Δmg cm^{-2})	Avg. WO_3 Capacity (mAh cm^{-2})	Avg. Efficiency (%)	Avg. MAD (%)
30min Ramp	1.032 ± 0.6966	1.759 ± 0.7988	88.49 ± 2.470	8.666 ± 1.669
15min Ramp	0.4524 ± 0.2539	1.104 ± 0.4076	100.9 ± 14.82	10.84 ± 0.0981
5min Ramp	0.4297 ± 0.5469	0.4004 ± 0.1263	87.86 ± 0.7799	6.082 ± 1.917

comes to the plating and stripping of Li metal, the 15 min. ramp has the highest Avg. efficiency of the samples; however the various cells tested show a very high distribution of Avg. efficiency. Additionally, the Avg. MADs of the cells tested are the highest at $\approx$10.84$\pm$0.0981% showing that the substrate is more unstable with Li metal, giving the high variation in the efficiency. The most stable is the 5 min. ramp giving an Avg. efficiency of 87.86$\pm$0.7799 %, while the efficiency is lower than others, the MAD is 6.082$\pm$1.917% showing the efficiency is the most stable. The data doesn't seem to correlate the amount of WO_3 with performance, as shown in the table when averages were examined. This is further shown when the best cells from each sample set (**Table 3.3**) were examined. The better performing cells have a linear change in both weight change and

Table 4.3: Weight Change, Capacity, Efficiency, and MAD of the best cell at different ramp times heated for 30 min under an ambient atmosphere in the Box Furnace.

Sample	Weight Change (Δmg cm^{-2})	WO_3 Capacity (mAh cm^{-2})	Avg. Efficiency	MAD
30min Ramp	0.6836	1.360	89.72	7.831
15min Ramp	0.3255	0.9003	108.3	10.79
5min Ramp	0.1563	0.3372	88.25	7.051

capacity contribution. The 15 min ramp still shows an unstable interface with an average efficiency of 108.3% and MAD of 10.79%. The 30 min ramp and 5 min ramp show results very similar efficiencies and MADs. This seems to show that either the interface needs to have long time to stabilize the WO_3 formed on the surface, or ramp time has to be so low to immediately start the oxidation without the unstable intermediates.

When samples prepared under controlled oxygen atmosphere were examined, the first thing

that stands out, is the weight change was significantly reduced and the difference between difference ramp times is diminished. Additionally, on both 30 min ramp and 5 min ramp the difference between the different cells is much less, under ambient atmosphere in the box furnace the difference between cells was 0.6966 mg cm^{-2} and 0.5469 mg cm^{-2} as compared to the controlled oxygen atmosphere tube furnace with a low variance of 0.08464 mg cm^{-2} and 0.03906 mg cm^{-2} respectively. The Avg. WO_3 capacity contribution shows the large difference stemming from the 30 min. ramp time, the 15 min. ramp and 5 min. ramp both share an Avg. contribution of 0.5213 mAh cm^{-2} and 0.5193 mAh cm^{-2}.The performance of the samples heated under the oxygen atmosphere show an average efficiency greater than that of the ambient box furnace samples with 30 min ramp averaging $\approx$94.99$\pm$14.91%, 15 min ramp averaging $\approx$92.05$\pm$4.828%, $\approx$89.86$\pm$5.29. It is hypothesized that the reason for the increased efficiency is the purity of the substrates formed. The MADs for the pure atmosphere samples holds to similar percentages as those of the box furnace samples indicating that while the efficiency increased the stability is similar. Interestingly not only the averages, but the best cells (**Table 3.5**) from the samples for the oxygen atmosphere show a 15 min ramp time has the best performance in stability with the 30 min ramp showing the best efficiency. It is hypothesized that this is occurring due to the lack of secondary compounds forming, therefore it is only thickness of the layer of oxide that contributes to the SEI and not the secondary compounds which can be formed under the ambient atmosphere.

These results bring two concerns to the forefront of this testing method. While the oxide

Table 4.4: Average Weight Change, Capacity, Efficiency, and MAD of 3 cells at different ramp times heated for 30 min under oxygen atmosphere in the Tube Furnace after purging for 30 min with O_2.

Sample	Avg. Weight Change (Δmg cm^{-2})	Avg. WO_3 Capacity (mAh cm^{-2})	Avg. Efficiency (%)	Avg. MAD (%)
30min Ramp	0.3999 $\pm$0.08464	1.121 $\pm$0.3763	94.99 $\pm$14.91	11.37 $\pm$1.067
15min Ramp	0.4524 $\pm$0.2148	0.5213 $\pm$0.7721	92.05 $\pm$4.828	7.981 $\pm$3.170
5min Ramp	0.2864 $\pm$0.03906	0.5193 $\pm$0.5592	89.86 $\pm$5.294	7.857 $\pm$1.9178

Table 4.5: Weight Change, Capacity, Efficiency, and MAD of the best cell at different ramp times heated for 30 min under oxygen atmosphere in the Tube Furnace after purging for 30 min with O_2.

Sample	Weight Change (Δmg cm^{-2})	WO_3 Capacity (mAh cm^{-2})	Avg. Efficiency (%)	MAD (%)
30min Ramp	0.3646	1.3724	102.2	10.57
15min Ramp	0.3060	0.1712	91.27	6.655
5min Ramp	0.2669	0.1315	82.93	7.320

layers are formed the consistency of the weight change, the capacity contribution, and purity is worrisome. The oxide layer's exact effects cannot be correctly understood if the produced layer is inconsistent between samples. Additionally, while the formation of the oxide layer on the W shows an increase in performance, the cost of production and W metal, in general, is a concern for practical applications. The W is two times the density of Cu; this leads to a marked increase in the weight of the battery, decreasing the Gravimetric energy density, which uses the total weight of the battery, including inactive components. Furthermore, the benefits of the oxide layer cannot be wholly separated from the W substrate. This lead to the search for applying a thin, consistent WO_3 onto Cu. The Cu is the standard current collector allowing for a complete comparison of the specific activity of the tungsten oxide without the impact of the W substrate.

4.2 WO_3 for Modifying the SEI

As shown, there is a correlation to WO_3 content and lithium metal plating and stripping. WO_3 is interesting due to its intermediate stages, as mentioned in Chapter 1, and its ability to intercalate Li to form the tungsten bronzes. Additionally, the various tungsten oxides that are formed during conversion are catalytically active. Therefore, it is hypothesized from the previous results that WO_3 has three main roles in the impact of the interracial reactions leading to the formation of the SEI. Firstly, WO_3 alters the nucleation/growth of Li metal plating and stripping. Secondly, the tungsten oxide helps generate inorganic constituents within the SEI. Finally, a generation of W metal within the SEI network helps to decrease the formation of "dead" Li which otherwise becomes isolated and irreversible.[79] To further flesh this hypothesis out in a systematic manner and

with relation to Cu being the underlying substrate, a thin layer of W was sputter deposited onto the surface of Cu under different oxygen atmospheres (Experiential in appendices) in collaboration Dr. Xingchen Xiao from GM. The different atmospheres alter the tungsten oxides formed and the subsequent colors of the coated copper.

4.2.1 Impacts of WO_3 on Nucleation during Plating and Stripping of Li

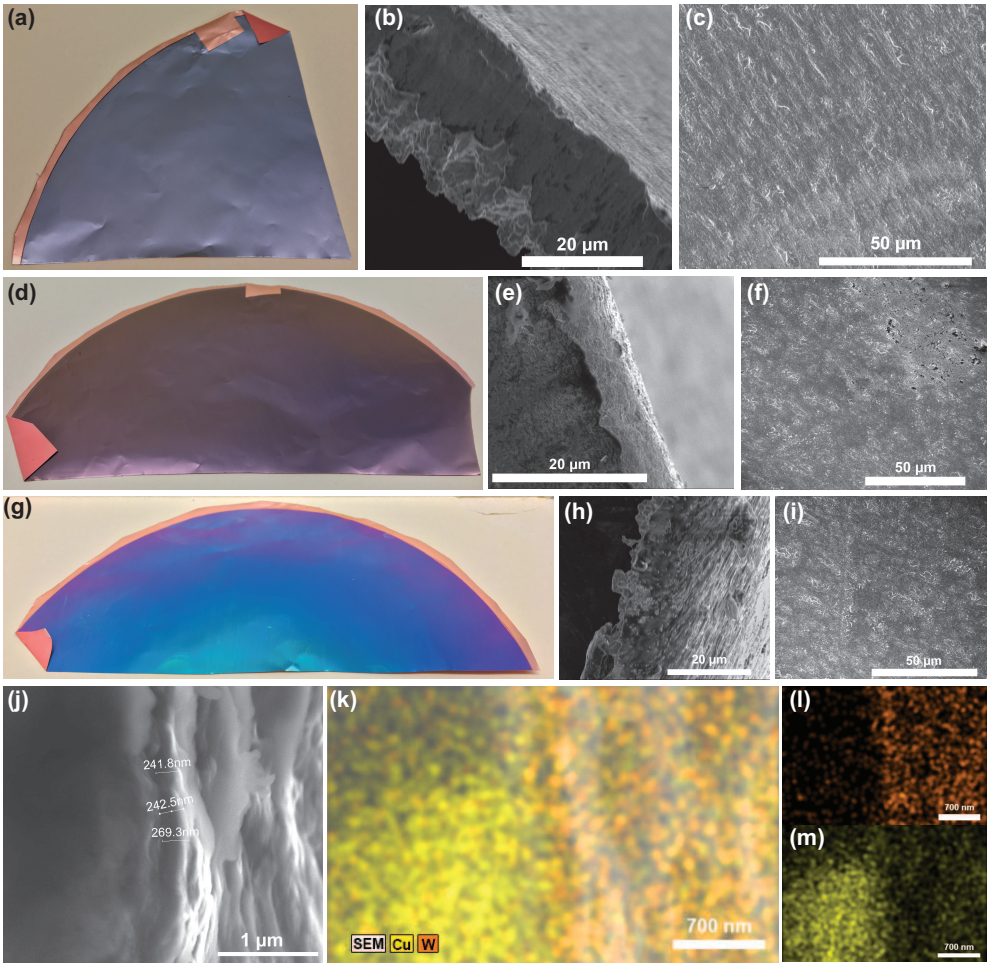

Figure 4.7: Visual and SEM images of Coating 1 (**a-c**), Coating 2 (**a-c**), Coating 3 (**a-c**), with cross-section analysis (**j**), and EDX of Coating 3 (**k-m**). Reproduced with permission from Ref. (*79*). Copyright 2019 American Chemical Society

The thin layers of WO_3 can be seen in **Figure 4.7** The first sample (**Figure 4.7a**) shows a grey color due to the lowest oxygen content, this sample will be referred to as Coating 1. The SEM of the cross-section (**Figure 4.7b**) and surface (**Figure 4.7c**) shows a smooth surface with

the coating having some cracks and ridges. The second coating (Coating 2), shows a more brown color (**Figure 4.7d**), this coating had a higher oxygen content than Coating 1. The cross-section SEM (**Figure 4.7e**) shows a rougher surface than that of Coating 1. Additionally, the surface SEM (**Figure 4.7f**) reveals dark patches on the surface with cracks and pitting. Coating 3(the sample with the highest oxygen content) shows a blue color in **Figure 4.7g**. The color difference between the coatings varies based on edge oxygen vacancies and thin-film interference. Higher oxygen content changes the color of the tungsten oxide with thin-film interference, additionally modifying this color. The cross-sectional SEM, in **Figure 4.7h**, shows a surface similar to that of Coating 2 some roughness and pitting. However, the surface SEM (**Figure 4.7i**) differs from Coating 2 in the absence of the black spots seen on its surface. Upon closer examination of the cross-section (**Figure 4.7j**) and the conjunctive use of Energy-dispersive X-ray Spectroscopy (EDX) shown in **Figures 4.7 k-m** the thickness of the oxide layers are ≈251.25 nm. The XRD of the

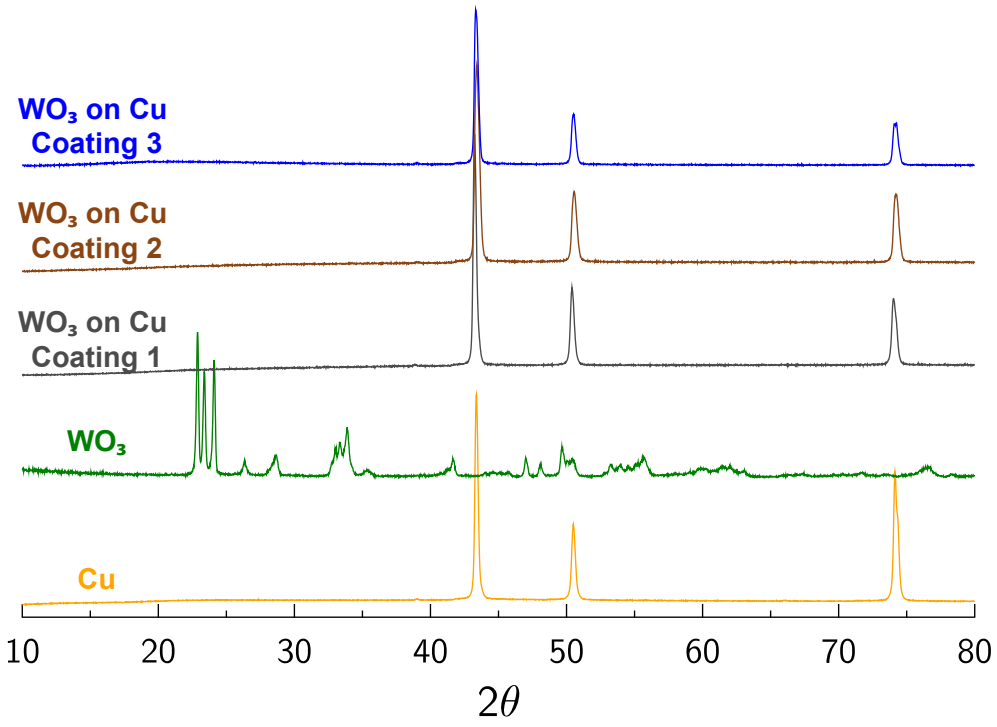

Figure 4.8: XRD analysis of the three coatings on Cu with WO_3 and Cu blank substrates.

coated materials (**Figure 4.8**) shows just the Cu peaks with no visible WO_3 peaks. These copper

peaks correspond to the phases Cu(111) at 44°, Cu(200) at 51 °, and Cu(220) at 74°. The lack of WO_3 peaks is indicative of the layer being amorphous. Corresponding to the fact that the samples were prepared at room temperature with no annealing of the layers after formation. The samples' surface compounds were examined using XPS to determine the exact oxides present. The XPS (**Figure 4.9**) reveals the different oxides on the different coatings. Coating 1 shows the presence of 3 different W oxides WO_2, $W_{18}O_{49}$, and WO_3 (**Figure 4.9a**) at 32.1 eV, 34.1 eV, and 36.2 eV respectively. Coating 2 (**Figure 4.9b**) shows just the two oxides $W_{18}O_{49}$ and WO_3 at 34.1 eV and 36.2 eV respectively. Coating 3 (**Figure 4.9c**)shows just the WO_3 peak in the W4f region at 36.2 eV binding energy. The XPS shows the differing oxygen content used during the sputtering, affected the surface oxides, with the higher oxygen content forming the more pure oxide.

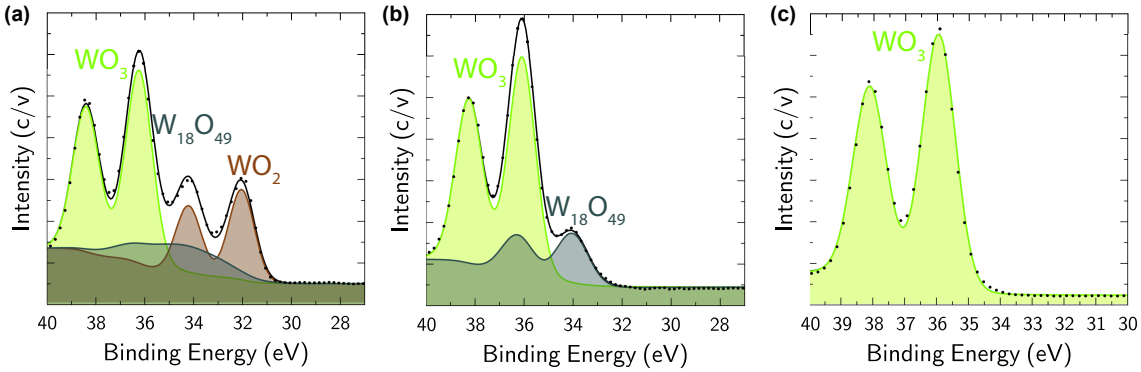

Figure 4.9: XPS of the W4F region of Coating 1 (**a**), Coating 2 (**b**), and Coating 3 (**c**).

To understand the impact the substrates had on the nucleation of Li metal 0.0625 mAh cm^{-2} of Li was coated on the different coated samples. Using this low of capacity allows for the morphology of the Li that is plated on the surface and not that plated onto other Li metal to be observed. **Figure 4.10** shows the different SEM of this nucleation stage of the different coated coppers. Coating 1 (**Figure 4.10a, b**) shows a morphology with large wide areas plated with Li metal. The morphology is large, with fibers at the edges. Interestingly for Coating 2, different regions appear shown in **Figure 4.10c**. Upon closer inspection, these two regions have differing Li morphologies with the top "dark" region showing larger rough Li morphology (**Figure 4.10d**). The other "light" region shows a small dispersion of Li particles much smaller than that of the

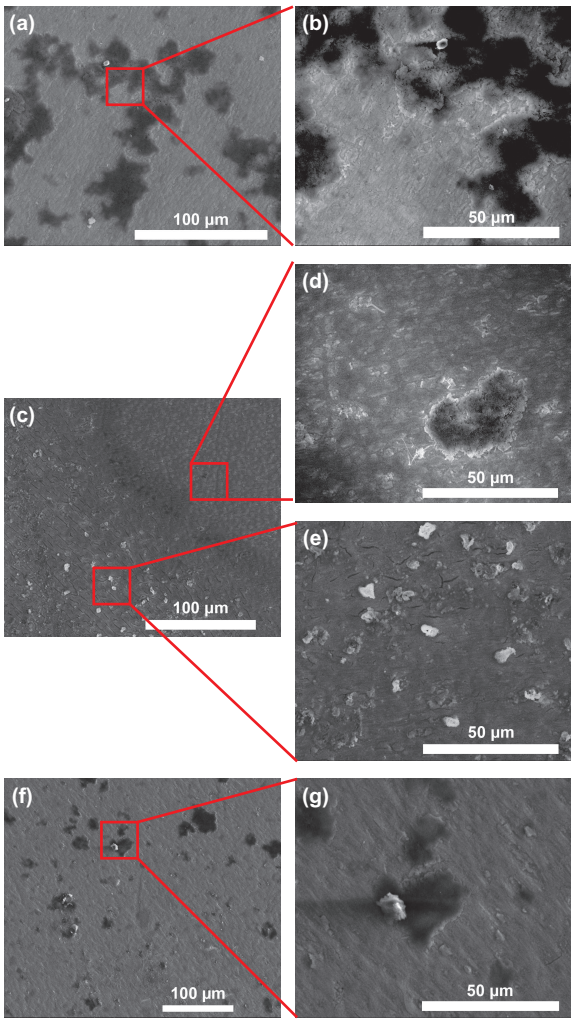

Figure 4.10: SEM of Coating 1 (**a, b**), Coating 2 (**c-e**), and Coating 3 (**f, g**). Reproduced with permission from Ref. (*79*). Copyright 2019 American Chemical Society

"dark" region. Coating 3 (**Figure 4.10f, g**) shows a morphology closer to that of Coating 1, with the covering of the Li being much less at this stage. The Li covering discrepancy is caused by the oxygen discrepancy between the two layers. More Li is needed for the conversion reactions on Coating 3 than Coating 1 based on stoichiometry.

EDX was used on Coating 2 to determine further the causes, which lead to the differing morphologies by analyzing the atomic difference of the three regions present, the "dark" region, the center transitional area, and the "light" region. Three point scans were taken at the previously mentioned areas shown in **Figure 4.11a** on the Li surfaces baring the transitional region, which didn't have any Li visible at this scale. **Figure 4.11b** provides a bar graph of the weight percent

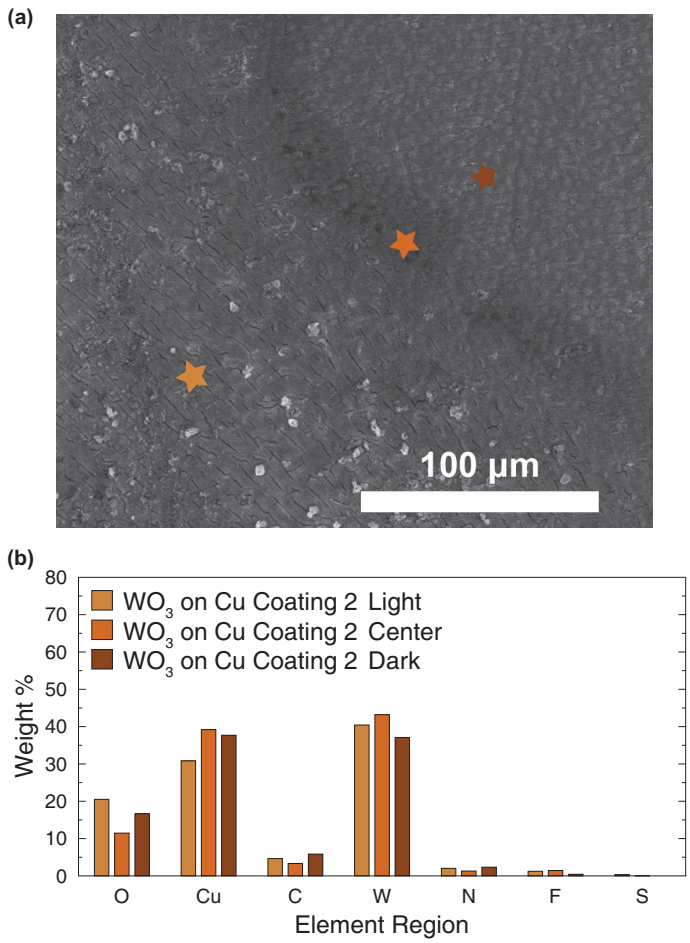

Figure 4.11: SEM (**a**) and EDX analysis (**b**) of the two-part area of Coating 2.

of each element in the various regions. Interestingly the regions with the highest amount of metals (Cu and W) have the lowest oxygen present, indicating these areas are areas with a low initial oxide covering. The "light" region has the most F and O, which would arise due to the great amounts of Li. However, the F may contribute to decreasing the nucleation overpotential allowing for the greater Li nucleation points, thereby decreasing the size. The "dark" region has the least amount of F, N, and O. This is attributed to the decreased breakdown of the electrolyte leading to a weaker SEI. Upon further polarization, to 1 mAh cm^{-2}, the differing morphologies are more visible. Coating 1 shows a more moss-like structure (**Figure 4.12a, b**). The two regions of Coating 2 completely disappear, and a mossy than morphology is seen. The Li particles are larger than that of Coating 1. Coating 3 shows the smoothest morphologies out of the three different coatings, less

of a mossy structure, and more of flat "sheets" overlapping. The Li plating morphology shows that pure WO_3 has a marked impact on the smoothness of the plated Li.

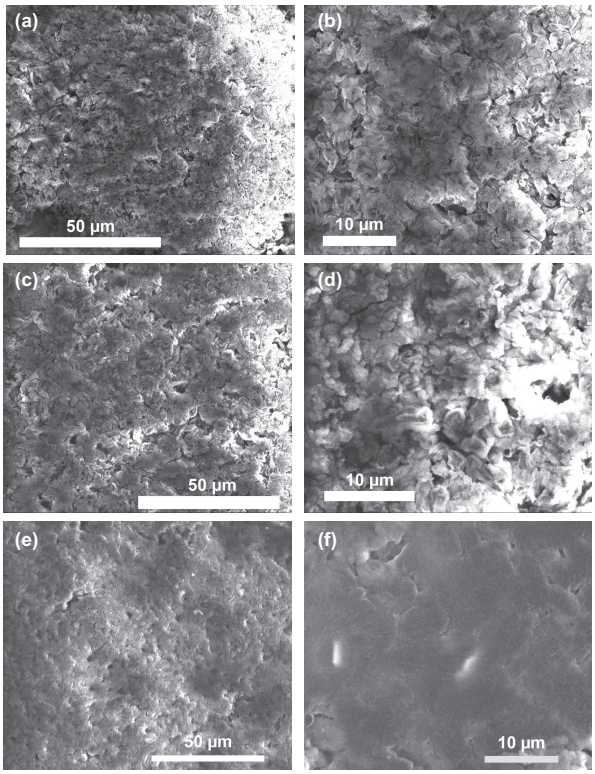

Figure 4.12: SEM of Lithium plated to 1 mAh cm^{-2} on Coating 1 (**a, b**), Coating 2 (**c, d**), and Coating 3 (**e, f**).

Further comparison from an electrochemical standpoint is shown in **Figure 4.13**. The CE (**Figure 4.13a**) shows that Coating 3 has the highest CE and higher stability than that of the other two coatings. The voltage polarization of Coating 1 (**Figure 4.13b**) shows large fluctuations at the beginning cycles with many fluctuations in the overall overpotential showing a layer that is unstable and changing from cycle to cycle. Additionally, the overpotential is the highest for this coating than the other two coatings, demonstrating a negative contribution to the internal resistance decreasing performance. Coating 2 (**Figure 4.13c**) voltage polarization shows less large fluctuations, but small changes are still seen within the cell going from lower relative overpotentials to higher and back to lower. The coating is more stable than Coating 1, but the changes are not negligible. **Figure 4.13d** shows the voltage polarization for Coating 3. This coating shows the most stable overpotential of

the three coatings. Additionally, the only fluctuation of the overpotential is that of a slow increase indicative of increased resistance due to SEI formation. The voltage profiles give greater detail

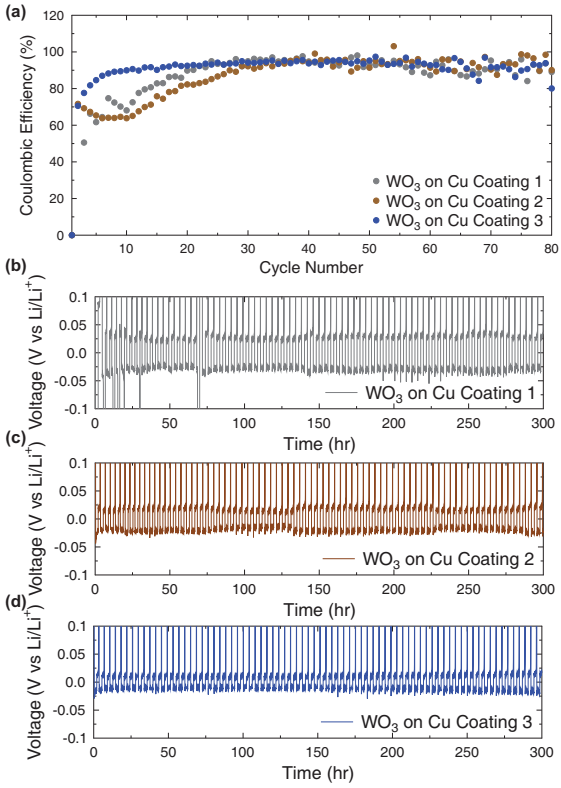

Figure 4.13: Electrochemical testing of the coatings showing the CE (**a**) for the coatings and the voltage polarization of Coating 1 (**b**), Coating 2 (**c**), and Coating 3 (**d**). Reproduced with permission from Ref. (*79*). Copyright 2019 American Chemical Society

on the changes Li plating and stripping takes place on the coated surfaces shown in **Figure 4.14**. **Figure 4.14a, b** show the large polarization seen at the beginning cycles. The least amount of capacity is contributed by this coating. Two separate plateaus are seen on the charging stage of the first cycle, because the first plateau corresponds to the formation of the Li tungsten bronze, before the conversion into W and Li_2O. The first plateau disappeared by the 25th cycle. The polarization stabilizes and stays very similar through the rest of the cycles. Coating 2 (**Figure 4.14 c, d**) shows a much greater capacity contribution than that of Coating 1 ($\approx$0.75 mAh cm^{-2}). This capacity contribution is seen on the charge cycle as well. By the 25th cycle, however, this capacity contribution is reduced. It disappeared completely by the 50th cycle, corresponding to the oxide layer composition as more O is in the oxide layer, the more Li is needed to convert it. Coating 3

(**Figure 4.14 e, f**) shows the most conversion contribution, which corresponds to the higher oxide, leading to more Li needed. This coating is the most stable with the least fluctuation of voltage polarization and efficiency. The nucleation overpotential of Cu in Figure 2.2 from Chapter 2 is -53.6 mV vs. Li^+/Li, while Coating 1, 2, 3 (**Figure 4.14 b, d, f**) is -190.3 mV vs. Li^+/Li, -48.3mV vs. Li^+/Li, and -29.1 mV vs. Li^+/Li respectively. The main reason for this difference is because although Li_2O is insulating, W is electronically conductive. Li_2O also has a lower bandgap than the other components within the SEI formed on the Cu, improving the net conductivity,[80] and Li_2O has been shown to stabilize Li metal.[81] The presence of Li_2O reinforces SEI integrity allowing for fewer cracks in the SEI and mitigates further electrolyte consumption.[82] Therefore, SEI-derived from continuous electrolyte decomposition is reduced, leading to the reduced total cell impedance and the observed overpotential. These coatings show that WO_3 as a coating material increases the stability of the interface and stabilizes the plating and stripping of Li metal when compared to the performance of Cu shown in Figure 2.2 in Chapter 2.

4.2.2 Enriched SEI through Conjunctive Conversion and Plating Reactions.

To further distinguish the effects the simultaneous conversion reactions have on the SEI, the SEI constituents formed during the precursor stage at 0V vs. Li^+/Li and the following nucleation will be examined. From previous results, the W and Li_2O plays an important part in the high performance of the Coated Cu. The precursor components found on the bare Cu are similar to other components in LiTFSI in ether electrolytes.[83] The F1s region (**Figure 4.15a**) of the XPS shows the two peaks corresponding to the C-F bond and Li-F bonds at 688.2 eV and 684.6 eV respectively. The C-F bond arises from the LiTFSI salt, whereas the Li-F is from the decomposition of the LiTFSI. The Li1s (**Figure 4.15b**) also shows the Li-F peak at the binding energy of 58 eV. Additionally, other components from the breakdown of the electrolyte are seen: Li_xSO_y, Li-O, and $LiCO_2H$.[12] When it comes to the solvent derived components to the SEI, these appear in the O1s (**Figure 4.1c**) and C1s (**Figure 4.15d**) including COOR, C-OR, and C-C bonds.[12]With the thin layer of WO_3, the components stay similar to the relative intensities of the components changing.

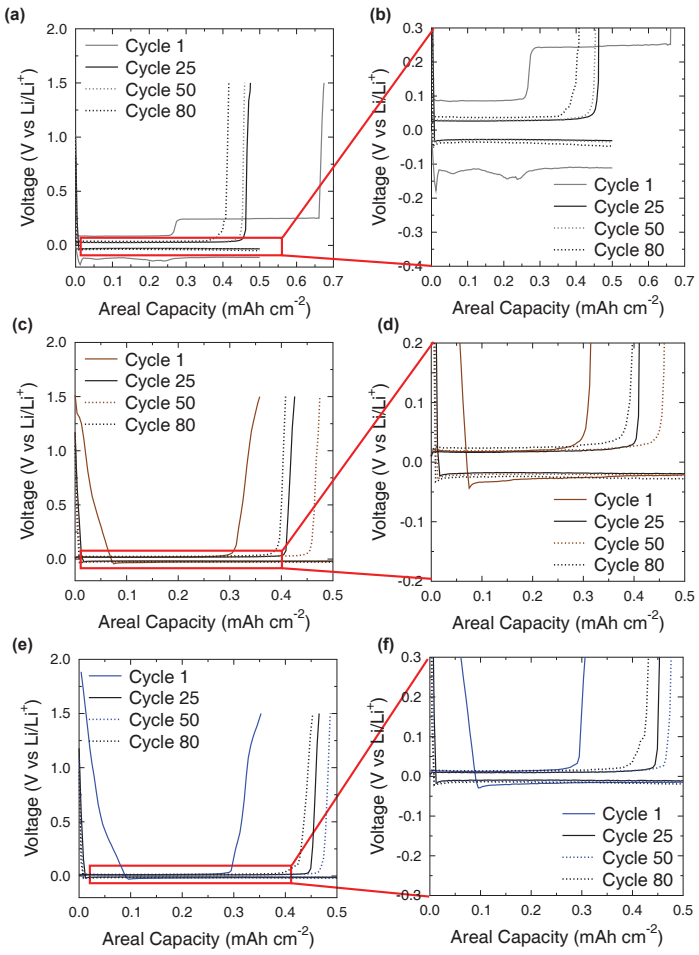

Figure 4.14: Voltage profile of coating 1 (**a, b**), Coating 2 (**c, d**), and Coating 3 (**e, f**).

The F1s region for Coating 1 (**Figure 4.15f**) shows a much greater amount of Li-F than the C-F bond, demonstrating a greater break down in the salt than that of the Cu. This could arise from the either the WO_3 or its reduced products helping to cleave additional C-F bonds.[79] In addition to the usual components Li_xWO_y shows up in the Li1s (**Figure 4.15f**) with a higher concentration of the carbonate. The presence of the Li_xWO_y demonstrates the incomplete conversion reaction, showing that all of the WO_3 has not been completely converted.[79] The unconverted WO_3 arises due to the overpotential that is needed to complete the conversion reaction being greater than the end parameters. This overpotential drives the potential needed below 0V vs. Li^+/Li.[79] The tungsten bronze is seen in the O1s (**Figure 4.15g**) with the peak for the Li-O bond. The O1s region shows the two compounds that are mainly increased during the conversion reactions. The loss of the

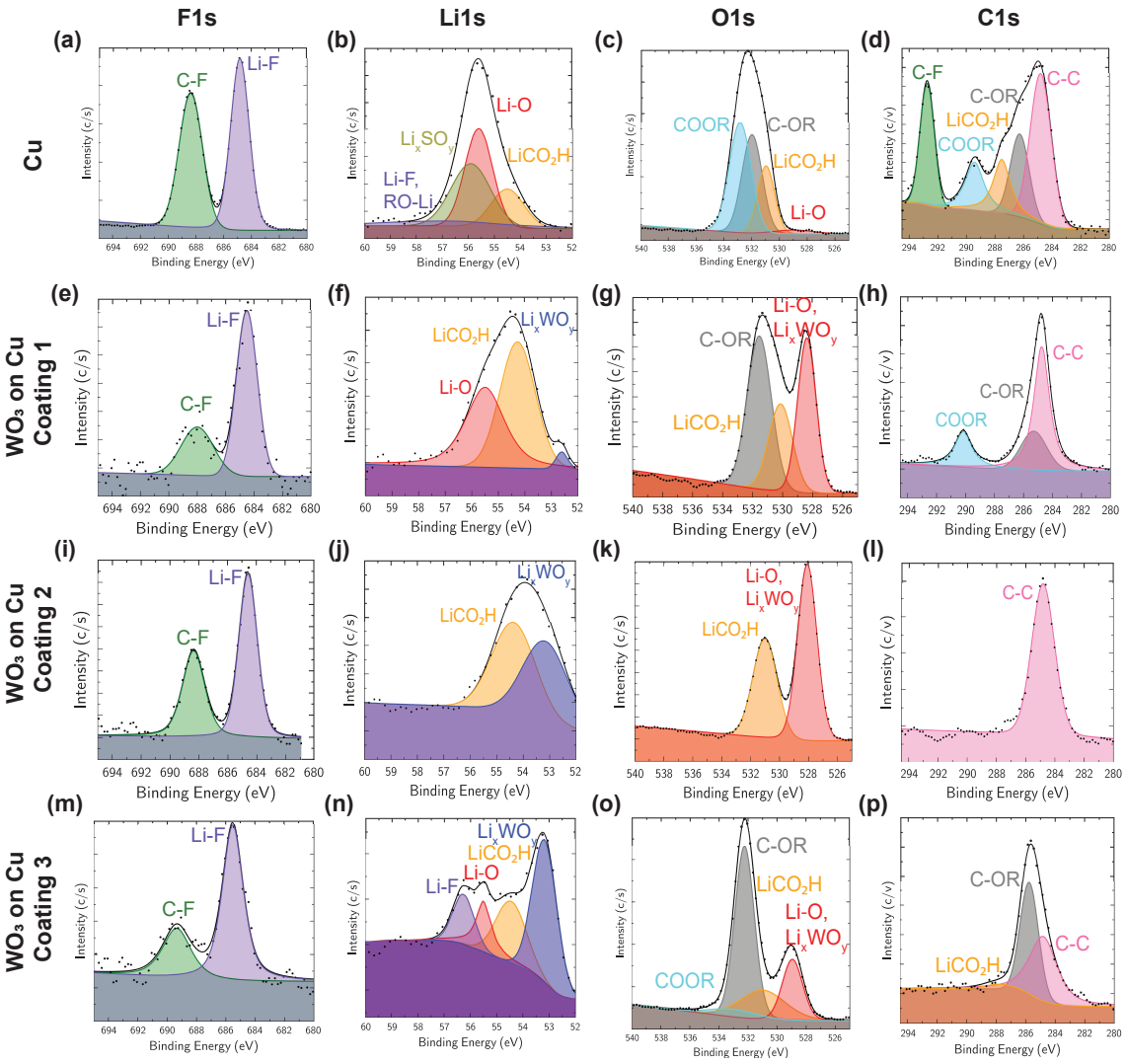

Figure 4.15: XPS of the SEI precursors at 0V vs. Li^+/Li discharge on Cu in the F1s (**a**), Li1s (**b**), O1s (**c**) and C1s (**d**) regions; Coating 1 in the F1s (**e**), Li1s (**f**), O1s (**g**) and C1s (**h**) regions; of Coating 2 in the F1s (**i**), Li1s (**j**), O1s (**k**) and C1s (**l**) regions; and of Coating 3 in the F1s (**m**), Li1s (**n**), O1s (**o**) and C1s (**p**) regions. Reproduced with permission from Ref. (*79*). Copyright 2019 American Chemical Society

COOR peak demonstrates a decreased amount of large products contributed by the solvents. This is further seen by the C1s (**Figure 4.15h**). The minimization of the extra carbon bonds shows a more complete decomposition of the solvents rather than the partial reactions shown on the bare Cu. The elimination of the C-F bond in the C1s region further shows the decreased content the pure LiTFSI has, and the more decomposed products are formed. Coating 2's F1s region shows

a similar ratio of the Li-F and C-F bonds as Coating 1, demonstrating the impact the oxide has shown in **Figure 4.15i**. The Li1s region (**Figure 4.15j**) for Coating 2 shows a minimized Li-O peak, but a larger amount of the L_xWO_y, the overpotential needed for this conversion reaction is greater than that of Coating 1 and 3 shown later. One explanation is the two areas seen on the SEM. These different areas can have differing potentials at which the conversion reaction begins due to the differing oxides present. The O1s region (**Figure 4.15k**) supports this by showing a large Li_xWO_y/Li-O peak. The only carbonate is seen in the O1s but completely disappears in the C1s region (**Figure 4.15l**). This shows that differing oxygen amounts of the WO_3 coating and the substrates fundamentally change the quantity and components within the SEI. When Coating 3 is considered, the F1s region(**Figure 4.15m**) shows the characteristic high Li-F peak now associated with the catalytic breakdown of the salt. The Li1s shows the Li-F peak in addition to the Li-O peaks. This shows the conversion reaction has progressed further than that of Coating 3. The presence of the tungsten bronze still demonstrates the depressed overpotential of the conversion reaction showing that not all of the WO_3 is completely converted. The O1s and C1s (**Figure 4.15o, p**) show the components of the decomposition of the solvents. These further show the catalytic effect the coating has on the SEI formation. The disappearance of the C-F peak in the three coatings is the most promising, considering that this cleavage forms Li-F. The SEI formed decreases/eliminates the unwanted salts of Li_xSO_y and promotes the formation of the beneficial Li-F which enriches the SEI.[30]

Further polarization to a nucleation capacity (0.0625 mAh cm^{-2}) allows for the study of the interfacial effects once the presence of Li is established on the surface, but before the bulk effects of Li metals reaction with the electrolyte becomes the dominating contributions. The different coatings were examined once the cells were disassembled and rinsed to prevent any further contamination by the electrolyte. The Cu was discussed in Chapter 2 and will be referenced here to compare against the nucleation of the three different coatings in **Figure 4.16**. On Coating 1, in the F1s region (**Figure 4.16a**), the C-F bond is completely gone with only the Li-F bond showing up. The Li1s and O1s regions (**Figure 4.16b & c**) show similar Li carbonate and Li tungsten bronze.

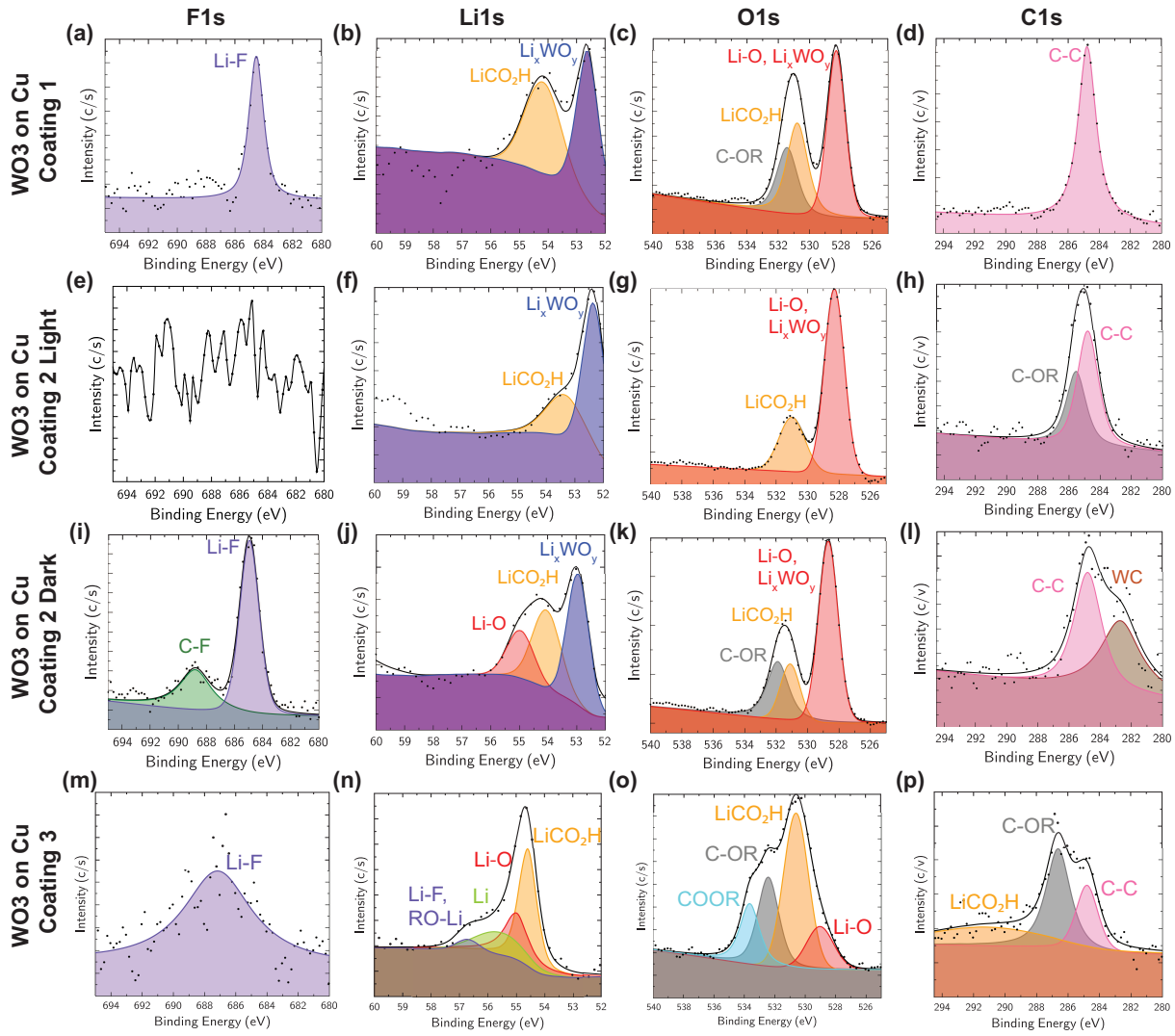

Figure 4.16: XPS of the SEI after discharged to 0.0625 mAh cm^{-2} on Coating 1 in the F1s (**a**), Li1s (**b**), O1s (**c**) and C1s (**d**) regions; Coating 2 "Light" in the F1s (**e**), Li1s (**f**), O1s (**g**) and C1s (**h**) regions; of Coating 2 "Dark" in the F1s (**i**), Li1s (**j**), O1s (**k**) and C1s (**l**) regions; and of Coating 3 in the F1s (**m**), Li1s (**n**), O1s (**o**) and C1s (**p**) regions. Reproduced with permission from Ref. (*79*). Copyright 2019 American Chemical Society

The addition of the small capacity isn't enough for Coating 1 to complete the conversion reaction.

Additionally, the C-OR is diminished, and the C1s (**Figure 4.16d**) just shows the C-C bond, giving further credence to the catalytic effect of the WO_3 coating. As two regions in the SEM were described as "light" and "dark", ' these two regions each had XPS ran to flesh the different interactions between them further. The "light" area of Coating 2, which showed the small Li nucleation, has a F1s region, which shows no discernible Li-F or C-F peaks. This section in

the Li1s, O1s, and C1s (**Figure 4.16f-h**) shows components similar to that of the precursor. When compared to the "light" side, the "dark" side does show the C-F and Li-F peaks in the F1s region (**Figure 4.16i**). The presence of the Li-F in this region indicates one of the primary causes of the discrepancy in the Li morphology. The Li-F smooths the deposition decrease the nucleation sites causing the larger particles. The Li1s region (**Figure 4.16j**), in addition to the tungsten bronze, the Li-O peak appears showing the conversion reaction in the area of Coating 2 is farther progressed than the "light". While the O1s region (**Figure 4.16l**) remains similar in composition, a new peak arises in the C1s region, mainly the WC peak. Coating 3 shows a single Li-F peak in the F1s region(**Figure 4.16**), with the same peak showing up in the Li1s region (**Figure 4.16n**) as well. Additionally, the Li1s region has the Li metal peak at 56 eV and the disappearance of the Li_xWO_y. During an increased overpotential, the conversion reaction for Coating 3 is driven to completion. Within the O1s (**Figure 4.16o**) and C1s (**Figure 4.16p**) regions, the contribution of the solvents in the SEI is slightly more diverse than the other coatings. When compared to the Cu in Chapter 2, the intensities of these regions and component contributions change. The higher polarization on these WO_3 coated Cu samples (except the "light" region) shows an enriched LiF consistent with smooth plating of Li and increased stability, as seen from the electrochemical performances. These XPS results confirm the active role the WO_3 has in the decomposition of the electrolyte, even creating a guided pathway.[79]

The electrolyte used has a lot to do with the SEI that is formed upon the surface. Previously all the tests have been performed using the standard ether electrolyte of 1M LiTFSI in DME/DOL. There is another salter that has been utilized exclusively with Li metal due to the ease of the formation of Li-F. The salt used is Lithium bis(fluorosulfonyl)imide (LiFSI); this differs slightly from the LiTFSI. The -CF_3 on the terminal ends of the molecule is replaced with just -F. This small change greatly increases the formation of Li-F due to the changes in bond energies. The C-F has an average bond energy of 485 kJ mol^{-1} whereas the N-F bond is 272 kJ mol^{-1}.[84] This change allows for the much easier removal and formation of the beneficial Li-F. Cu and the various WO_3 coatings were tested in a mixed electrolyte of 0.5M LiTFSI: 0.5M LiFSI in DME/DOL to

observe the performance when an additional easier pathway for decomposition is present. The

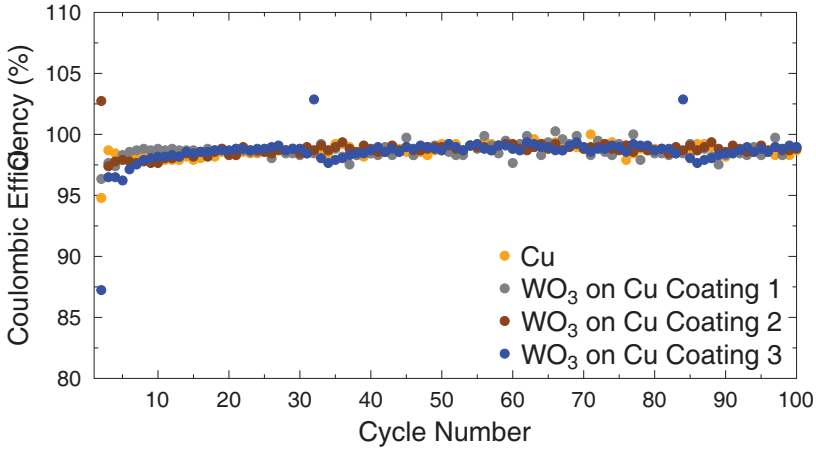

Figure 4.17: CE of dual salt electrolyte with Cu and the three coatings.

coloumbic efficiency of these tests is shown in **Figure 4.17**. With the added LiFSI, the benefits of the catalytic conversion of the LiTFSI are diminished, giving performances similar between all four samples. The average efficiencies for each sample were ≈98.66%, 98.9797%, 98.7448%, 98.5638% shown in **Table 3.6** and a MAD of the efficiency of 0.3789%,0.4092%, 0.3255%, and 0.5889% respectively. Coating 1 showed the least performance in pure LiTFSI; in the mixed salt electrolyte, the lesser amount of oxide prevents too much catalytic activity giving greater efficiency. Voltage hysteresis can be used to quantify the voltage polarization within the cell during cycles. Voltage hysteresis is calculated by taking the difference between mid-cycle potentials shown in the following equation.

Table 4.6: Quantified Avg. CE, CE MAD, Avg. Voltage hysteresis, and MAD of voltage hysteresis for cells cycled in dual salt.

Sample	Avg. Efficiency(%)	Efficiency MAD(%)	Avg. Voltage Hysteresis (V vs. Li^+/Li)	Voltage Hysteresis MAD (V vs. Li^+/Li)
Cu	98.6600	0.3789	0.0508	0.0273
WO_3 on Cu Coating 1	98.9797	0.4092	0.0488	0.0293
WO_3 on Cu Coating 2	98.7448	0.3255	0.0259	0.0135
WO_3 on Cu Coating 3	98.5638	0.5889	0.0739	0.0753

$$Voltage\,Hysteresis(V vs. Li^+/Li) = |Mid point\,Discharge(V vs. Li^+/Li) - Mid point\,Charge(V\ vs.\ Li^+/Li)| \quad (4.4)$$

The hysteresis supports Coating 1 being the best performer, with Coating 3 showing higher hysteresis due to the addition of the other components from the catalytic break down increasing the SEI which increases the internal resistance, increasing the voltage hysteresis. Coating 2 shows mediocre results but an extremely low hysteresis. Herein, the catalytic effect of the WO_3 is seen by the negative effects it can have when in competition with other SEI forming additives. The negative effects are negligible in this case due to the decomposition of the LiFSI overshadowing any of the positive effects it has, particularly with the LiTFSI.

4.2.3 Tungsten Mixed SEI Matrix for Reduction of "dead" Li.

As mentioned in Chapter 1, the issue of "dead" Li cannot be overlooked in the Li metal battery performance. The formation of the Li_xWO_y, followed by Li_2O/W upon complete conversion, is seen in the XPS results while forming other inorganic components. The W within the SEI forms an important role in the prevention of "dead" Li. The W can form an electronically conductive network within the SEI, decreasing the "dead" Li and maintaining the battery for longer, by minimizing Li loss.[79] The TEM and point EDX (**Figure 4.17a, b**) of Coating 3 at nucleation shows high W signals within the SEI upon the Li(dark).[79] The oxygen signal corresponds to the Li_2O present from the conversion reaction.

The presence of the W within the SEI increases the utilization of the Li metal, seen in the increased CE and stability. The doping doesn't increase the conductivity to the point of detriment due to the ionic conductivity being the dominant mechanism. EIS further demonstrates the effect of the W on the interfacial conductivity of the SEI. EIS studies on the different coatings shown in **Figure 4.19** after discharged to 0 V vs. Li^+/Li (**Figure 4.19a**), after plating 0.5 mAh/cm2 (**Figure 4.19b**), and after stripping the Li by charging to 1.5 V vs. Li^+/Li (**Figure 4.19c**). From the EIS, the interfacial resistance is much lower for the WO_3 coated on Cu for all three coatings than for the plain Cu, with Coating 3(blue) being the lowest. This interface persists even once all the Li

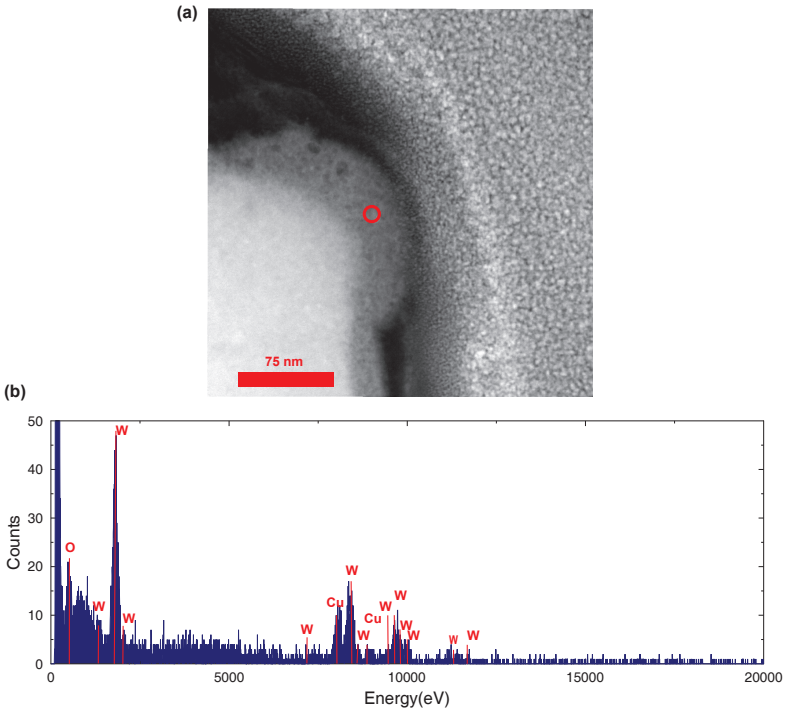

Figure 4.18: TEM of Li deposited under the WO_3 coating (**a**), with EDX (**b**) showing the W in the SEI layer. Reproduced with permission from Ref. (*79*). Copyright 2019 American Chemical Society

is removed. The resistivity of the interface (**Figure 4.19d**) is obtained by subtracting the first resistance from the second, divided by the area of the electrode following the two fitting circuits given in **Figure 4.19e**. In both circuits, R2 and CPE1 are attributed to the SEI, whereas R3 and CPE2 are attributed to the charge transfer with Li metal when present. The equivalent circuit I is used for fitting the EIS at 0 V vs. Li^+/Li and after charging. Equivalent circuit II fits the EIS of Li plated on the substrates. The fit shows that at 0 V vs. Li^+/Li, coating 3 provides an interface that is three times more conductive than bare Cu, with Coating 2 being higher than both Coating 1 and 3. After Li is plated, the coated Cu interface is 1.5 more conductive than bare copper, with all three coatings sharing similar resistivities. After the Li is removed, the interface provided by the WO_3 coatings provides an increased conductivity of 2-6 times that of bare Cu. The interface helps to decrease the resistivity of the interface at all stages of the cell cycle, decreasing the overpotential of the battery. The idea of a mixed conductive SEI has been further shown to have a substantial positive effect on stabilizing the plating and stripping of Li metal.[79,80,85]

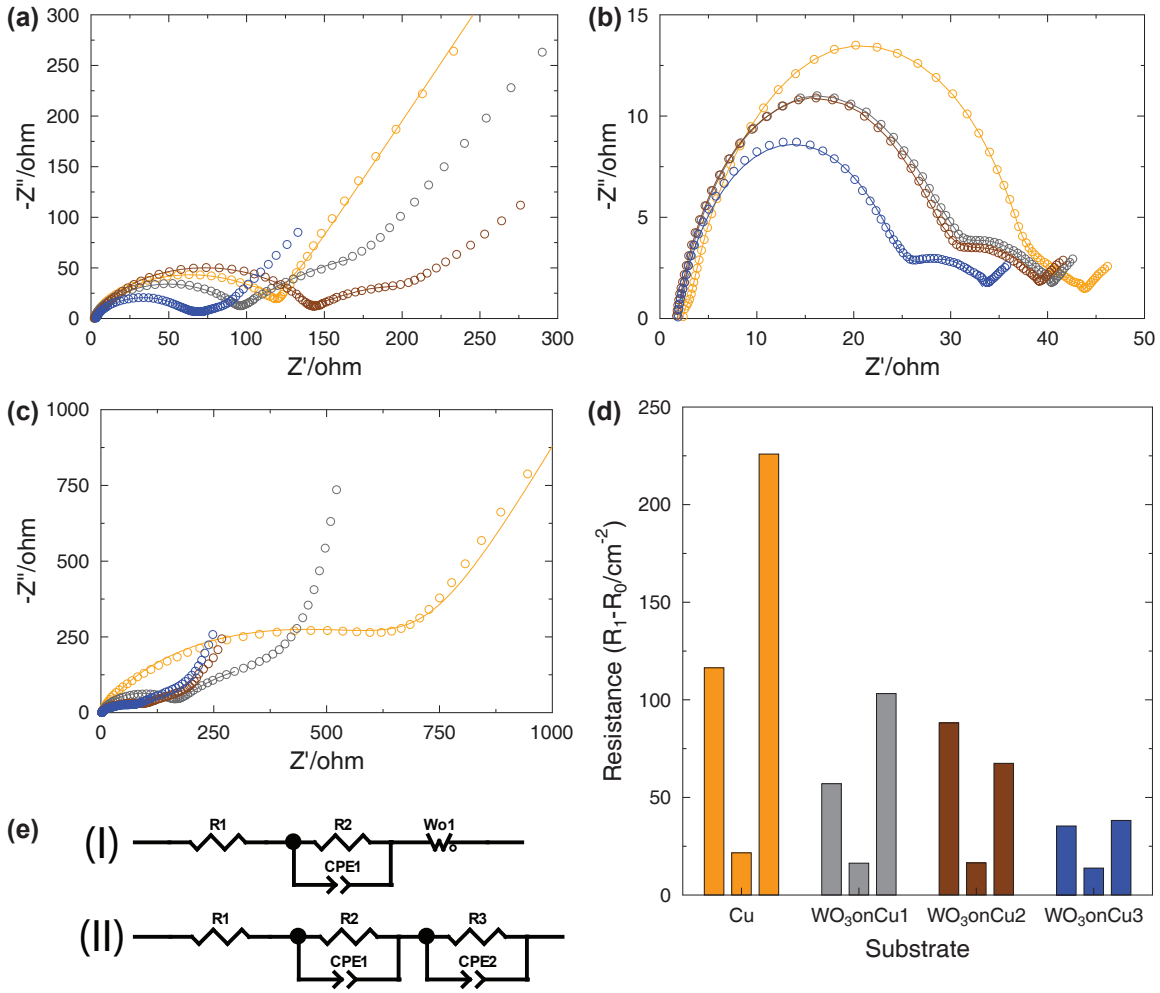

Figure 4.19: EIS analysis of the 3 coatings after discharge to 0V vs. Li^{+}/Li (**a**), after 1st plating (**b**), and after first charge (**c**). Bar graph (**d**) comparing the R_{SEI} of the 3 states of charge, with equivalent circuits (**e**) used for fitting.

At higher currents the impact of the W on the CE start to become minimized. At 1 mA cm^{-2}, the Cu starts to stabilize the CE (**Figure 4.20**) showing less variation. The efficiency is still poor compared to the WO_3 coated Cu but the trend starts to become similar. The presence of the W within the SEI plays a drastic effect on the voltage hysteresis (**Figure 4.20b**). Upon closer examination the Avg. Efficiency (**Table 3.7**) for Cu is 53.7272% with a MAD of 24.4968% . Coatings 1, 2, and 3 had efficiencies of 57.1195% with a MAD of 8.6954%, 75.0381% with a MAD of 7.7688%, and 76.7223% with a MAD of 5.7593%. The coating gives a bolstered efficiency of ≈25% and the MAD of the cell decreases dramatically. While the catalytic effects

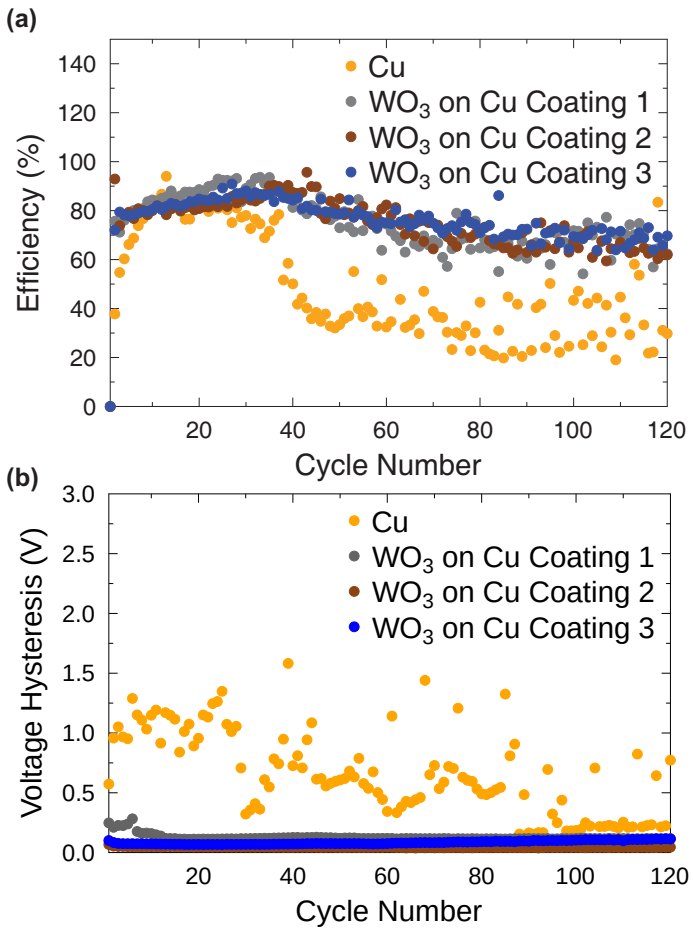

Figure 4.20: CE (**a**) and voltage hysteresis (**b**) of coatings cycled at 1 mA cm^{-2} current density. Reproduced with permission from Ref. (*79*). Copyright 2019 American Chemical Society

are diminished due to less time for formation of the SEI, the benefits of the W stabilization is still seen. Coating 3 stabilizes the most with the lowest Voltage hysteresis of 0.1489 V vs. Li^+/Li with a MAD of 0.0408 V vs. Li^+/Li showing a highly stable cell even after 120 cycles.

The further increase of current density to 2 mA cm^{-2} shows the decreased effectiveness of the catalytic breakdown and subsequent SEI formation by a similar CE trend shown in **Figure 4.20a**. Coating 3 shows the least fluctuation in the efficiency but the same decrease to ≈60% . After 200 cycles, the voltage hysteresis (**Figure 4.20b**) shows Coating 1 becoming unstable after 100 cycles with Cu and Coating 2 demonstrating similar hysteresis. Coating 3 has the same initial hysteresis where the Cu and Coating 2 have a slight decrease. After 500 cycles (**Figure 4.20c**) the Cu becomes unstable having large fluctuations, beginning at cycle 200. Coating 2 is very

Table 4.7: Quantified Avg. CE, CE MAD, Avg. Voltage hysteresis, and MAD of voltage hysteresis for cells cycled at 1 mA cm^{-2}.

Sample	Avg. Efficiency (%)	Efficiency MAD (%)	Avg. Voltage Hysteresis (V vs. Li^+/Li)	Voltage Hysteresis MAD (V vs. Li^+/Li)
Cu	53.7272	24.4968	0.6233	0.2986
WO_3 on Cu Coating 1	75.1195	8.6954	0.4389	0.4272
WO_3 on Cu Coating 2	75.0381	7.7688	0.3299	0.2806
WO_3 on Cu Coating 3	76.7223	5.7593	0.1489	0.0408

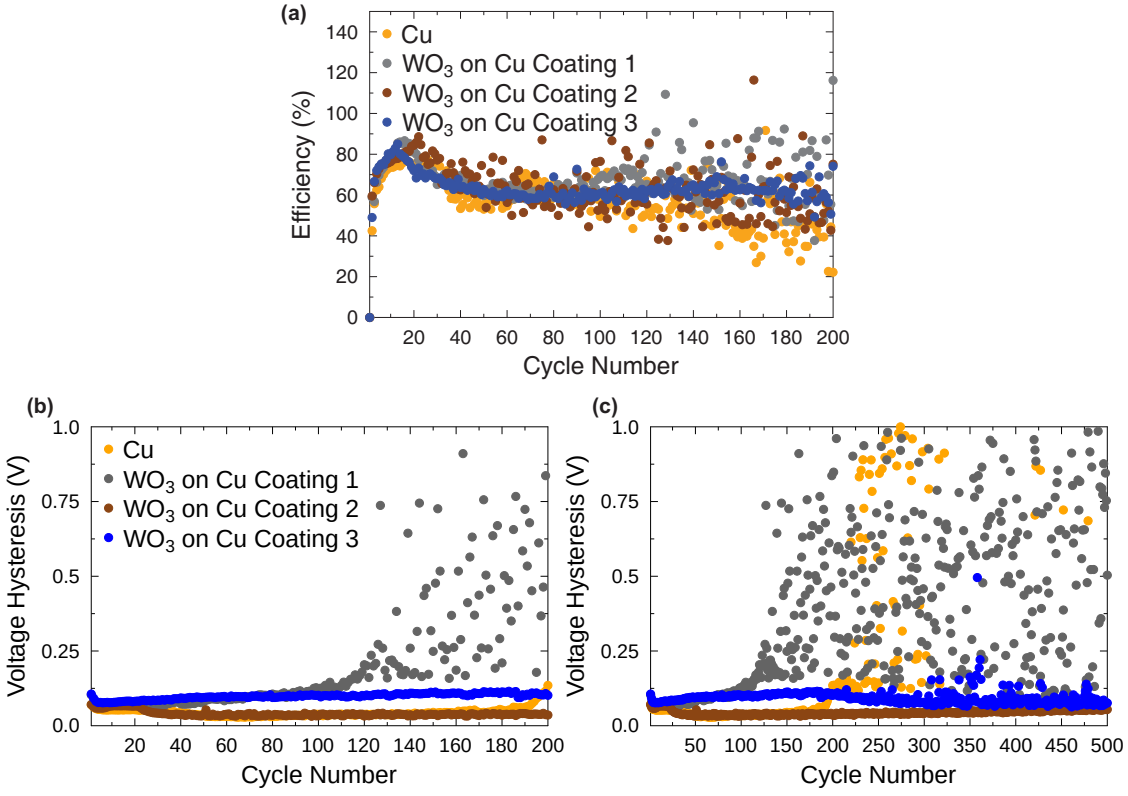

Figure 4.21: CE (**a**) and voltage hysteresis (**b, c**) of coatings cycled at 2 mA cm^{-2} current density. Reproduced with permission from Ref. (*79*). Copyright 2019 American Chemical Society

stable when pertaining to the voltage hysteresis, whereas there is some fluctuation for Coating 3 starting at cycle 300. The quantified values for the Avg. CE after 200 cycles and the Avg. Voltage Hysteresis after 500 cycles further show this difference (**Table 4.8**). The WO_3 coating increases the Avg. Efficiency after 200 cycles by ≈6 %. While Coating 2 has the lowest hysteresis of 0.0438

Table 4.8: Quantified Avg. CE, CE MAD, Avg. Voltage hysteresis, and MAD of voltage hysteresis for cells cycled at 2 mA cm^{-2}.

Sample	Avg. Efficiency(%)	Efficiency MAD(%)	Avg. Voltage Hysteresis(V vs. Li^+/Li)	Voltage Hysteresis MAD(V vs. Li^+/Li)
Cu	56.9117	9.352	0.6233	0.6089
WO_3 on Cu Coating 1	62.5336	6.3237	0.4286	0.2808
WO_3 on Cu Coating 2	63.5818	9.8093	0.0438	0.006
WO_3 on Cu Coating 3	63.4728	4.4925	0.0926	0.0138

V vs. Li^+/Li with a MAD of 0.006 V vs. Li^+/Li, the MAD of the efficiency is 9.8093 % similar to that of Cu (9.352%). The increased amount of W can help to regenerate the "dead" Li causing some fluctuation in the efficiency, while mitigating the impedance increased by the accumulation of the "dead" Li.[79]

4.3 Conclusion

The presence of the oxide on the surface of W and the subsequent coating of WO_3 onto Cu shows an interaction between the tungsten oxide and the electrolyte. During the conversion reaction, the compounds of W and Li_2O are formed. During this conversion reaction, altering the SEI through the catalytic decomposition of electrolyte materials has been observed. Li_2O enriches the SEI with greater inorganic compounds, increasing SEI's strength. The W creates a framework upon decomposition allowing for the reactivation of "dead" Li whereas Cu forms no such framework leaving "dead" Li isolated (**Figure 4.21**). The novel application of WO_3 provides a new method for modifying the SEI by guided decomposition and in situ SEI formation with wanted compounds dispersed throughout providing new solutions for the challenges of Li metal batteries.

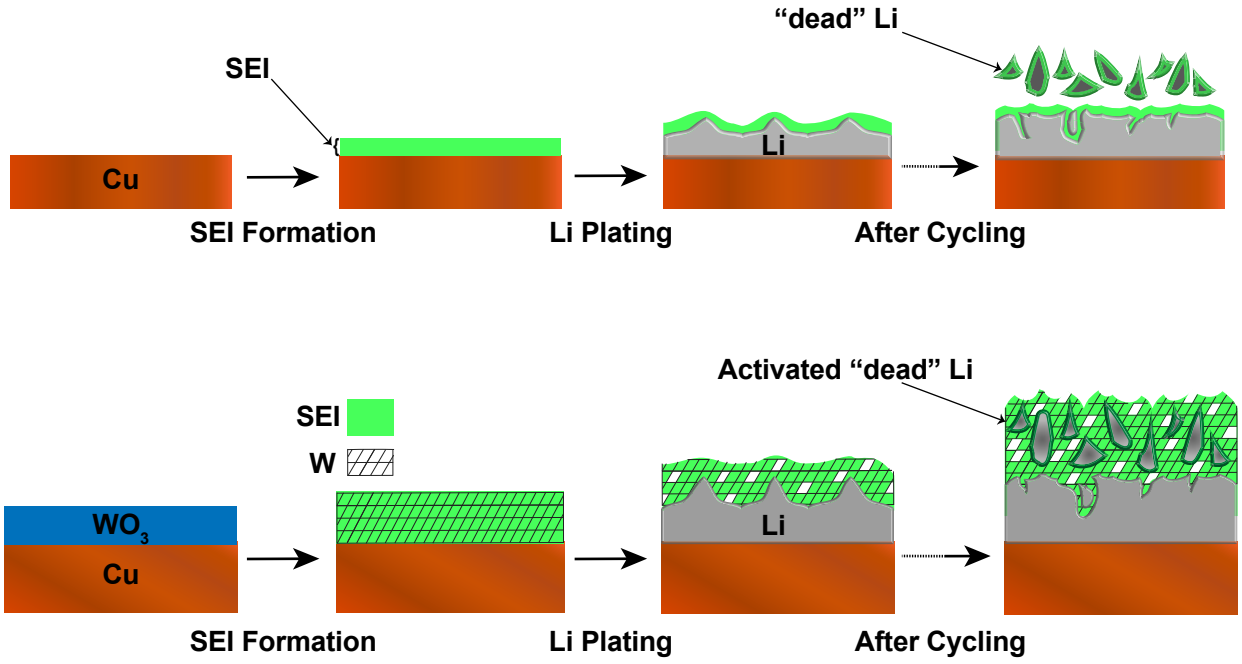

Figure 4.22: Descriptive diagram showing the impact the W has in the SEI. Reproduced with permission from Ref. (*79*). Copyright 2019 American Chemical Society

5 Exploration of Conversion Materials: Preliminary Screening and Application

5.1 Introduction

The positive effects of the tungsten oxide coating on the surface of Cu raise other questions. Does it have to be an oxide? Does it have to be W? This chapter seeks to answer these questions through a preliminary study of other conversion materials and the promising application as a separator interface. Through this initial study, new research directions can be used for others to continue pushing the limits further.

5.2 Exploration of Novel Conversion Materials

To begin with the exploration of other novel conversion materials, some metrics need to be observed. **Table 5.1** shows the different conversion materials we screened, including five different W compounds and four different oxide compounds, with their corresponding oxidation states of the metal, the decomposition products, the bandgap of said products, the metals conductivity, and the calculated migration energies of Li through the decomposition products. These material properties help compare the different aspects of the conversion materials being screened and, therefore, help establish patterns. Samples were coated onto the Cu through slurry and powder method, WO_3 was included to compare a promising candidate following the same preparation methods and as a standard for positive performance.

5.2.1 Materials Response to Cycling

The coated Cu samples were electrochemically cycled to identify the performance against Li metal. The average efficiencies through 100 cycles are shown in **Figure 5.1**. A high coulombic efficiency and low voltage hysteresis are ideal precursor identifiers to show promising materials. Here it's seen that the WO_3 and AgF show the highest efficiency. The WCl_6 had the worst performance, being completely unstable against Li metal. While the instability of the WCl_6 is seen, the WS_2 had the worst efficiency. This is likely due to the formation of lithium sulfides that can

Table 5.1: Conversion Materials and the decomposition products with bandgaps and calculated migration energies

Sample	Oxidation State	Lithium Decomposition Product	Band Gap(eV)[57] Decomposition Product	Metal Conductivity(S/m)[84]	Calculated Migration Energies of Li^+ (eV)[86]
WO_3	+6	$3Li_2O$	4.7	$2x10^7$	0.15
WS_2	+4	Li_2S	3.9	$2x10^7$	0.34
WSe_2	+4	Li_2Se	3.72	$2x10^7$	0.35
WTe_2	+4	Li_2Te	2.52	$2x10^7$	0.35
WCl_6	+6	6LiCl	6.25	$2x10^7$	0.45
VSe_2	+4	Li_2Se	3.72	$0.0489x10^6$	0.35
$MnSe_2$	+4	Li_2Se	3.72	$6.2x10^5$	0.35
Fe_3O_4	+2,+3	$4Li_2O$	4.7	$1x10^7$	0.15
Cr_2O_3	+3	$3Li_2O$	4.7	$7.9x10^6$	0.15
AgF_2	+2	2LiF	8.9	$6.2x10^7$	0.73
Cu_2O	+1	Li_2O	4.7	$5.9x10^7$	0.15

dissolve into the electrolyte contaminating all the Li within the cell and causing a drop in the CE. Future tests for WS_2 should include the additive $LiNO_3$ due to the synergistic effects it has with sulfur compounds in SEI formation. However, it was not added to prevent any unnecessary correlations from being drawn.[28] The average voltage hysteresis in **Figure 5.2** shows supporting information for the performance of the various conversion materials. The instability of the WCl_6

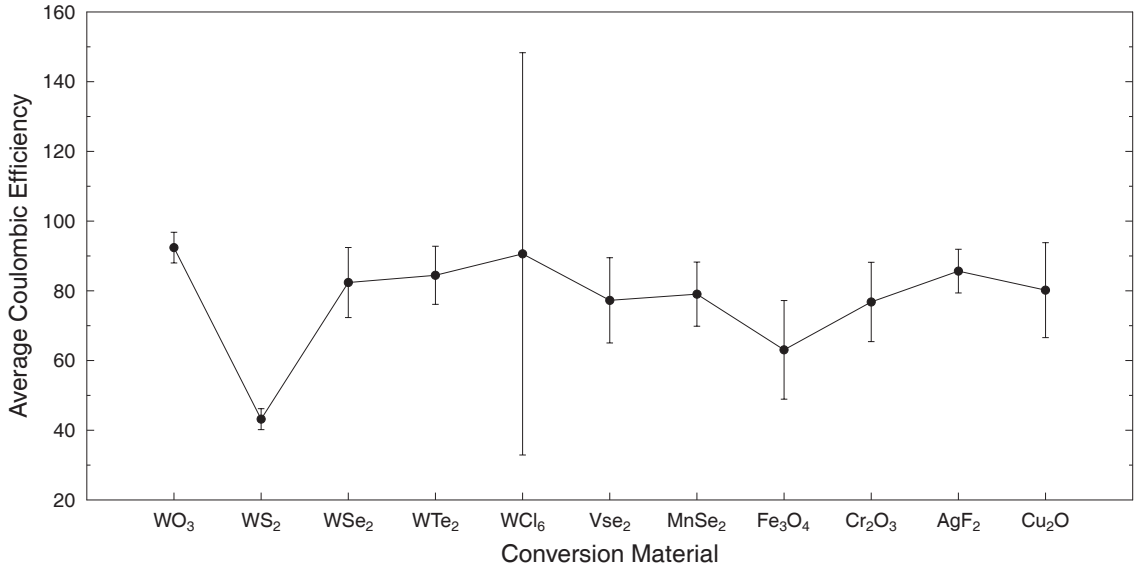

Figure 5.1: Average coulombic efficiency for the various conversion materials with the error bar showing the MAD for 100 cycles.

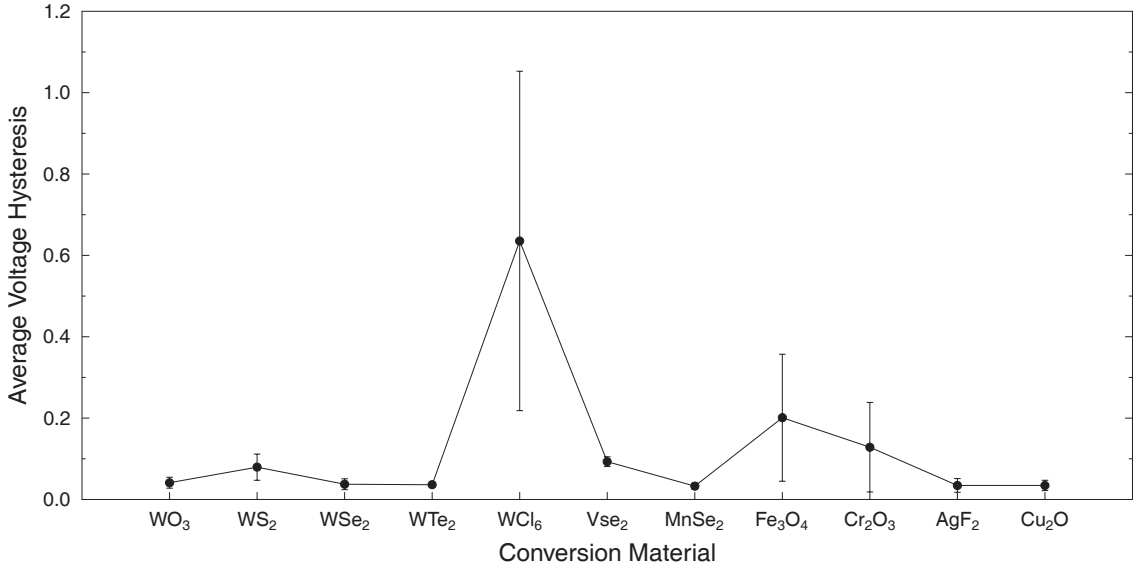

Figure 5.2: Average voltage hysteresis for the various conversion materials with the error bar showing the MAD for 100 cycles.

is magnified in this case, showing the substantial potential difference in the plating and stripping of Li of ≈0.63 V vs. Li^+/Li. Such a large overpotential is detrimental to the cell. It is unclear as to the causes for the instability as it has been shown that LiCl can be used as a Li metal surface modifier.[87] One explanation is that the SEI formed with the LiCl contains a much higher content of LiCl than layers with other conversion materials. This, coupled with LiCl's low Li migration energy (0.45 eV), causes the SEI to be highly resistive, causing broader voltage polarization. The voltage hysteresis reinforces the high performance of the WO_3 and AgF. This, coupled with the

Table 5.2: Conversion Materials

Sample	Efficiency	Voltage Polarization
WO_3	92.3952±4.4012	0.0412±0.0134
AgF	85.6549±6.2675	0.0345±0.0169

increase in efficiency, gives promising results. A caution evaluating these results is that this film is very thick, which can cause mechanical failure due to volume expansion, as mentioned in Chapter 3. **Table 5.2** shows the values of the CE and hysteresis for the WO_3 and AgF. The WO_3 has a higher efficiency of 92.3952±4.4012%, whereas the AgF has an efficiency of 85.6549±6.2675%. The voltage hysteresis shows the AgF having a lower average overpotential than that of the WO_3.

This is due to the high lithiocity of the LiF formed and the addition of the Ag. Ag forms an alloy with Li and can act as both an ionic conductor and an electronic conductor with its high metal conductivity.[88] To further flesh out these interfacial resistivities and the impact the Ag and LiF

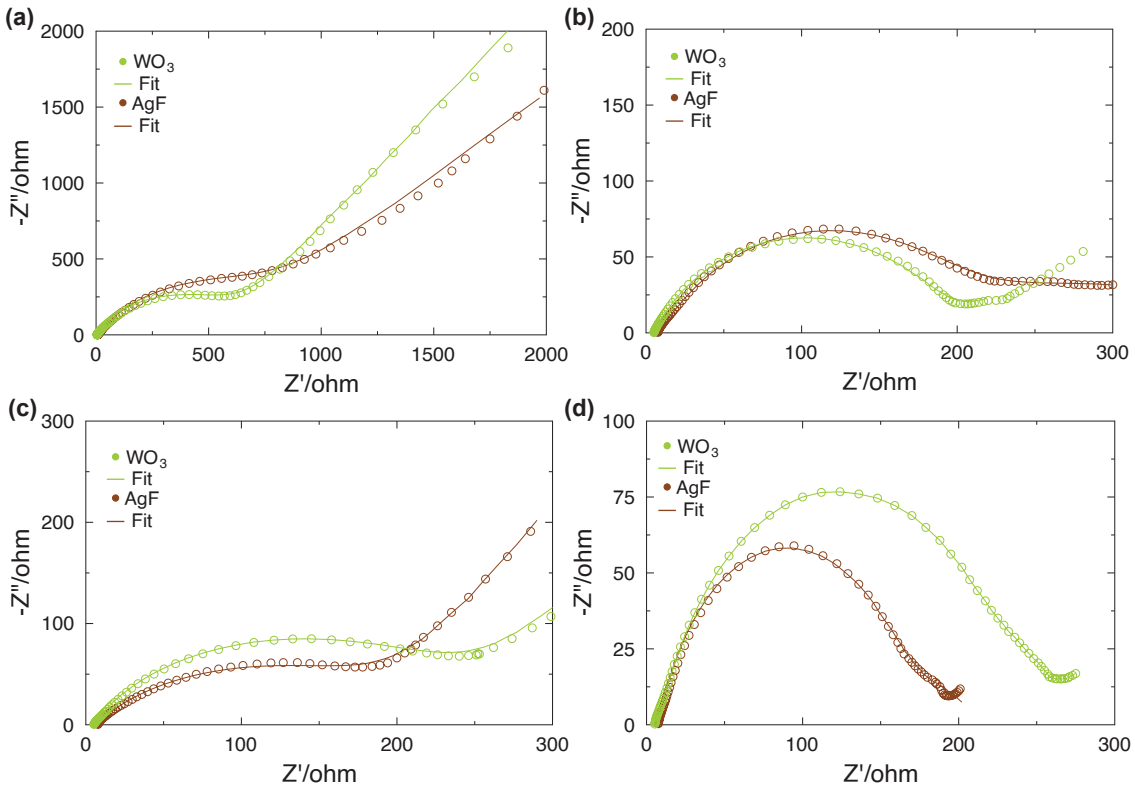

Figure 5.3: Nyquist Plots of WO_3 and AgF coated Cu in carbonate electrolyte at 0V vs. Li^+/Li (**a**), after the first discharge (**b**), after the first charge (**c**), and after the fifth discharge (**d**).

has on the SEI, EIS was utilized. 4 Stages of the cell cycles were tested after discharge to 0V vs. Li^+/Li (the end of the conversion reaction before the Li metal plates), after the first plating of Li metal, after the 1st stripping of Li metal, and after the 5th plating of Li metal. These stages give a snapshot into the formation and stabilization of the SEI. The coatings were first tested in carbonate electrolyte (1M $LiPF_6$ in Ethylene Carbonate (EC) and Dimethyl Carbonate (DMC)). The 0V vs. Li^+/Li EIS (**Figure 5.3a**) shows both layers have similar high resistances before Li is plated. After Li is plated for the first time (**Figure 5.3b**), the resistance decreases substantially, with the WO_3 being slightly less than that of the AgF. After the first stripping (**Figure 5.3c**), the resistance is maintained at the low value. After the 5th discharge, the stability of the SEI and the interface is

demonstrated.

In ether electrolyte, the two coatings start to become more differentiated. The EIS shows that at 0V vs. Li^+/Li (**Figure 5.4a**), the AgF coating has a much lower resistance than that of the WO_3. This trend carries through the first discharge (**Figure 5.4b**), the first charge (**Figure 5.4c**), and the 5th discharge (**Figure 5.4d**). It should be noted that the AgF on the first charge showed some instability in the charge transfer region; this is attributed to some of the coating having loose contact giving the instability. However, after the 5th cycle, stability has returned. This shows the importance of the first few cycles in the formation of stable SEIs. When examined together, the

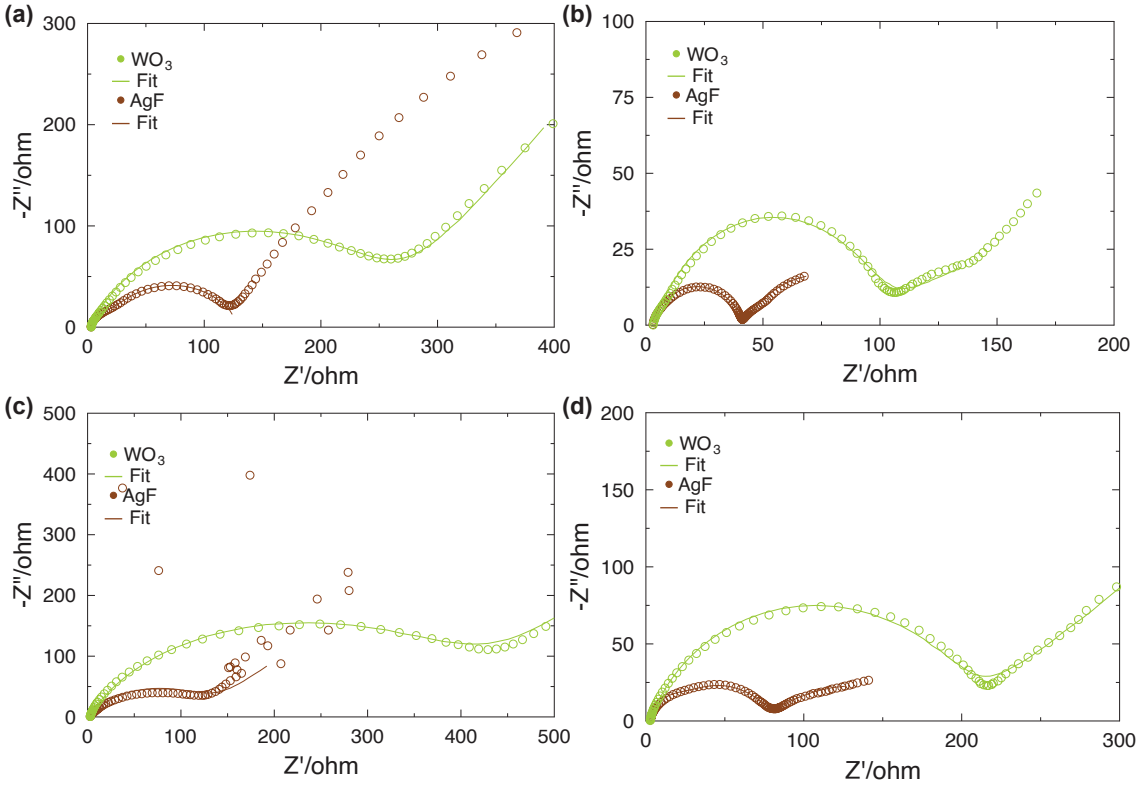

Figure 5.4: Nyquist Plots of WO_3 and AgF coated Cu in ether electrolyte at 0V vs. Li^+/Li (**a**), after the first discharge (**b**), after the first charge (**c**), and after the fifth discharge (**d**).

calculated SEI resistivities, shown in **Figure 5.5**, the AgF shows an overall much lower resistance to than the WO_3. The high conductivity of Ag in and of itself is one of the reasons, and another reason is that the Ag-Li alloy that is formed can help to enhance the layer due to its expansion (≈17%).[88] This helps to fill any gaps in the SEI. When compared to the efficiency and the SEI

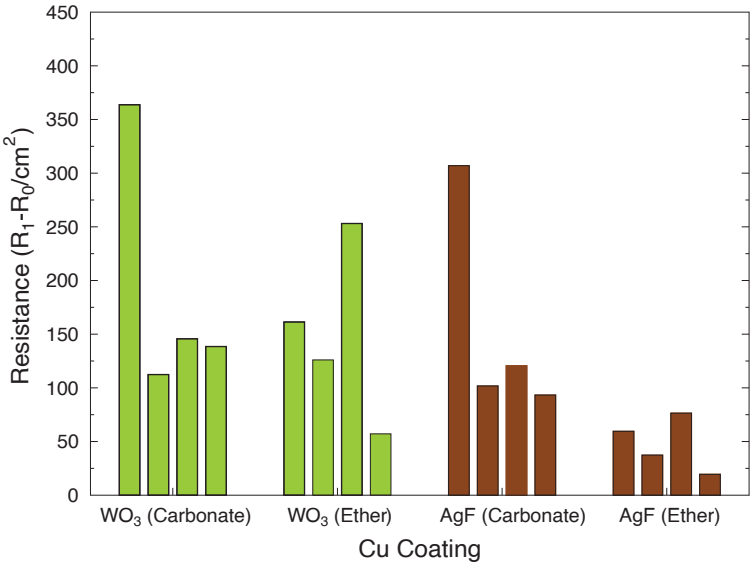

Figure 5.5: Bar graph showing the SEI resistivity of the WO_3 and AgF coated Cu in ether and carbonate electrolyte at 0V vs. Li^+/Li, after the first discharge, after the first charge, and after the fifth discharge (from left to right), with equivalent circuit used for calculation and fitting inset.

resistivity for the ether electrolyte, the R_{SEI} is too small. Bingbin Wu et al.[68] showed that the SEI must have a certain resistance threshold to mitigate further dendrite growth. The SEI produced by the AgF, while it has larger resistance, is more prone to generate more Li dendrites, thereby more "dead" Li. This leads to the spikes in the efficiency observed during cycling.

5.3 Application as Separator Coating

Coating the substrate has been a valid method for modifying the SEI and the plating and stripping of Li metal. However, the issue of long term stability of the modified layer decreases as more Li is stripped and deposited. This leads to the idea of the application of the coating onto the separator. The separator would become a functional separator forming a modified interface that expands with the Li and is always present "on top" of the Li and the SEI. **Figure 5.6** shows the schematic for this coating, where the Li-ions would pass through the coating and plate on the current collector similar to the coated current collector, however, this coating is bound to the separator. The two top coatings, previously mentioned being applied to Cu, were coated onto the polyethylene separator following the same coating procedure previously mentioned. The separator

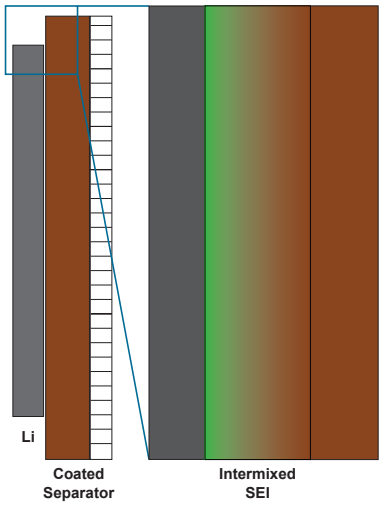

Figure 5.6: Schematic of the coating separator and the subsequent SEI formed.

was dried then placed within the cell with the coating layer facing the Cu anode where Li would be plated. The two electrolytes were used, carbonate and ether, for the cycling. The electrochemical results shown in **Figure 5.7** shows the CE efficiencies for the carbonate (**Figure 5.7a**) and ether (**Figure 5.7b**). Immediately the performance of the two coatings shows completely different interactions due to the electrolyte used. The carbonate electrolyte is much more stable than that of the ether with regards to the CE performance. The voltage polarization (**Figure 5.8**) tells a similar story. The WO_3 (**Figure 5.8a**) and AgF (**Figure 5.8b**) coatings show a polarization stereotypical of SEI growth. As the cells cycle, the SEI grows, increasing the cell impedance, thereby increasing the polarization between the plating and stripping of a cycle. The WO_3 shows an increase to higher polarization than that of the AgF. The coatings in ether electrolyte show a rough low impedance cycle behavior. This indicates instability within the electrochemistry of the cell, particularly in the gaps seen. These show areas where longer stripping is taking place. This longer stripping is attributed to irreversible side reactions taking place during discharge, stealing the Li, thereby making it take longer to reach the voltage cutoff. This is seen by these long white gaps taking place after very short cycles. This phenomenon additionally contributes to the high variability within the CE of the cell.

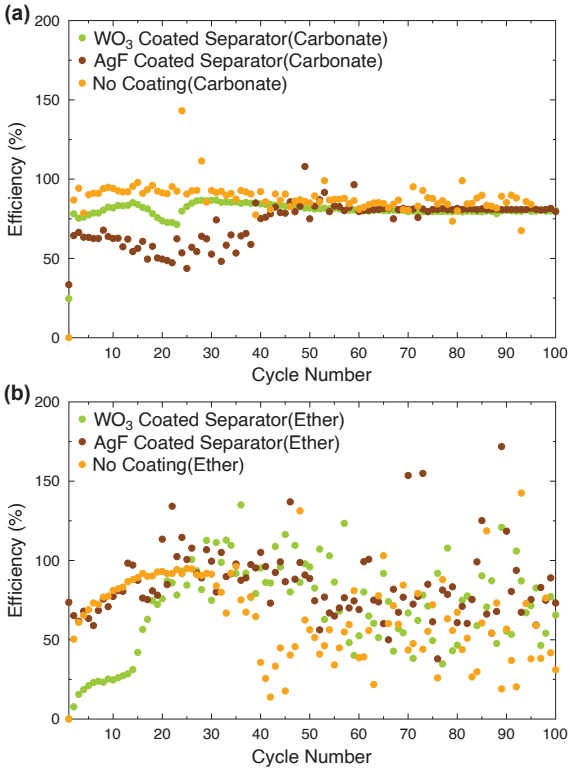

Figure 5.7: Coulombic efficiencies of coated separator in carbonate electrolyte (**a**) and ether electrolyte (**b**)

5.3.1 Interfacial Resistivity Changes

Exploration of this modified separator was further probed through EIS. Since differing voltage polarizations are seen between the coatings and electrolytes, EIS should quantify these differences and help identify which aspect of the battery is contributing to this polarization. This is due to voltage polarization being a qualitative measure of the cell's total internal resistance, not necessarily of one specific aspect. The Nyquist plots of the carbonate show that from the beginning before any Li is plated (**Figure 5.9a**), the AgF has a much lower R_{SEI} than the WO_3. This differs from when the coating was on the current collector, where both coatings had similar resistances. The WO_3 coating shows a lower R_{SEI} when coated on the separator as compared to the coated current collector, however after first discharge (**Figure 5.9b**), the first charge (**Figure 5.9c**) and the 5th discharge (**Figure 5.9d**), the resistances stabilize, same with the AgF coating. In ether electrolyte (**Figure 5.10**), the overall resistivities are much lower for both coating materials. At

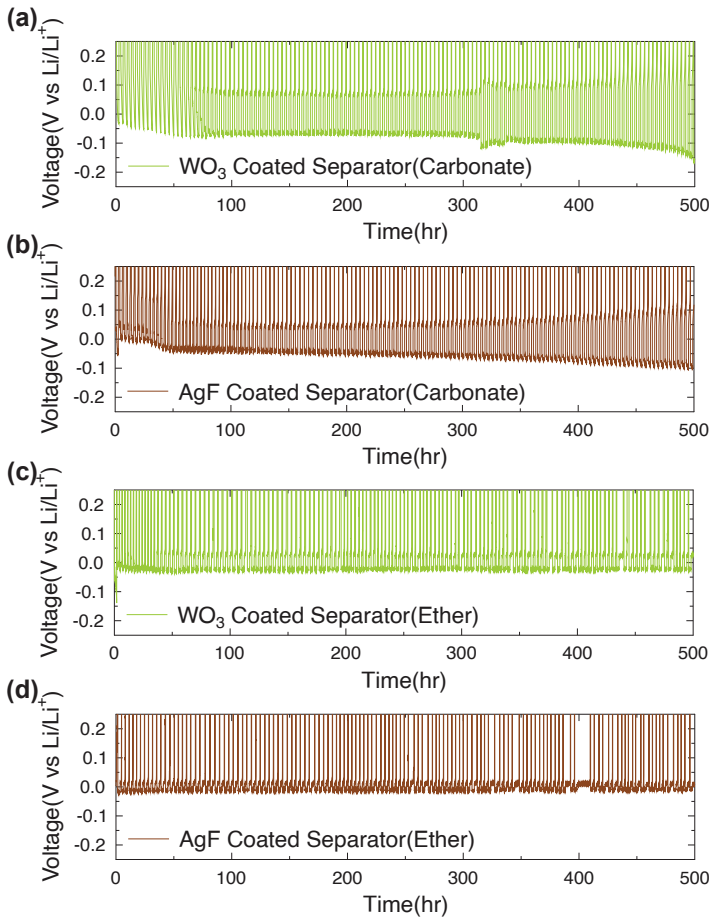

Figure 5.8: Time vs. Voltage graph of coated WO_3 (**a**) and AgF (**b**) separator in carbonate electrolyte and WO_3 (**c**) and AgF (**d**) separator ether electrolyte.

0V vs. Li^+/Li (**Figure 5.10a**), the R_{SEI} both show similar performance, with the WO_3 coating showing a slight instability in the R_{ct}. After Li is plated on the surface of the current collector (**Figure 5.10b**), this instability disappears. Additionally, the AgF coating shows a further decrease in the R_{SEI}. The R_{SEI} of the WO_3 coating after charging (**Figure 5.10c**) and after the 5th discharge (**Figure 5.10d**) stabilized, as did the R_{SEI} of the AgF coating. When the R_{SEI} of the various coatings in the differing electrolytes is examined, the coatings on the separators generally produce a lower R_{SEI} than that of coatings on the current collector. Interestingly the positive impact the AgF has on the R_{SEI} is further increased than that of coatings on the current collector. The reason for this is that the SEI that is formed when the coating is placed on the separator vs. the current collector can be much thinner. This is due to the freedom of movement the coating has. This forms

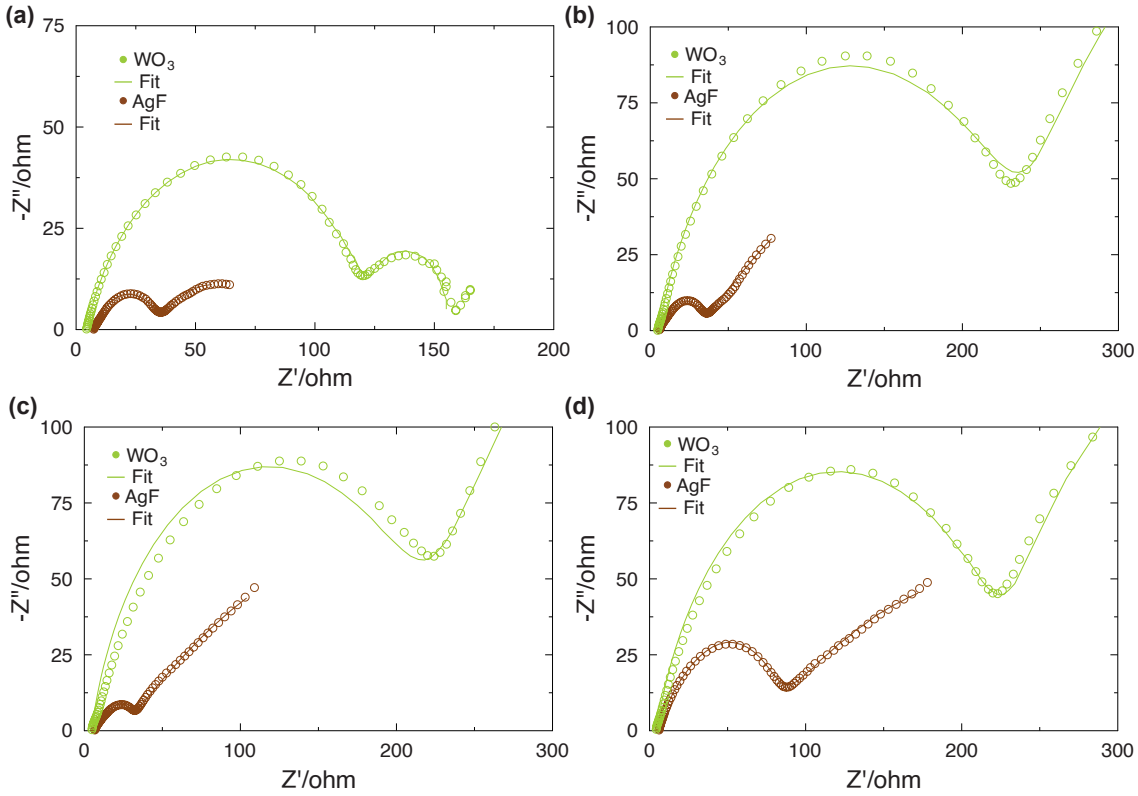

Figure 5.9: Nyquist Plots of WO_3 and AgF coated separator in carbonate electrolyte at 0V vs. Li^+/Li (**a**), after the first discharge (**b**), after the first charge (**c**), and after the fifth discharge (**d**).

a kind of tri-layer SEI where there is an inorganic layer formed on the plated Li initially a mix of the separator coating and the electrolyte decomposition products. The organic layer is minimized, decreasing the resistivity. This minimization, particularly in ether electrolyte, is not effective at allowing smooth Li plating and stripping, as seen from the CE. The carbonate electrolyte benefited greatly from the separator coating, though the lead time on the stable cycling is disconcerting. Taking between 30-40 cycles to stabilize is not ideal; however, the mechanism for this increased performance is still unknown.

5.4 Conclusion

In conclusion, screening for new materials to be candidates for future work has been conducted. AgF is a promising new material for study. AgF, when reacted with Li, will form Ag-Li

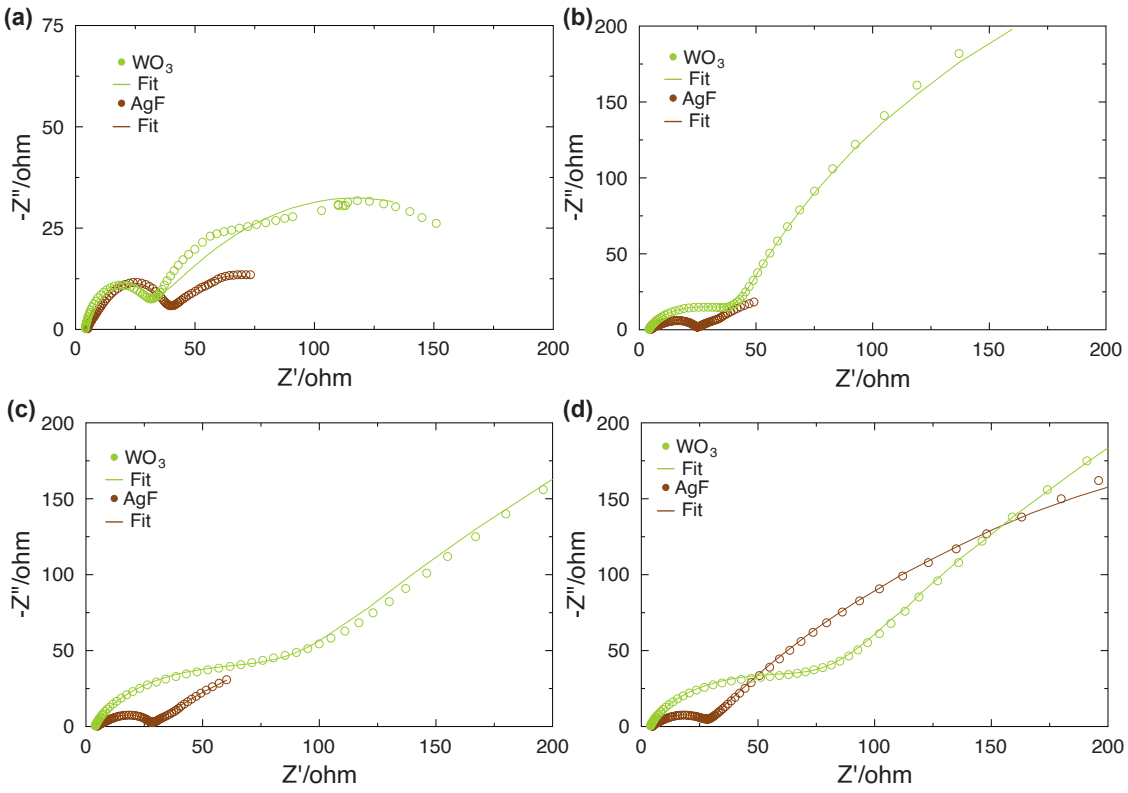

Figure 5.10: Nyquist Plots of WO_3 and AgF coated separator in ether electrolyte at 0V vs. Li^+/Li (**a**), after the first discharge (**b**), after the first charge (**c**), and after the fifth discharge (**d**).

alloy and Li-F, this allows for the creation of a hybrid interface with the increased electronic conductivity of the Ag to help revive "dead" Li while giving the Ag-Li alloy to increase the Li^+ flux within the SEI. When these materials were applied to the separator to create a different type of interface, the coatings performed well in the carbonate electrolyte. Still, they showed no marked improvement over not coating in ether electrolyte. This is speculated to stem from the lack of a key decomposition component formed when the coating was on the current collector but not present on the separator; however, the exact mechanism has yet to be seen.

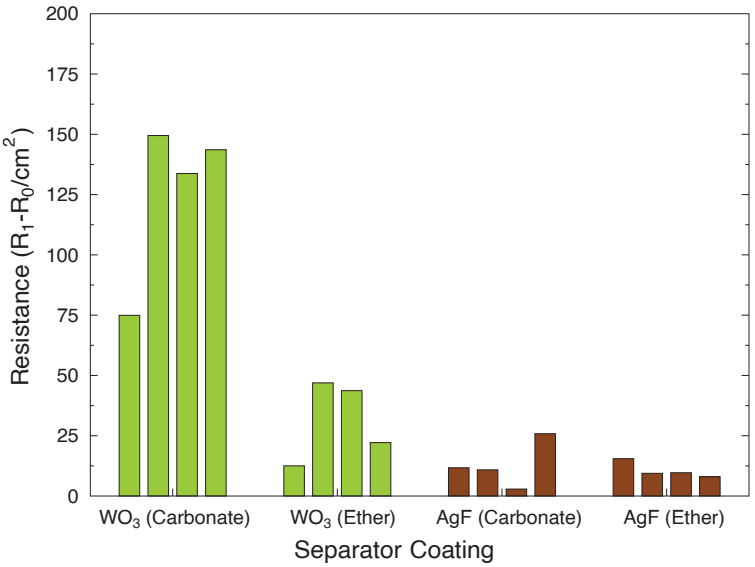

Figure 5.11: Bar graph showing the SEI resistivity of the WO_3 and AgF coated separator in ether and carbonate electrolyte at 0V vs. Li^+/Li, after the first discharge, after the first charge, and after the fifth discharge (from left to right), with equivalent circuit used for calculation and fitting inset.

6 Conclusion

This research aimed to explore the fundamental nature of the interfacial reactions in Li metal batteries. The particular interfaces explored were those of the metal-metal interface between the Li and the current collector it was plated on. Through electrochemical testing and surface characterization, it was found that W had a positive effect on the plating of Li and demonstrated some interface interaction. Upon further investigation, this modification came not from the metal-metal interface but the metal-metal oxide interaction between the Li and the WO_3. This research helped fill the gap in knowledge on the exact role that the Cu current collector and other current collectors have on the plating and stripping of Li metal.

The crystal-crystal interface was explored utilizing texture analysis and the single crystals Cu(100), Cu(110), and W(100). The texture revealed that the crystal has an impact on the initial crystal structure of the lithium plated on top of it. This impact did not positively affect the plating and stripping of Li in and of itself. The texture further revealed that the principal texture element of Li grown through electrodeposition is fiber texture. This texture is uniaxial and has a direct correlation with dendrites. The crystal structure and thereby the texture is further impacted by the pressure exerted by the separator, where the higher PE separator caused an increase in texture. The lower impact glass fiber separator reduced the texture, causing the more random distribution of the Li crystal structure. This research is first of its kind in the practical application of texture to understand the texture elements within the Li metal battery as Li is plated and the impact it has on crystal structure and the strength of Li dendrites. This opens the door for a new understanding of Li crystal structure through the beginning stages of the cell. Further study to be considered would be how are the texture changes depending on the state of charge and lifetime of the battery? Can we modify the surface of the current collector to induce a particular texture changing the texture to one in the Z direction to the Y direction?

Li metal-oxide interactions were studied, and the WO_3 was found to modify the plating and stripping of Li metal through a threefold mechanism of first modifying the morphology and

nucleation of the Li. Secondly, it was shown through XPS analysis that the WO_3 was able to help induce further decomposition of electrolyte components making an inorganic rich SEI high in LiF amounts, causing smooth morphologies. Thirdly, the presence of W within the SEI demonstrated that the mixed interface with electronic conductors, in addition to ionic conductors, helps to mitigate " dead" Li and decrease the R_{SEI}. This represents a new understanding of the role of metals within the SEI. Additionally, this gives another piece in the puzzle to fit together with other mitigation options to try to realize the practical uses of the Li metal battery. This thesis serves as a critical piece in understanding the fundamental nature of some of the interfacial reactions with Li metal in the Li metal battery system.

Bibliography

1. S. Goriparti, E. Miele, F. D. Angelis, E. D. Fabrizio, R. P. Zaccaria, C. Capiglia, *Journal of Power Sources* **257**, 421–443 (2014).

2. J. Xu, S. Dou, H. Liu, L. Dai, *Nano Energy* **2**, 439–442 (2013).

3. M. J. Loveridge, G. Remy, N. Kourra, R. Genieser, A. Barai, M. J. Lain, Y. Guo, M. Amor-Segan, M. A. Williams, T. Amietszajew, *et al.*, *Batteries* **4**, 3 (2018).

4. A. Jana, D. R. Ely, R. E. Garcia, *Journal of Power Sources* **275**, 912–921 (2015).

5. C. Niu, H. Lee, S. Chen, Q. Li, J. Du, W. Xu, J.-G. Zhang, M. S. Whittingham, J. Xiao, J. Liu, *Nature Energy* **4**, 551–559 (July 1, 2019).

6. K.-H. Chen, K. N. Wood, E. Kazyak, W. S. LePage, A. L. Davis, A. J. Sanchez, N. P. Dasgupta, *Journal of Materials Chemistry A* **5**, 11671–11681 (2017).

7. J. Xiao, *Science* **366**, 426–427 (2019).

8. P.-H. Haumesser, in *Nucleation and Growth of Metals*, ed. by P.-H. Haumesser (Elsevier, 2016), pp. 59–70.

9. J. R. Groza, J. F. Shackelford, *Materials Processing Handbook* (CRC press, 2007).

10. M. Schlesinger, M. Paunovic, *Modern Electroplating* (John Wiley & Sons, 2011), vol. 55.

11. J. B. Goodenough, Y. Kim, *Chem Mater* **22**, 587–603 (2010).

12. C. Fiedler, B. Luerssen, M. Rohnke, J. Sann, J. Janek, *J Electrochem Soc* **164**, A3742–A3749 (Dec. 2017).

13. F. Single, B. Horstmann, A. Latz, *J Electrochem Soc* **164**, E3132–E3145 (2017).

14. Y. C. Chen, C. Y. Ouyang, L. J. Song, Z. L. Sun, *The Journal of Physical Chemistry C* **115**, 7044–7049 (2011).

15. Q. Zhang, J. Pan, P. Lu, Z. Liu, M. W. Verbrugge, B. W. Sheldon, Y.-T. Cheng, Y. Qi, X. Xiao, *Nano Lett* **16**, 2011–2016 (2016).

16. C. Monroe, *J Electrochem Soc* **152**, A396–A404 (Jan. 2005).

17. X.-R. Liu, X. Deng, R.-R. Liu, H.-J. Yan, Y.-G. Guo, D. Wang, L.-J. Wan, *ACS Applied Materials & Interfaces* **6**, 20317–20323 (2014).

18. J. Zhang, R. Wang, X. Yang, W. Lu, X. Wu, X. Wang, H. Li, L. Chen, *Nano Lett* **12**, 2153–2157 (2012).

19. H. KUWATA, H. SONOKI, M. MATSUI, Y. MATSUDA, N. IMANISHI, *Electrochemistry* **84**, 854–860 (2016).

20. J. Heine, P. Hilbig, X. Qi, P. Niehoff, M. Winter, P. Bieker, *J Electrochem Soc* **162**, A1094–A1101 (Feb. 2015).

21. E. Markevich, G. Salitra, D. Aurbach, *ACS Energy Letters* **2**, 1337–1345 (2017).

22. E. Markevich, G. Salitra, F. Chesneau, M. Schmidt, D. Aurbach, *ACS Energy Letters* **2**, 1321–1326 (2017).

23. D. Aurbach, K. Gamolsky, B. Markovsky, Y. Gofer, M. Schmidt, U. Heider, *Electrochim Acta* **47**, 1423–1439 (2002).

24. J. Guo, Z. Wen, M. Wu, J. Jin, Y. Liu, *Electrochem Commun* **51**, 59–63 (2015).

25. S. Xiong, K. Xie, Y. Diao, X. Hong, *J Power Sources* **246**, 840–845 (2014).

26. X. Liang, Z. Wen, Y. Liu, M. Wu, J. Jin, H. Zhang, X. Wu, *J Power Sources* **196**, 9839–9843 (2011).

27. W. Li, H. Yao, K. Yan, G. Zheng, Z. Liang, Y.-M. Chiang, Y. Cui, *Nat Commun* **6**, 7436 (2015).

28. C. Yan, X.-B. Cheng, C.-Z. Zhao, J.-Q. Huang, S.-T. Yang, Q. Zhang, *J Power Sources* **327**, 212–220 (2016).

29. C.-Z. Zhao, X.-B. Cheng, R. Zhang, H.-J. Peng, J.-Q. Huang, R. Ran, Z.-H. Huang, F. Wei, Q. Zhang, *Energy Storage Materials* **3**, 77–84 (2016).

30. M. Wang, L. Huai, G. Hu, S. Yang, F. Ren, S. Wang, Z. Zhang, Z. Chen, Z. Peng, C. Shen, D. Wang, *The Journal of Physical Chemistry C* **122**, 9825–9834 (2018).

31. S.-Y. Ha, J.-G. Han, Y.-M. Song, M.-J. Chun, S.-I. Han, W.-C. Shin, N.-S. Choi, *Electrochim Acta* **104**, 170–177 (2013).

32. Z. Xie, Z. Wu, X. An, X. Yue, A. Yoshida, X. Du, X. Hao, A. Abudula, G. Guan, *Chemical Engineering Journal* **393**, 124789 (2020).

33. Y. Qian, Y. Kang, S. Hu, Q. Shi, Q. Chen, X. Tang, Y. Xiao, H. Zhao, G. Luo, K. Xu, Y. Deng, *ACS Applied Materials & Interfaces* **12**, PMID: 32040291, 10443–10451 (2020).

34. X. Shen, H. Ji, J. Liu, J. Zhou, C. Yan, T. Qian, *Energy Storage Materials* **24**, 426–431 (2020).

35. F. Ding, W. Xu, G. L. Graff, J. Zhang, M. L. Sushko, X. Chen, Y. Shao, M. H. Engelhard, Z. Nie, J. Xiao, X. Liu, P. V. Sushko, J. Liu, J. G. Zhang, *J Am Chem Soc* **135**, 4450–6 (2013).

36. W. Jia, C. Fan, L. Wang, Q. Wang, M. Zhao, A. Zhou, J. Li, *ACS Applied Materials & Interfaces* **8**, PMID: 27237827, 15399–15405 (2016).

37. A. Basile, A. I. Bhatt, A. P. O'Mullane, *Nat Commun* **7**, ncomms11794 (2016).

38. M. Ishikawa, H. Kawasaki, N. Yoshimoto, M. Morita, *J Power Sources* **146**, Selected papers pressented at the 12th International Meeting on Lithium Batteries, 199–203 (2005).

39. N. W. Li, Y. X. Yin, C. P. Yang, Y. G. Guo, *Adv Mater* **28**, 1853–8 (2016).

40. K. Liao, S. Wu, X. Mu, Q. Lu, M. Han, P. He, Z. Shao, H. Zhou, *Adv Mater* **30**, 1705711 (2018).

41. Q.-C. Liu, J.-J. Xu, S. Yuan, Z.-W. Chang, D. Xu, Y.-B. Yin, L. Li, H.-X. Zhong, Y.-S. Jiang, J.-M. Yan, X.-B. Zhang, *Adv Mater* **27**, 5241–5247 (2015).

42. L. Ma, M. S. Kim, L. A. Archer, *Chem Mater* **29**, 4181–4189 (2017).

43. Y. Zhao, M. Amirmaleki, Q. Sun, C. Zhao, A. Codirenzi, L. V. Goncharova, C. Wang, K. Adair, X. Li, X. Yang, F. Zhao, R. Li, T. Filleter, M. Cai, X. Sun, *Matter* **1**, 1215–1231 (Nov. 6, 2019).

44. A. C. Kozen, C.-F. Lin, A. J. Pearse, M. A. Schroeder, X. Han, L. Hu, S.-B. Lee, G. W. Rubloff, M. Noked, *ACS Nano* **9**, PMID: 25970127, 5884–5892 (2015).

45. S. C. Jung, Y.-K. Han, *The Journal of Physical Chemistry Letters* **4**, 2681–2685 (2013).

46. S. S. Zhang, X. Fan, C. Wang, *Electrochim Acta* **258**, 1201–1207 (2017).

47. Y. Zhang, W. Luo, C. Wang, Y. Li, C. Chen, J. Song, J. Dai, E. M. Hitz, S. Xu, C. Yang, Y. Wang, L. Hu, *Proceedings of the National Academy of Sciences* **114**, 3584–3589 (2017).

48. S.-H. Wang, Y.-X. Yin, T.-T. Zuo, W. Dong, J.-Y. Li, J.-L. Shi, C.-H. Zhang, N.-W. Li, C.-J. Li, Y.-G. Guo, *Adv Mater* **29**, 1703729 (2017).

49. A. Wang, X. Zhang, Y.-W. Yang, J. Huang, X. Liu, J. Luo, *Chem* **4**, 2192–2200 (2018).

50. S. Liu, X. Xia, Y. Zhong, S. Deng, Z. Yao, L. Zhang, X.-B. Cheng, X. Wang, Q. Zhang, J. Tu, *Adv Energy Mater* **8**, 1702322 (2018).

51. Q. Li, S. Zhu, Y. Lu, *Adv Funct Mater* **27**, 1606422 (2017).

52. C. Yang, Y. Yao, S. He, H. Xie, E. Hitz, L. Hu, *Adv Mater* **29**, 1702714 (2017).

53. L. Fan, S. Li, L. Liu, W. Zhang, L. Gao, Y. Fu, F. Chen, J. Li, H. L. Zhuang, Y. Lu, *Adv Energy Mater* **8**, 1802350 (2018).

54. S.-S. Chi, Y. Liu, W.-L. Song, L.-Z. Fan, Q. Zhang, *Adv Funct Mater* **27**, 1700348 (2017).

55. Y. Gu, H.-Y. Xu, X.-G. Zhang, W.-W. Wang, J.-W. He, S. Tang, J.-W. Yan, D.-Y. Wu, M.-S. Zheng, Q.-F. Dong, B.-W. Mao, *Angew Chem Int Ed* **58**, 3092–3096 (2019).

56. Y.-J. Kim, S. H. Kwon, H. Noh, S. Yuk, H. Lee, H. soo Jin, J. Lee, J.-G. Zhang, S. G. Lee, H. Guim, H.-T. Kim, *Energy Storage Materials* **19**, 154–162 (2019).

57. A. Jain, S. P. Ong, G. Hautier, W. Chen, W. D. Richards, S. Dacek, S. Cholia, D. Gunter, D. Skinner, G. Ceder, K. a. Persson, *APL Mater* **1**, 011002 (2013).

58. H. Ding, S. S. Dwaraknath, L. Garten, P. Ndione, D. Ginley, K. A. Persson, *ACS Applied Materials & Interfaces* **8**, PMID: 27145398, 13086–13093 (2016).

59. F. Shi, A. Pei, A. Vailionis, J. Xie, B. Liu, J. Zhao, Y. Gong, Y. Cui, *Proceedings of the National Academy of Sciences* **114**, 12138–12143 (2017).

60. C. Jin, O. Sheng, Y. Lu, J. Luo, H. Yuan, W. Zhang, H. Huang, Y. Gan, Y. Xia, C. Liang, J. Zhang, X. Tao, *Nano Energy* **45**, 203–209 (2018).

61. D. Lin, J. Zhao, J. Sun, H. Yao, Y. Liu, K. Yan, Y. Cui, *Proceedings of the National Academy of Sciences* **114**, 4613–4618 (2017).

62. J. Luan, Q. Zhang, H. Yuan, D. Sun, Z. Peng, Y. Tang, X. Ji, H. Wang, *Adv Sci* **6**, 1901433 (2019).

63. Y. He, M. Gu, H. Xiao, L. Luo, Y. Shao, F. Gao, Y. Du, S. X. Mao, C. Wang, *Angew Chem Int Ed Engl* **55**, 6244–7 (2016).

64. W.-J. Li, Z.-W. Fu, *Appl Surf Sci* **256**, 2447–2452 (2010).

65. A. R. West, *Solid State Chemistry and Its Applications* (John Wiley & Sons, 2014).

66. P. Monk, R. Mortimer, D. Rosseinsky, *Electrochromism and Electrochromic Devices* (Cambridge University Press, 2007).

67. J. Xiao, Q. Li, Y. Bi, M. Cai, B. Dunn, T. Glossmann, J. Liu, T. Osaka, R. Sugiura, B. Wu, J. Yang, J.-G. Zhang, M. S. Whittingham, *Nature Energy* (June 25, 2020).

68. B. Wu, J. Lochala, T. Taverne, J. Xiao, *Nano Energy* **40**, 34–41 (2017).

69. J. Barton, J. O. Bockris, *Proceedings of the Royal Society of London. Series A. Mathematical and Physical Sciences* **268**, 485–505 (1962).

70. A. Bard, L. Faulkner, *Electrochemical Methods: Fundamentals and Applications, 2nd Edition* (Wiley Textbooks, 2000).

71. E. Aydogan, S. Pal, O. Anderoglu, S. Maloy, S. Vogel, G. Odette, J. Lewandowski, D. Hoelzer, I. Anderson, J. Rieken, *Materials Science and Engineering: A* **661** (Mar. 2016).

72. R. Hielscher, H. Schaeben, *Journal of Applied Crystallography* **41**, 1024–1037 (2008).

73. O. Engler, V. Randle, *Introduction to Texture Analysis: Macrotexture, Microtexture, and Orientation Mapping* (CRC press, 2009).

74. M. a.-S. Duesbery, V. Vitek, *Acta Materialia* **46**, 1481–1492 (1998).

75. A. J. Louli, M. Genovese, R. Weber, S. G. Hames, E. R. Logan, J. R. Dahn, *Journal of The Electrochemical Society* **166**, A1291–A1299 (2019).

76. M. Yang, J. Hou, *Membranes* **2**, 367–383 (2012).

77. M. Altman, E. Bauer, *Surface Science* **347**, 265–279 (1996).

78. L. Ying-jun, W. Jiang-ping, G. Qin-lin, G. Lin-lin, T. You-qi, *Chinese Journal of Catalysis* **1** (1987).

79. J. Lochala, T. Taverne, B. Wu, M. Benamara, M. Cai, X. Xiao, J. Xiao, *ACS applied materials & interfaces* **11**, 44204–44213 (2019).

80. X.-B. Cheng, C. Yan, X.-Q. Zhang, H. Liu, Q. Zhang, *ACS Energy Letters* **3**, 1564–1570 (2018).

81. G. Karkera, A. S. Prakash, *ACS Applied Energy Materials* **1**, 1381–1388 (2018).

82. Z. Zhang, X. Xu, S. Wang, Z. Peng, M. Liu, J. Zhou, C. Shen, D. Wang, *ACS Applied Materials & Interfaces* **8**, 26801–26808 (2016).

83. D. Aurbach, E. Zinigrad, Y. Cohen, H. Teller, *J. Solid State Ionics* **148**, 405–416 (2002).

84. D. Lide, *Crc Handbook of Chemistry and Physics, 87th Edition* (Taylor & Francis, 2006).

85. C. Yan, X.-B. Cheng, Y.-X. Yao, X. Shen, B.-Q. Li, W.-J. Li, R. Zhang, J.-Q. Huang, H. Li, Q. Zhang, *Adv Mater* **30**, 1804461 (2018).

86. I. Kishida, Y. Koyama, A. Kuwabara, T. Yamamoto, F. Oba, I. Tanaka, *The Journal of Physical Chemistry B* **110**, 8258–8262 (2006).

87. L. Lin, F. Liang, K. Zhang, H. Mao, J. Yang, Y. Qian, *J. Mater. Chem. A* **6**, 15859–15867 (32 2018).

88. J. A. Rodriguez, J. Hrbek, *The Journal of Physical Chemistry* **98**, 4061–4068 (1994).

89. R. Adams, *Journal of Vacuum Science & Technology A: Vacuum, Surfaces, and Films* **1**, 12–18 (1983).

90. D. Mainprice, F. Bachmann, R. Hielscher, H. Schaeben, *Geological Society, London, Special Publications* **409** (Aug. 2014).

A Appendix

A.1 Materials & Methods

A variety of metal substrates were obtained for the use the various experiments. The metal substrates were cut (ϕ =14 μm) sonicated in ethanol (EtOH) for 15 min then dried overnight in a vacuum oven at 80deg C. The metals were then utilized in coin cells for electrochemical testing, and characterization preparation.

A.1.1 Methods

Thermal Oxidation

The preparation of WO_3 on the surface of tungsten foil (Alfa Assar, 0.05 mm thick) was formed using thermal oxidation. Thermal oxidation utilizes high heat and oxygen to form the metal oxide on the surface of the metal, undergoing the following conversion.

$$2W + 3O_2 \rightarrow WO_3 \tag{A.1}$$

Thermal oxidation is a useful preparation method due to the ease of forming thin films of the oxide. The thickness can be controlled by oxygen content, temperature, and heating time.

Magnetron Electron Sputtering

WO_x films were formed using Magnetron Electron Sputtering Technique. Magnetron Electron Sputtering is a Plasma Vapor Deposition (PVD) process where plasma is created using positive ions that are accelerated on the W target. The W atoms are ejected from the target and condensed on the surface of the target. The oxygen of the as-prepared WO_x films depends on the oxygen content within the magnetron. This process was done by Dr. Xingchen Xiao of General Motors Research and Development Center in collaboration with our lab.

A.1.2 Important Characterization Techniques

Ex-situ X-ray Diffraction

X-ray Diffraction (XRD) is a powerful technique to understand the crystal structure of solid materials. XRD for this work was performed on a Panalytical X'Pert Materials Research

Diffractometer using a Solid State PIXcel™ detector. Cu radiation with a generator voltage of 45 mV and tube current of 40 mA, a Kα1 (λ = 1.54056 Å) and Kα2 (λ= 1.54439 Å) with a Kα1:Kα2 ratio of 0.5 was used for all experiments. The general XRD scans were done for a 2θ range of 20-90 ° with a step size of 0.02 ° and a time per step of 0.5 s. Lithium metal samples were placed on carbon tape on a glass slide, with a double layer of clear tape wrapped around the glass to prevent reaction with the atmosphere. The pole figures were done for Li(110) and Li(220) at a 2θ of approx. 36.19 ° and 52.12 ° from 0-360 ° Φ and 0-60 ° Ψ with a step size of 1 and 1.2 respectively 0.65s dwell time. Rietveld calculations were performed using the X'Pert HighScore software version 2.2e.

X-ray Photo Spectroscopy

X-Ray Photo Spectroscopy is a technique used to the elemental composition and electronic state of elements on materials. The XPS used in this study was the PHI VersaProbe XPS instrument with a 25W monochromatized Al Kα radiation. Software analysis was performed using XPSspeak41 in conjunction with CasaXPS version 2.319PR.10 for composition evaluation. Samples were prepared in the glovebox and sealed for transportation to the machine. Samples were quickly transferred to XPS with minimal exposure to the ambient atmosphere (approx. $>$ 1 min).

A.2 Chapter 2 Supplemental Information

A.2.1 Alloying of Ag with Li

The Ag shows a very high coulombic efficiency; this is due to the reversible alloying of the Ag with the Li. The voltage polarization (**Figure A.1a**) shows the average potential on discharge to be greater than 0V, demonstrating the lack of Li plating. From the voltage profile in **Figure A.1b**, the first discharge shows that in Lithium initial has a plating plateau at -0.05V. The 20th discharges show a discharge curve more closely resembling the alloying profile. This completely stabilizes, and a clean alloy is shown at both cycle 40 and 80. This is the reason for the low coulombic efficiency during the earlier cycles, which then stabilizes the latter cycles. The Ag alloy is significant in that the alloy displays a low volume contraction/expansion of 18% as compared to that of Si which is 70% and the volume change in Li plating which theoretically would be 100%.[88] In addition, the Ag-Li bonding is considered to be metallic with some ionic properties, allowing the minimization of the negative effects of the electron-donor properties of the Li. This allows for the Li to still be highly active in SEI formation.[88] This will be utilized later in the future conversion

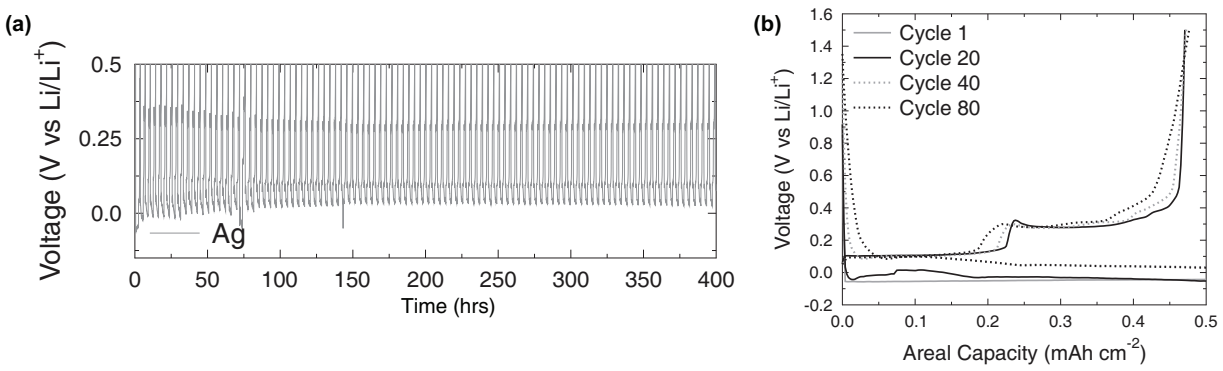

Figure A.1: Voltage polarization and voltage profile of Ag (**a**) & (**b**)

materials section.

A.2.2 Stainless Steel's Interaction with Li metal

The Stainless steel substrates displayed a rather odd low initial coulombic efficiency, which later on rises to between 60-80%. The voltage polarization (**Figure A.2a**) reveals that plating for Fe81 doesn't start to occur until around the 250th-hour mark. The voltage profile (**Figure A.2b**) shows that no actual lithium plating happens at up to 80 cycles. The reaction that seems to be occurring in the stead of Li plating is the decomposition of Cr_2O_3 with Li following the equation:

$$Cr_2O_3 + 6Li \rightarrow 2Cr + 3Li_2O\,(0.5V vs Li^+/Li) \tag{A.2}$$

This is due to the large component of the Cr and the fact that the native oxide on stainless steel is mostly composed of Cr_2O_3 giving it its "stainless" properties.[89] Both the Fe86 (**Figure A.2c, d**) and Fe87 (**Figure A.2e**) show a similar reaction with the Cr; however, they show lithium plating sooner than that of the Fe81. This points to a decreasing amount of the Cr_2O_3 present, which decreases the side reactions. Additionally, the presence and quantity of the impurities are minimized, showing that the substrate composition and surface compounds have a significant effect on the plating and stripping of Li metal. The Fe81 (**Figure A.3a**) shows a surface with striations with a surface roughness visibly similar to that of the copper shown in Figure 2.3 from Chapter 2. The Fe86 (**Figure A.3b**) shows similar striations but a smoothness visibly closer to that of the W shown in Figure 2.3 from Chapter 2. The Fe87 (**Figure A.3c**) shows striations as well but with a roughness that is the worst of all the metal substrates. After plating Li to a capacity of 1 mAh cm^{-2}, the Fe81 (**Figure A.3h**) shows a morphology with smooth spots, mixed with bulges at different areas, Fe86 (**Figure A.3i**) however differs with a mossy structure similar to the Cu with

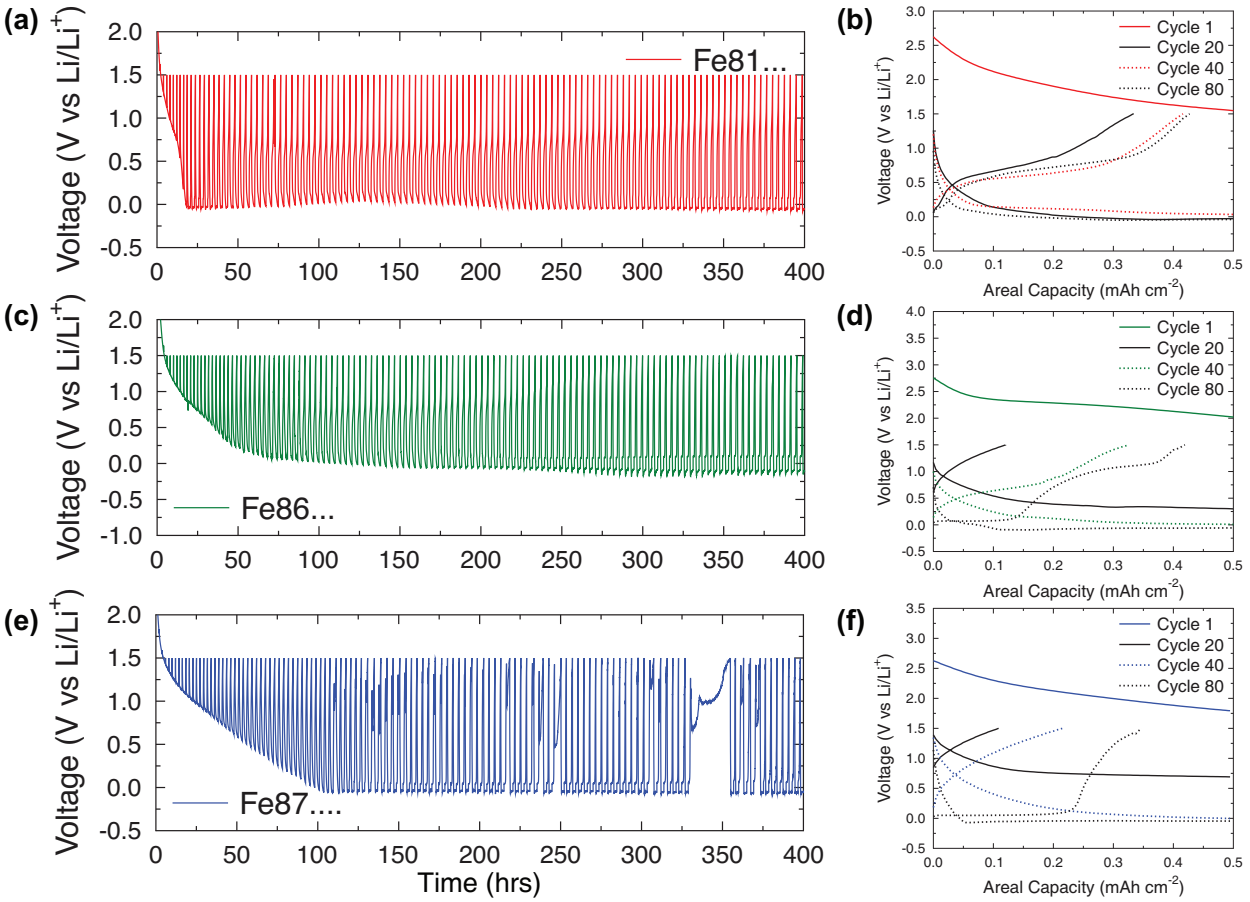

Figure A.2: Voltage polarization and voltage profile of Fe81 (**a**) & (**b**), Fe86 (**c**) & (**d**), and Fe87 (**e**) & (**f**) respectively.

platelet like structure intermixed with the substrate. Fe87 (**Figure A.3j**) shows a similar structure to that of the Fe81 with less of the boulder-like structures. Upon further plating to 3 mAh cm^{-2}, the Fe81 (**Figure A.3m**) shows that the boulders have developed into the mossy structures seen in the Cu. The Fe86 (**Figure A.3n**) shows that the platelets have disappeared, and a greater quantity of fibers have developed compared to that of the W. The Fe87 (**Figure A.3o**) substrate shows the same development of the boulder-like-structures into the mossy structures indicative of bulk lithium growth.

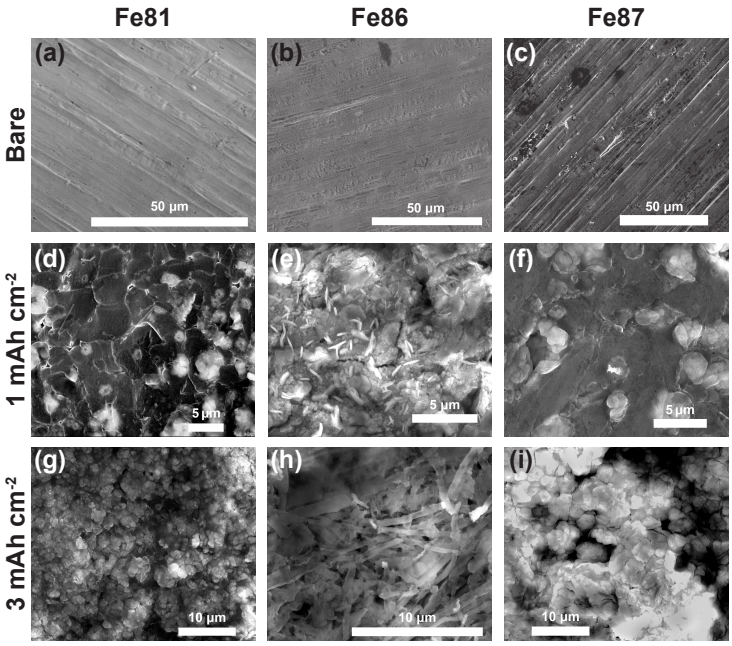

Figure A.3: Voltage polarization and voltage profile of Fe81 (**a**) & (**b**), Fe86 (**c**) & (**d**), and Fe87 (**e**) & (**f**) respectively.

A.3 Chapter 3 Supplemental Material

A.3.1 Quantifying Texture to Understand Anisotropy

Quantification of the anisotropy of the various samples is given in the Texture Index. Texture Index is a calculation based on the volume fraction of crystal with any given orientation, where TI=1 is a completely random distribution, and a single orientation will have an infinity large value[90]. The other measurement that can be used to quantify the texture is the Entropy of the ODF. Where the texture index changes based upon the large values within an ODF, the entropy is very sensitive to the small variances within an ODF. The uniform random distribution has an entropy=0 and has a minimum or negative value for a unimodal orientation. **Table 3.1** shows the Texture

Table A.1: Texture index of samples with PE and GF separators.

Sample	20μm PE	200μm PE	200μm GF
Polycrystalline Cu	2.1614	2.1614	2.0926
Polycrystalline W	2.8754	2.8754	2.1243
Cu(100)	2.475	2.3196	1.8736
Cu(110)	13.9786	2.3913	2.0765
W(100)	7.8284	2.5146	2.4441

Index for all samples previously discussed. It shows that the Cu(110) is the most highly textured,

Table A.2: Active Material Loading of Conversion Coated onto Cu for conversion material screening.

Conversion Material	Active Material Loading ($mg \cdot cm^{-2}$)
WO_3	1.024
WS_2	0.8994
WSe_2	1.603
WTe_2	0.299
WCl_6	0.783
VSe_2	1.193
$MnSe_2$	0.1958
Fe_3O_4	1.522
Cr_2O_3	1.340
AgF	0.869
Cu_2O	1.566

followed by W(100) at low Li thicknesses. With the increased thicknesses, the texture decreases to roughly the same value of 2 with Poly-W and W(100) being the two largest textured, respectively. The further de-texturing effect of the GF is seen by the Texture Index decreasing further for all samples. This shows that while the pole figures show the Li has crystals oriented in 3D space, their orientation at higher thicknesses becomes quite low, becoming more randomly oriented rather than highly focused.

$$f_{est} = argmin \sum Ni = 1 \tag{A.3}$$

A.4 Chapter 5 Supplemental Material

A.4.1 Conversion Material Coating Ratio

90% Conversion Material

10% PVDF(5% Solution) in NMP

Carbon Coated Cu Substrate

A.4.2 Conversion Active Loading

A.5 IKB Synthesis

Weights

Ketjen Black (KB) 0.5g

Citric Acid (CA) 1g

Ethylene Glycol (EG) 0.64g

Isopropanol 10 drops

A.5.1 Procedure

1. Grind KB for 5 mins
2. Add KB, CA mixture to a 100 mL round bottom flask
3. Add 50 mL of Deionized Water, 10 drops of Isopropanol, 10 drops of Isobutanol
4. Sonicate for 2 mins to ensure dispersion
5. Place in an oil bath and add EG
6. Add 2 cm stir bar and set stirring to 1
7. Place water condenser on flask and heat at 130°C for 5 hrs
8. Monitor, the reaction, maintaining water flow and proper stirring
9. After 5 hrs remove the condenser and place foil on the opening to the round bottom flask
10. Poke holes in the foil to control the evaporation time
11. When the material looks like playdough, carefully remove the flask and turn everything off
12. Remove the material from the flask and place in a crucible boat for tube furnace
13. Follow instructions on the tube furnace and heat the material at 400°C for 5 hrs
14. After 5 hrs increase the temperature to 900°C for 10 hrs
15. When the 10 hrs have elapsed, turn off the heat, make sure the air is still flowing, and allow the material to come to room temperature.
16. When the material has reached room temp ≈ 25°C remove from the tube furnace.
17. Lightly grind the resulting material and measure the amount recovered
18. Clean and store everything for next use

A.6 Sulfur Loading

A.6.1 Weights/Ratios

Sulfur 80% by wt.

IKB 20% by wt.

Procedure

1. Measure out sulfur and carbon materials
2. Place in a mortar and proceed to grind the two together until no yellow is visible
3. Place in a hydrothermal bomb and proceed to heat in a box furnace at 155°*C* for 24 hrs
4. Once complete, remove from the bomb and measure the amount recovered
5. Label as IKB-S with the date
6. Clean and store everything for next use

A.7 IKB-S Slurry

A.7.1 Ratio/Weights

IKB-S 80% by wt. 0.16g

CNF 10% by wt. 0.02g

CMC (2% solution) 6% by wt. 0.06g

SBR (20% solution) 4% by wt. 0.04g

A.7.2 Procedure

1. 0.02g of Carbon nanofibers mixed with 0.6g of CMC solution at 2000rpms for 20 minutes and defoam at 2200 RPMs for 10 min
2. Add 0.16g of IKB-S and 5 drops of Isobutanol, repeat stirring procedure from step 1

3. Add 0.04g of SBR solution and mix at 2000 RPMs for 10 min, then defoam for 5 min at 2200 RPMs

4. Add drops of water and mix at 2000 RPMs for 30 seconds, defoaming for 30 seconds at 2200 RPMs to insure slurry is of the proper viscosity.

5. Coat on carbon-coated aluminum at 15 using the electrode blade

6. Air dry overnight, then punch into 14mm diameter electrodes and put in the vacuum oven for 8 hrs at -30 kPa at 20$^{\circ}C$

7. Place in the glovebox for assembly

A.8 Lithium/S Cell Assembly

Everything in the following procedure is done within the glovebox unless specifically stated otherwise.

1. Prepare Anode Cap, Spring, Stainless Steel Spacer, Cathode cap, and Celgard separator in the glovebox for battery assembly

2. Place the cathode can on the scale and tare it

3. Place the sulfur cathode in the cathode can, with the active material facing up and take the weight

4. Take the weight as X and do the following calculation

$$[X - 0.00652g\ (Al\ substrate)] \times 0.64\ (\%\ of\ active\ material) \tag{A.4}$$

   This is the amount of sulfur.

5. To determine the amount of electrolyte multiply the amount of sulfur by the ratio that will be used (For 20:1 multiply by 20)

6. While the cathode can is still on the scale, zero and add the amount of electrolyte in grams to the cathode

7. Remove the cathode can from the scale

8. Place the 2500 Celgard separator onto the S cathode
9. Add a drop of electrolyte on top the separator
10. Place stainless steel separator onto Lithium metal
11. Place SS/Li onto the Celgard Lithium facing down
12. Place Spring onto SS separator
13. Place anode cap on top and press with your hand
14. Use the Coin cell crimper, with the crimping die attached to seal the coin cell, go to redline $\approx 1200 psi$
15. Label the coin cell and remove from the glove box

A.9 Electrochemical Testing

Calculating C-rate

$$1C\ (mA) = [Theoretical\ Specific\ Capacity\ (mAh/g) \times Active\ Material\ (grams)] \div 1\ hr \quad \text{(A.5)}$$

$$mA = \frac{mAh}{g} \times \frac{g}{1} \times \frac{1}{hr} \quad \text{(A.6)}$$

A.9.1 Performance Evaluation

1. Place coin cell back in Landt battery tester
2. Discharge battery at C/20 Rate to 2.0V and charge the battery at C/20 for the first 3 cycles

$$\frac{1000\ mAh}{g} \times \frac{X\ g}{1} \times \frac{1}{20} hr = x\ (mA) \quad \text{(A.7)}$$

3. After the three cycles program Charge and Discharge at C/5 rate for 500 cycles

$$\frac{1000\ mAh}{g} \times \frac{X\ g}{1} \times \frac{1}{5} hr = x\ (mA) \quad \text{(A.8)}$$